SEQUENTIAL GROWTH, REGROWTH, AND CONTROL OF POLYPYRROLE-METAL COIL COMPOSITE ARTIFICIAL MUSCLES

by

John Cody Sarrazin

A dissertation submitted to the faculty of
The University of Utah
in partial fulfillment of the requirements for the degree of

Doctor of Philosophy

Department of Mechanical Engineering

The University of Utah

May 2015

The University of Utah Graduate School

STATEMENT OF DISSERTATION APPROVAL

The dissertation of **John Cody Sarrazin**

has been approved by the following supervisory committee members:

Stephen A. Mascaro	, Chair	**12/9/2014** Date Approved
Debra Mascaro	, Member	**12/9/2014** Date Approved
Sanford G. Meek	, Member	**12/9/2014** Date Approved
Shadrach Roundy	, Member	**12/9/2014** Date Approved
Mikhail Skliar	, Member	**12/9/2014** Date Approved

and by **Tim A. Ameel** , Chair/Dean of the Department/College/School of **Mechanical Engineering**

and by David B. Kieda, Dean of The Graduate School.

ABSTRACT

Conducting polymer actuators have shown numerous improvements in mechanical performance over the last couple of decades, but can be better utilized in applications with the ability to adjust to unknown operating conditions, or improved during their lifetime. This work employs the process of sequential growth to initially fabricate polypyrrole-metal coil composite actuators, and then again for further actuator growth during its lifetime of operation.

The novel synthesis process was first shown through the use of a custom testing apparatus that could support the sequential growth process by allowing different actuation and synthesis solutions to be controlled in the test cell, as well as facilitate mechanical performance testing.

Open-loop testing demonstrated the actuator system performance for multiple growth stages over multiple input frequencies, and was then compared to the parameters identified to fit a simplified model during operation. The simplified model was shown to differentiate from the experimental data, but provided useful optimal growth prediction values with a performance cost evaluation algorithm. The model could predict the optimal growth determined by the experimental data to within one growth stage.

Performance was improved by using a proportional-derivative feedback controller where the gains were calculated by the desired response at each

growth stage for each sample. The cost performance was performed again with the closed-loop data, but did an inferior job of predicting the optimal amount of growth for each sample compared to the open-loop data. The simplified model accurately tracked the behavior changes through multiple stages of growth. The main contributions of this work include a novel testing apparatus and synthesis method for multiple growth steps, the implementation of a simplified model for tracking and optimal growth stage prediction, and the application of a model-based proportional-derivative feedback controller.

For my family, related and otherwise; especially my mother, father, and sister.
Your support is unending.

TABLE OF CONTENTS

LIST OF TABLES

LIST OF FIGURES

CHAPTER 1

INTRODUCTION TO POLYMERS

1.1 Dissertation Motivation

The ability of actuators to mimic human muscle is an ongoing challenge. Multiple actuator technologies can produce comparable, and even advanced mechanical performance, yet none have shown the human ability to heal or to regrow during use. This missing component, the organic process of evolving during use, is a challenge that this research seeks to address.

An iterative approach was applied to a multiple link robot by Pil and Asada to improve the dynamic response by adding mass at specific spacing along the robot links [1]. The approach was three-pronged by analyzing the current dynamic system and predicting an improvement with added mass, actively adding mass, and then refining the control scheme to account for the adjusted system. The process flow is shown in Fig. 1.1. This work seeks to take a similar approach where adding mass equates to adding polymeric material and strength capability, as well as improving polymer degradation.

The first step was to choose a suitable material. This search started within the field of smart materials. Piezoelectric materials possess impressive strength and speed, but lack in strain magnitude and require an extensive generation process

involving extreme heat to create crystalline structures. Shape memory alloys exhibit useful strain and speed for macroscale actuation, but possess an extremely difficult manufacturing process to control the composition parameters closely, and work with the reactive nature of titanium. The solution was found in the group of materials known as electroactive polymers (EAPs). Specifically, the discovery of conducting polymers (CPs) in the late 1970s has spearheaded research approaches to actuator fabrication, application, and implementation. In the last couple of decades, CPs have made great leaps due to material composition, geometric design, polymerization process, and currently, the ability to regrow during operation.

1.2 Introduction

The implementation of CPs began back in the mid-19th century with the discovery of aniline. It was not until a century later, though, that the conductivity of these materials was noticed with a form of polypyrrole (PPy) in the semiconductor range. CPs more akin to the forms known today were not created until 1977 with the discovery of polyacetylene [2, 3], and the increase in conductivity in its doped state. An increase in research soon followed in this field of newly minted ‘organic metals,’ ‘synthetic metals,’ or ‘plastic metals’ [4]. CPs are also referred to as conjugated polymers, or π-conjugated polymers. This is due to the fact that their conductive nature is made possible by the delocalized electrons in the π orbits created by the π orbit overlapping along the polymer chain as a result of the conjugated backbone.

Although polyacetylene was the first of the CPs to be used, the inherent instability and difficulty in manufacturing made researchers more heavily explore the CPs, polyaniline (PANi), polythiophene (Pth), and polypyrrole (PPy). All three CPs present a higher stability, and the ability to be fabricated electrochemically [5-7] and their molecular structures are shown in Fig. 1.2.

1.3 Artificial Muscle Actuators

EAPs have expanded to cover a large range of applications and uses that include coatings, energy storage devices, sensors, and actuators [8-19]. Much of the current research is focused upon actuators due to their similarities to natural muscle, like skeletal muscle in humans. Considering CPs specifically, both CPs and natural muscles are made up of polymeric materials, both operate in chemical solutions, both use electrical input or stimulation, and both use that input to convert chemical energy into mechanical energy. Both materials also create actuation as a combination of free (unloaded) strain, change in elastic modulus, and creep strain. For these reasons, CPs are sometimes referred to as, 'artificial muscles.'

1.3.1 Human Muscle

Although mammalian muscle can be classified as skeletal muscle, smooth muscle, or cardiac muscle, this work focuses on the voluntary muscle used for dexterity and locomotion, skeletal muscle. Human muscle can exceed 40% strain, 0.35 MPa, 100%/s strain rate, but typical values of stress and strain are

0.1 MPa and 20%. Comparison values are shown in Table 1.1.

1.3.2 CP Actuators

Actuation of CP materials is a result of volumetric changes. It is controlled with an electrical input which offsets the electrical balance in the material, and counter-ions are exchanged between the CP and the electrolytic solution it operates in to accommodate the change in electrical potential.

The mechanical performance of CPs has greatly increased since their initial creation; mainly through improvements in synthesis techniques, material selection, and electrolyte solvent selection. The CP material PPy has exhibited greater stress, strain, and work density than human muscle, but generally has a much shorter life span. The general operation principles for reduction and oxidation are shown below in Fig.1.3 and the comparison to human muscle is shown in Table 1.2.

1.4 CP Materials

The three most common conducting polymer actuator materials are polyaniline (PANi), polythipophene (Pth), and polypyrrole (PPy). All three can be synthesized through electrical and electrochemical means and use ion insertion or rejection through oxidation and reduction for volume change [4, 21-29]. Polypyrrole is a common choice due to its relatively large strain stability, and conductivity [30-34].

1.5 Synthesis

1.5.1 Chemical Synthesis

Polypyrrole can be polymerized both by chemical and electrochemical means. Electrochemical fabrication is more commonly selected due to the fact that chemical synthesis creates more of a particle based structure with only a partially conjugated structure, poor mechanical properties, and lower conductivity [35, 36]. These properties make chemically synthesized PPy more commonly used in sensing applications versus actuation applications [37]. Electrochemical polymerization of PPy improves polymer structure, mechanical properties, conductivity, and also improves overall synthesis control versus purely electrical means.

1.5.2 Electrochemical Synthesis

Electrochemical polymerization of PPy commonly occurs in a three electrode cell where a reference electrode monitors the charge distribution from counter electrode to working electrode. The cell holds the monomer solution and additional doping agents. The exact mechanisms that control polymer formation are not completely understood, but the polymer forms on the working electrode in an oxidative process. Growth can be controlled through voltage or current control, and it has been demonstrated that after the initial cell activation, polymer deposition increases almost linearly with time [38]. It has also been demonstrated that polymer structure can vary according to working electrode material [31]. Some common working electrodes include gold, tin, platinum, glassy carbon, and

glass coated with conductive substrates such as indium-tin oxide. Common counter electrodes include platinum, nickel, and stainless steel.

Another factor that affects polymer growth is polymerization temperature. Higher performance polymers are achieved with a lower polymerization temperature. The colder temperatures (commonly -20 °C but even as low as -40 °C) will slow polymer kinetics to produce more uniform polymer structures and reduce unwanted polymer oligomer formation. Current density during polymerization also affects polymer structure [39-41]. Lower currents can improve polymer chain alignment, but can also increase polymer compactness to the point that ion transfer is impeded. One solution around this is sequential growth where higher current densities are used to increase polymer formation, but the high growth periods are remediated with ethanol washes when the current is turned off. Sequential growth is discussed further in the body of the dissertation. Continuous growth methods commonly use a current density of 0.1 mA/cm^2 or 0.125 mA/cm^2 and apply for anywhere from 6 to 24 hours based upon desired thickness and cell size and materials.

Polymer actuator performance is also dependent upon solvent doping due to the fact that actuation can be the result of one of more of the four reaction processes: cation injection reduction, cation ejection oxidation, anion injection oxidation, and anion ejection reduction [40, 42]. This means actuation can be affected by the molecules doped in the polymer structure during synthesis, or by the substances in the actuation solution after the polymer is synthesized. Actuation is affected by both solutions because of the range of actuation

processes [23, 43-47].

1.6 Geometry

Polypyrrole has been used to create linear and bending actuators. This work is concerned with linear actuators. Linear PPy actuators are fabricated using different actuator geometries. Initial actuators used a flat film geometry. The films are synthesized on flat electrode and then peeled off for use. Since the CPs change shape in all three dimensions concurrently, film actuators usually had a long, thin profile so the longest dimension would be the main actuator direction with the largest overall shape change. An effort to more directly orientate actuation direction in the PPy actuators came in a cylinder, or tube, shaped actuator. Now the axis of the cylinder was the main actuation direction, and the other dimensional changes resulted in relatively small changes in tube diameter. These actuators are considerably more complicated to fabricate, though, making the increase in actuation orientation an unlikely tradeoff for actuator choice. Both the flat film and tubular actuators also suffered from a low charge distribution capacity, especially as the polymers were fabricated longer and thicker to be more useful in macro robotic applications. One study showed that increasing the number of electrodes along a film actuator improved performance by increasing electron distribution and the results are shown in Fig. 1.4 [48].

The increased performance with the larger electrode dispersion, and the directional shape change of the tubular actuator geometry are combined in a polypyrrole-metal coil composite actuator geometry.

Polypyrrole-metal coil composite actuators are fabricated on a core electrode with a metal wire wrapped around it. This core plus metal coil or helix is the entire working electrode for synthesis. Once the PPy is deposited on the working electrode, the core is removed to leave the metal coil embedded within the polymer. Although it will influence mechanical performance, it directs all significant shape change to be along one dimension, the axis of the coil, and more uniformly distributes the control charge along the entire length of the actuator. Studies comparing all three geometries show a marked improvement in performance with the polypyrrole-metal coil composite actuators [17]. CP actuators with embedded metal helixes more closely resemble muscle fibers and were even bundled together in a muscle configuration. In one study, sixteen hundred were bundled together to lift a twenty-two kilogram mass [49].

1.7 Improvements

The main ways to improve actuator performance are to reduce actuator resistance, optimize mechanical properties, and extend life cycles. Incorporating a metal electrode is a means to reduce resistance along the length of the polymer actuator. Mechanical properties such as modulus can be increased by including additional materials, such as carbon nanotubes [27, 50]. Strain performance is increased with optimal doping and electrolyte selection as well as electrical input control strategies that can reduce the amount of time for any high electrical potential applications to reduce the possibility of polymer degradation [51]. Enhancing cycle life is also dependent upon avoiding degradation, as well

as avoiding degradation of the electrolytic solutions and overoxidation of the CP. Overoxidation leads to a loss of length in the conjugated backbones of the PPy material and the formation of unwanted carboxyl groups [52].

Other problems limiting life cycles in PPy are the reduction of ion migration routes as the gaps left by counter ions can be filled by diffusing lengths of polymeric chains and an overall leaning towards a more oxidized state with symmetric voltage inputs [53-55]. Apparently a symmetric current controlled input can eliminate this effect by more directly controlling the charge input to the polymer actuator system.

This work looks at improving performance by including a metal helix electrode, using sequential growth steps to optimize mechanical output and extend life cycles, and current based control to minimize destructive effects during operation.

1.8 Dissertation Structure

Chapter 2 introduces the unique testing apparatus needed to fabricate and test the sequentially synthesized PPy actuators. First, a test cell was used that could allow for the actuators to be fabricated, and then be used in actuation and additional growth tests. The test cell also allowed for easy insertion and removal of different electrolyte solutions to facilitate actuation cycles, and additional growth cycles. This test cell is part of a larger apparatus that can hold sensors to measure strain and force output, as well as house all of the necessary solutions and electrical equipment to operate and monitor the actuators.

Chapter 3 explains the investigation into the open-loop control of the actuators. Open-loop actuation tests were used to validate a simplified model, and then this simplified model was used monitor the change in model parameters over multiple growth cycles. Also, the actuators were tested at different frequencies to get a better idea of the trade-off between speed and strength in the actuators as additional growth steps are performed. These data could then be used in a performance cost analysis algorithm to predict the optimal amount of growth for a prescribed weighting value. Finally, the use of the model was analyzed as a replacement of the battery of tests needed to compile the frequency response plots.

Chapter 4 looks at closed-loop feedback control with a proportional-derivative (PD) control scheme. The same sort of testing performed in the previous chapter is performed to examine the effect of PD control through multiple growth stages on the same actuator. The frequency analysis testing allows for performance cost analysis to look at the optimal amount of growth based upon a closed-loop system. The simplified model is compared to experimental data for the closed-loop system to predict its efficiency in judging and predicting changes in actuator behavior.

A general conclusion is found in Chapter 5 with final thoughts and objectives for future work. The appendices at the end add pictures to represent equipment needed for growth and experimentation, as well as the custom test cell equipment used for the creation and control of these polypyrrole-metal coil composite actuators.

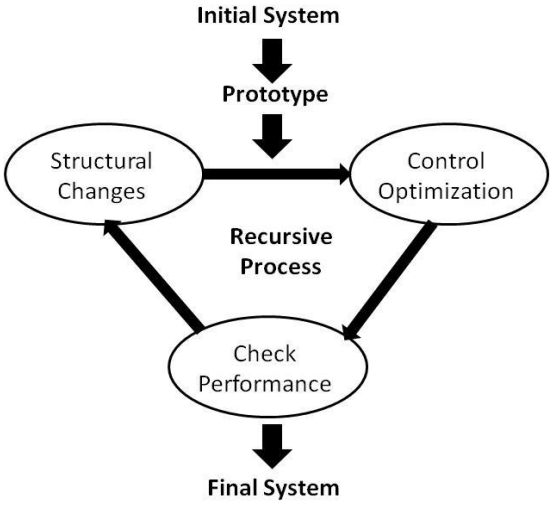

Figure 1.1. Recursive process for improving robotic prototypes (adapted from [1]).

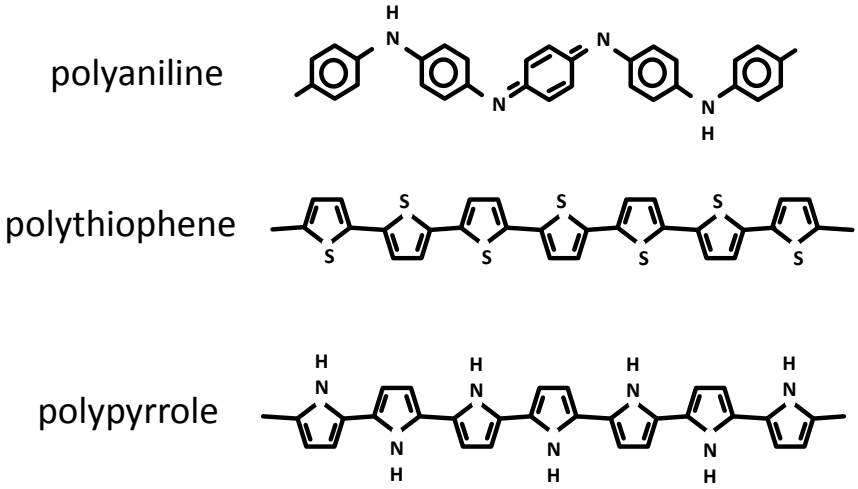

Figure 1.2. Molecular structure of three common CPs: polyaniline, polythiophene, and polypyrrole.

Table 1.1. Human muscle property values (data source [20]).

Property	Typical Value	Maximum Value
Strain (%)	20	>40
Stress (MPa)	0.1	0.35
Work Density (kJ/m^3)	8	
Density (kg/m^3)	1037	
Strain Rate %/s		500
Power to Mass (W/kg)	50	200
Efficiency (%)		40
Life Cycles		10^9
Elastic Modulus (MPa)	10-60	

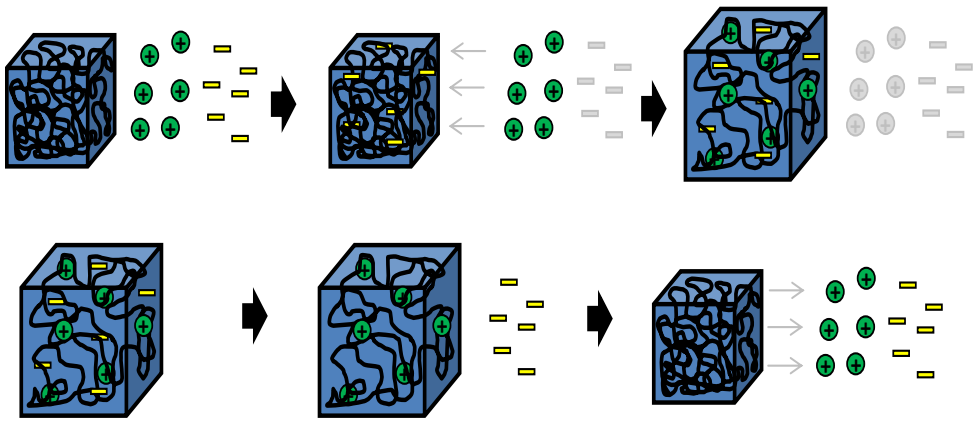

Figure 1.3. Conducting polymer actuation process. The top row shows a section of polymer separated from the cations and electrons. The next picture incorporates the electrons and this attracts the cations, incorporating them into the polymer chains. The second row shows the reverse of this process.

Table 1.2. Human muscle and PPy actuator comparison (data sources [20, 21]).

	Human Muscle	PPy Actuators
Stress (MPa)	0.1	>5
Strain (%)	20	Up to 40
Life Cycles	10^9 (Typical)	Up to 10^6
Work Density (kJ/m^3)	8	Up to 140
Efficiency (%)	>35	>30

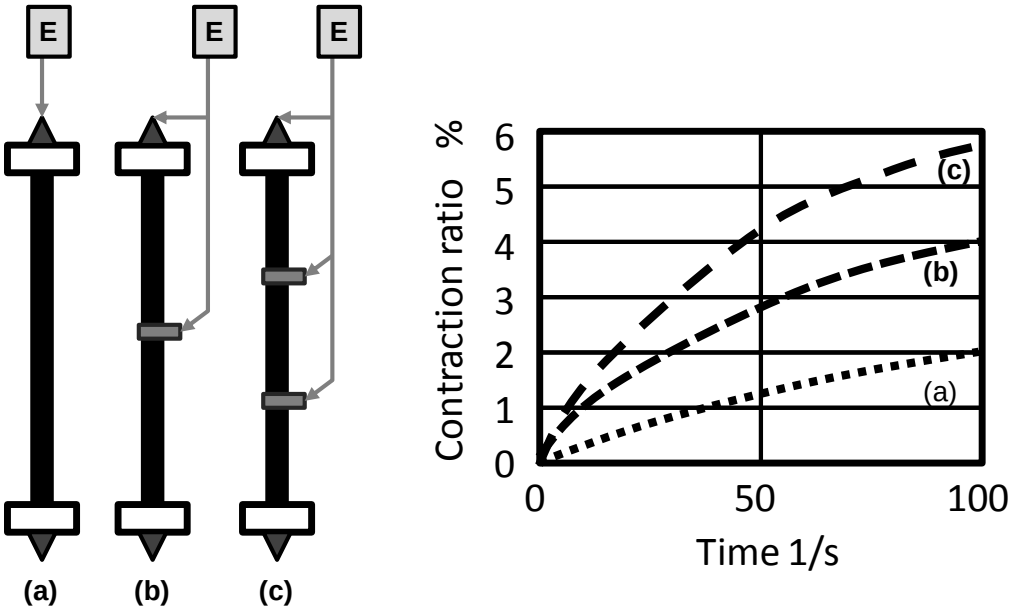

Figure 1.4. Research showing the improvement in displacement as electrode contact points are added for a flat PPy film in an aqueous NaPF6 solution at room temperature (adapted from [48]).

1.9 References

[1] A. C. Pil and H. H. Asada, "Integrated structure/control design of mechatronic systems using a recursive experimental optimization method," presented at the *IEEE/ASME Transactions on Mechatronics*, 1996.

[2] H. Shirakawa, E. J. Louis, A. G. MacDiarmid, C. K. Chiang, and A. J. Heeger, "Synthesis of electrically conducting organic polymers: halogen derivatives of polyacetylene,(CH) x," *Journal of the Chemical Society, Chemical Communications,* pp. 578-580, 1977.

[3] C. K. Chiang, C. Fincher Jr, Y. Park, A. Heeger, H. Shirakawa, E. Louis*, et al.*, "Electrical conductivity in doped polyacetylene," *Physical Review Letters,* vol. 39, p. 1098, 1977.

[4] R. Baughman, "Conducting polymer artificial muscles," *Synthetic Metals,* vol. 78, pp. 339-353, 1996.

[5] A. Diaz, K. K. Kanazawa, and G. P. Gardini, "Electrochemical polymerization of pyrrole," *Journal of the Chemical Society, Chemical Communications,* pp. 635-636, 1979.

[6] A. Diaz and J. Logan, "Electroactive polyaniline films," *Journal of Electroanalytical Chemistry and Interfacial Electrochemistry,* vol. 111, pp. 111-114, 1980.

[7] R. J. Waltman, J. Bargon, and A. Diaz, "Electrochemical studies of some conducting polythiophene films," *The Journal of Physical Chemistry,* vol. 87, pp. 1459-1463, 1983.

[8] K. Gurunathan, A. V. Murugan, R. Marimuthu, U. Mulik, and D. Amalnerkar, "Electrochemically synthesised conducting polymeric materials for applications towards technology in electronics, optoelectronics and energy storage devices," *Materials Chemistry and Physics,* vol. 61, pp. 173-191, 1999.

[9] J. Roncali, "Conjugated poly (thiophenes): synthesis, functionalization, and applications," *Chemical Reviews,* vol. 92, pp. 711-738, 1992.

[10] P. M. Beaujuge and J. R. Reynolds, "Color control in π-conjugated organic polymers for use in electrochromic devices," *Chemical Reviews,* vol. 110, pp. 268-320, 2010.

[11] M. Gerard, A. Chaubey, and B. Malhotra, "Application of conducting polymers to biosensors," *Biosensors and Bioelectronics,* vol. 17, pp. 345-

359, 2002.

[12] J. Killian, B. Coffey, F. Gao, T. Poehler, and P. Searson, "Polypyrrole composite electrodes in an all-polymer battery system," *Journal of The Electrochemical Society,* vol. 143, pp. 936-942, 1996.

[13] T. Mirfakhrai, J. D. Madden, and R. H. Baughman, "Polymer artificial muscles," *Materials Today,* vol. 10, pp. 30-38, 2007.

[14] M. Geoffrey and D. J. a. Spinks, "Electroactive conducting polymers for corrosion control: Part 2. Ferrous metals," *J Solid State Electrochem,* vol. 6, pp. 85-100, 2002.

[15] M. R. Abidian, D. H. Kim, and D. C. Martin, "Conducting-polymer nanotubes for controlled drug release," *Advanced Materials,* vol. 18, pp. 405-409, 2006.

[16] E. L. Williams, G. E. Jabbour, Q. Wang, S. E. Shaheen, D. S. Ginley, and E. A. Schiff, "Conducting polymer and hydrogenated amorphous silicon hybrid solar cells," *Applied Physics Letters,* vol. 87, pp. 223504-223504-3, 2005.

[17] J. Ding, L. Liu, G. M. Spinks, D. Zhou, G. G. Wallace, and J. Gillespie, "High performance conducting polymer actuators utilising a tubular geometry and helical wire interconnects," *Synthetic Metals,* pp. 391-398, 2003.

[18] Y. Wu, D. Zhou, G. M. Spinks, P. C. Innis, W. Megill, and G. G. Wallace, "TITAN: a conducting polymer based microfluidic pump," *Smart Materials and Structures,* vol. 14, p. 1511, 2005.

[19] G. M. Spinks, G. G. Wallace, J. Ding, D. Zhou, B. Xi, and J. Gillespie, "Ionic liquids and polypyrrole helix tubes: bringing the electronic Braille screen closer to reality," in *Smart Structures and Materials*, 2003, pp. 372-380.

[20] J. D. W. Madden, N. A. Vandesteeg, P. A. Anquetil, P. G. A. Madden, A. Takshi, R. Z. Pytel*, et al.*, "Artificial muscle technology: physical principles and naval prospects," *IEEE Journal of Oceanic Engineering,* vol. 29, pp. 706-728, 2004.

[21] P. A. T. Anquetil, "Large contraction conducting polymer molecular actuators," PhD, Massachusetts Institute of Technology, 2004.

[22] J. D. W. Madden, "Conducting polymer actuators," PhD, Massachusetts Institute of Technology, 2000.

[23] X. Chen and O. Inganäs, "Doping-induced volume changes in poly (3-octylthiophene) solids and gels," *Synthetic Metals,* vol. 74, pp. 159-164, 1995.

[24] M. Fuchiwaki, W. Takashima, and K. Kaneto, "Comparative study of electrochemomechanical deformations of poly (3-alkylthiophene) s, polyanilines and polypyrrole films," *Japanese Journal of Applied Physics,* vol. 40, p. 7110, 2001.

[25] Q. Pei and O. Inganäs, "Electrochemical muscles: bending strips built from conjugated polymers," *Synthetic Metals,* vol. 57, pp. 3718-3723, 1993.

[26] E. Smela, W. Lu, and B. R. Mattes, "Polyaniline actuators: Part 1. PANI (AMPS) in hcl," *Synthetic Metals,* vol. 151, pp. 25-42, 2005.

[27] G. M. Spinks, V. Mottaghitalab, M. Bahrami-Samani, P. G. Whitten, and G. G. Wallace, "Carbon-nanotube-reinforced polyaniline fibers for high-strength artificial muscles," *Advanced Materials,* vol. 18, pp. 637-640, 2006.

[28] W. Takashima, M. Fukui, M. Kaneko, and K. Kaneto, "Electrochemomechanical deformation of polyaniline films," *Japanese Journal of Applied Physics,* vol. 34, p. 3786, 1995.

[29] B. Xi, V.-T. Truong, P. Whitten, J. Ding, G. M. Spinks, and G. G. Wallace, "Poly (3-methylthiophene) electrochemical actuators showing increased strain and work per cycle at higher operating stresses," *Polymer,* vol. 47, pp. 7720-7725, 2006.

[30] L. Bay, K. West, P. Sommer-Larsen, S. Skaarup, and M. Benslimane, "A conducting polymer artificial muscle with 12% linear strain," *Advanced Materials,* vol. 15, pp. 310-313, 2003.

[31] S. Hara, T. Zama, W. Takashima, and K. Kaneto, "Free-standing gel-like polypyrrole actuators doped with bis(perfluoroalkylsulfonyl)imide exhibiting extremely large strain," *Smart Materials and Structures,* vol. 14, pp. 1501-1510, 2005.

[32] S. Hara, T. Zama, W. Takashima, and K. Kaneto, "TFSI-doped polypyrrole actuator with 26% strain," *Journal of Materials Chemistry,* vol. 14, pp. 1516-1517, 2004.

[33] S. Hara, T. Zama, W. Takashima, and K. Kaneto, "Tris(trifluoromethylsulfonyl)methide-doped polypyrrole as a conducting polymer actuator with large electrochemical strain," *Synthetic Metals,* vol. 156, pp. 351-355, 2006.

[34] S. Hara, T. Zama, W. Takashima, and K. Kaneto, "Gel-like polypyrrole based artificial muscles with extremely large strain," *Polymer Journal,* vol. 36, pp. 933-936, 2004.

[35] M. Castillo-Ortega, M. Inoue, and M. Inoue, "Chemical synthesis of highly conducting polypyrrole by the use of copper (II) perchlorate as an oxidant," *Synthetic Metals,* vol. 28, pp. 65-70, 1989.

[36] H. O. Chan, "Electrically conductive graft copolymers of poly (methyl methacrylate) with varying polypyrrole and poly (3-alkylpyrroles) contents," *Journal of Materials Chemistry,* vol. 8, pp. 2347-2352, 1998.

[37] H. Bai and G. Shi, "Gas sensors based on conducting polymers," *Sensors,* vol. 7, pp. 267-307, 2007.

[38] E. Genies, G. Bidan, and A. Diaz, "Spectroelectrochemical study of polypyrrole films," *Journal of Electroanalytical Chemistry and Interfacial Electrochemistry,* vol. 149, pp. 101-113, 1983.

[39] S. Y. Chu, H. Peng, P. A. Kilmartin, G. A. Bowmaker, R. P. Cooney, and J. Travas-Sejdic, "Effect of deposition current density on the linear actuation behaviour of PPy (CF 3 SO 3) films," *Current Applied Physics,* vol. 8, pp. 324-327, 2008.

[40] J. Sui, J. Travas-Sejdic, S. Y. Chu, K. C. Li, and P. A. Kilmartin, "The actuation behavior and stability of p-toluene sulfonate doped polypyrrole films formed at different deposition current densities," *Journal of Applied Polymer Science,* vol. 111, pp. 876-882, 2009.

[41] A. Ashrafi, M. Golozar, and S. Mallakpour, "Morphological investigations of polypyrrole coatings on stainless steel," *Synthetic Metals,* vol. 156, pp. 1280-1285, 2006.

[42] M. Gandhi, P. Murray, G. Spinks, and G. Wallace, "Mechanism of electromechanical actuation in polypyrrole," *Synthetic Metals,* vol. 73, pp. 247-256, 1995.

[43] T. F. Otero, "Soft, wet, and reactive polymers. Sensing artificial muscles and conformational energy," *Journal of Materials Chemistry,* vol. 19, pp. 681-689, 2009.

[44] G. Maia, R. M. Torresi, E. A. Ticianelli, and F. C. Nart, "Charge compensation dynamics in the redox processes of polypyrrole-modified electrodes," *The Journal of Physical Chemistry,* vol. 100, pp. 15910-15916, 1996.

[45] S. Bruckenstein, J. Chen, I. Jureviciute, and A. R. Hillman, "Ion and solvent transfers accompanying redox switching of polypyrrole films immersed in divalent anion solutions," *Electrochimica Acta,* vol. 54, pp. 3516-3525, 2009.

[46] L. Bay, T. Jacobsen, S. Skaarup, and K. West, "Mechanism of actuation in conducting polymers: osmotic expansion," *The Journal of Physical Chemistry B,* vol. 105, pp. 8492-8497, 2001.

[47] H. Okuzaki, T. Kondo, and T. Kunugi, "Characteristics of water in polypyrrole films," *Polymer,* vol. 40, pp. 995-1000, 1999.

[48] T. Zama, S. Hara, W. Takashima, and K. Kaneto, "Fast response polypyrrole actuators with auxiliary electrodes," *Japanese Journal of Applied Physics,* vol. 44, pp. 8153-8160, 2005.

[49] S. Hara, T. Zama, W. Takashima, and K. Kaneto, "Polypyrrole-metal coil composite actuators as artificial muscle fibres," *Synthetic Metals,* pp. 47-55, 2004.

[50] P. Laborde-Lahoz, W. Maser, T. Martinez, A. Benito, T. Seeger, P. Cano*, et al.*, "Mechanical characterization of carbon nanotube composite materials," *Mechanics of Advanced Materials and Structures,* vol. 12, pp. 13-19, 2005.

[51] J. Rodriguez, H. Grande, T. Otero, and H. Nalwa, *Handbook of organic conductive molecules and polymers*. John Wiley & Sons Ltd: New York, vol. 2, 1997.

[52] Y. Li and R. Qian, "Electrochemical overoxidation of conducting polypyrrole nitrate film in aqueous solutions," *Electrochimica Acta,* vol. 45, pp. 1727-1731, 2000.

[53] T. Otero, H. Grande, and J. Rodriguez, "Conformational relaxation during polypyrrole oxidation: from experiment to theory," *Electrochimica Acta,* vol. 41, pp. 1863-1869, 1996.

[54] G. M. Spinks, B. Xi, D. Zhou, V.-T. Truong, and G. G. Wallace, "Enhanced control and stability of polypyrrole electromechanical actuators," *Synthetic Metals,* vol. 140, pp. 273-280, 2004.

[55] T. F. Otero, M. Marquez, and I. J. Suarez, "Polypyrrole: diffusion coefficients and degradation by overoxidation," *The Journal of Physical Chemistry B,* vol. 108, pp. 15429-15433, 2004.

CHAPTER 2

APPARATUS FOR AND PERFORMANCE OF SEQUENTIAL GROWTH OF POLYPYRROLE-METAL COIL COMPOSITE POLYMERS

2.1 Abstract

This dissertation introduces a new electroactive polymer (EAP) actuator technology that allows for systematic, sequential growth of polypyrrole-metal coil composite actuators. The EAP material is synthesized in a specific apparatus with an embedded metal helix that acts not only as a support, but as an embedded working electrode for increased electrical conductivity during actuation; this provides a means by which to perform additional polymer growth stages. The additional growth is shown to increase electrical capacitance and mechanical force generation. The ability for additional growth during operation adds a unique functionality to biomimetic actuator technology that is similar to the capabilities of biological muscle.

2.2 Introduction

Due to the current interest and exploration of biologically inspired actuator technologies, electroactive polymers (EAPs) have been used in a wide range of

devices and sensors [1-6]; one of the most exciting applications being artificial muscles [7-10]. Human muscle and ionic EAPs are both polymeric materials that operate in a chemical bath with electrical excitation for actuation and have an inherent mechanical response. Comparing the mechanical performance, EAPs exhibit lower strain rates, but higher activation stresses and power densities [11]. Nonetheless, EAPs have achieved strain rates over 10% s-1, strains exceeding 20% (including recoverable strains of 14%), and stresses over 20 MPa [12-16]. One aspect of human muscle not yet compared to EAP actuators is the ability to improve during periods of additional growth. This is now possible with the inclusion of a metal helix working electrode and a sequential growth synthesis process.

Embedding a helix in a tubular polypyrrole actuator has resulted in improved performance over film and tubular geometries without an additional helix electrode [16]. The metal helix acts as a support structure to hold the polymer form and direct the inherent three-dimensional shape change along the axis of the helix, assists in distributing the charge throughout the polymer (additional electrodes have been shown to improve performance in polypyrrole films [17]), and performs as a working electrode within the polymer material. Sequential growth has been shown to produce higher density polypyrrole films in a fraction of the time needed to synthesize polypyrrole by previous methods [18]. This work uses sequential growth to first create a polypyrrole-metal coil composite actuator, and then to continuously modify the actuator performance and electrochemical response in response to changing demands or degradation of the actuator. This

actuator technology would be ideal for autonomous robots that operate under conditions where minimizing actuator weight is of high priority and actuator demands are not well known. The ability of this polymeric actuator material to successively regrow and evolve makes this system able to mimic the more advanced functions of human muscle.

2.3 Sequential Growth Apparatus

The ability to perform multiple stages of sequential growth necessitates the use of a specific apparatus that allows for the switching of growth and actuation solutions while also permitting mechanical performance testing. The unique test cell used here was modeled after a previous hollow polypyrrole fiber actuator test cell that encapsulates the actuator, counter electrode, and actuation electrolyte in a tube, and is shown in Fig. 2.1 [16]. The test cell also allows for strain measuring by attaching the actuator to a lever that registers the displacement on a ruler.

The custom test cell used here consists of a glass tube that is capped with form-fitting Delrin pucks and rubber gaskets (as shown in Fig. 2.2). The tube and pucks are held together to be airtight using three equally spaced bolts that clamp the assembly together with thumb nuts. The top Delrin puck is affixed with the reference and counter electrodes to allow for easy removal and electrode connections. The bottom clamp holds the actuator with an alligator clip (not shown in Fig. 2.2), which is also connected to a lead for the working electrode. Holes in the top puck allow for access to the actuator and holes to insert any

electrolytic fluid. The bottom puck has a hole for flushing out the electrolytic fluid after the specified operational step is completed. For testing of a polypyrrole-metal coil composite actuator, the actuator is secured to the alligator clip on the bottom puck; then, the gaskets, glass tube, and opposite puck are assembled and sealed with the screws and thumb nuts. The assembled test cell can then be used in the custom testing apparatus where it can be connected to the electrolytic fluid stores and mechanical testing sensors. The different testing configurations are shown in Fig. 2.3.

The testing apparatus is split into a front section (shown in Fig. 2.4) and rear section (shown in Fig. 2.5). The front section holds the test cell described above, along with a linear variable differential transducer (LVDT) to measure displacement, and a force sensor to measure actuator force output.

The different sensors are utilized by running high-tensile fishing from the actuator and over pulleys to reach the desired sensor. The rear section holds bottles for the actuation solution, growth solution, ethanol wash solution, power source, and peristaltic pump and nitrogen tank (not pictured in Fig. 2.5).

The nitrogen tank is used not only to dry out the actuator between growth stages, but pressurizes the solution bottles. Flow from the pressurized solution bottles is controlled using tubing sections that are held kinked on servo motors. The servo motors each hold two kinked tubing sections. Turning the servo from this base position will further kink one tubing section and unkink the opposite tubing section, thereby allowing the tubing's fluid to flow into the cell. The flow concept is shown in Fig. 2.6.

The total of four tubing sections that feed the test cell stem from the growth solution bottle, actuation solution bottle, ethanol flush bottle, and the nitrogen gas tank. Since the test cell is not completely sealed, the tubing section originating in the nitrogen gas tank can be left slightly open to allow the test cell to have a slightly positive nitrogen gas pressure to stop natural cell oxidation from the environment. The experimental apparatus front section is shown in Fig. 2.7, and the rear section is shown in Fig. 2.8.

2.4 Methods

2.4.1 Reagents and Materials

Methyl benzoate, tetrabutylammonium tetrafluoroborate (TBABF4), sodium tetrafluoroborate (NaBF4), ethanol, and acetone were purchased from Sigma-Aldrich Inc. and used as-received. Pyrrole monomer (Sigma-Aldrich) was distilled before use. The polymerization solution, or growth solution, contained pyrrole (0.25 mol dm−3) and TBABF4 (0.2 mol dm−3) mixed in methyl benzoate. The actuation solution was an aqueous NaBF4 (1.0 mol dm−3) solution [12]. Working electrode materials consisted of 0.050 mm tungsten wire (Goodfellow) and 0.500 mm nitinol wire (or shape memory alloy (SMA); Dynalloy, Inc.). The counter electrode was acetone rinsed stainless steel mesh (McMaster-Carr), and silver wire (Goodfellow) served as the reference electrode.

2.4.2 Electrochemical Synthesis

Synthesis was performed using a Hokuto-Denko potentio-galvanostat model HA-151 in a conventional three-electrode setup. The working electrode was created by winding the smaller diameter tungsten wire around the nitinol core with a custom coil winder. A custom test cell was used that allows for ease of electrode connection and electrolytic fluid addition and removal.

The polypyrrole was synthesized using a 3 mA/cm2 excitation for 2 minute cycles, which were interrupted with an ethanol wash and drying under nitrogen gas. A total of 8 cycles were performed and all films were grown at room temperature (approximately 21° C). After the 8 cycles, core removal was accomplished by placing the polypyrrole coated core and helix in boiling distilled water, thereby contracting the nitinol core to ease pulling out of the core physically. Electrode connection to the polymer-metal helix composite actuator was created by inserting shorter sections of the core material into each end and secured with silicon adhesive. The resulting polypyrrole-metal coil composite actuators measured between 1cm and 3cm in length. A schematic of the entire process is shown in Fig. 2.9.

2.4.3 Characterization

The completed actuators are placed back in the test cell, and the cell filled with actuation electrolyte solution. After running tests, the growth process was repeated, and the effect upon the polymer analyzed using a data acquisition (DAQ) card (National Instruments USB-6009) connected to the potentiostat and

to the control circuit for the force sensor (Omega LCL-227G load cell).

An FEI NanoNova scanning electron microscope (SEM) was used to take the surface images. LabVIEW was used to control the potentiostat and record response data. Post-processing was performed in SIMULINK.

Initial creation and subsequent growth and actuation of the polymer-metal coil composite actuators follow similar protocol, which is outlined in Fig. 2.9. Initial construction uses a custom coil winder to wrap tungsten wire over a nitinol core wire. This tungsten helix-wrapped nitinol core acts as the working electrode for the initial growth steps. The initial polypyrrole growth consists of 8 cycles of electrical excitation in the growth solution, consisting mainly of pyrrole and a doping ion, followed by an ethanol wash and nitrogen drying cycle. All growth and actuation is performed in a custom test cell that allows for easy electrode connection and specific fluid and gas addition and removal. At this point, the nitinol core is physically removed after submerging the polypyrrole-coated tungsten helix and nitinol core in boiling distilled water. The water is therefore above the shape transition temperature of the nitinol core to instigate core contraction. This core contraction improves the ease with which the nitinol core can be removed to leave a hollow tube of polypyrrole with the tungsten helix embedded. Small bits of the core material are slightly inserted back into each end of the hollow polypyrrole tube and secured with silicon adhesive. The exposed sides of these wire sections act as actuator leads and connection points for the completed actuator. The completed actuator is placed back in the test cell for actuations and additional growth tests, where the additional growth tests

undergo the same growth protocol with the exception of the nitinol core in the actuator/working electrode.

2.5 Results and Discussion

2.5.1 Short-Term Size and Strength

The SEM surface images in Fig. 2.10 show a clear distinction between the smoother texture of the polymer-metal coil composite actuator using sequential growth and the more clustered, less-dense, or ‘cauliflower,’ texture of the actuator using continuous growth. The cauliflower texture is common in continuously grown polypyrrole actuators where monomer diffusion limits the rate of polymerization. Greatly increasing the excitation current (by a factor of twelve comparing these two growth strategies) increases polymerization rate, but also sacrifices polymer structure by increasing undesired oligomer growth. This undesired growth is mitigated with the ethanol washes and nitrogen drying, both acting to restrict undesired growth and oxidation when increasing the excitation current to reduce the growth period. The process of sequential growth aids not only in producing denser, smoother polypyrrole films, but allows for production in a fraction of the time (tens of minutes versus hours). The additional benefit of using sequential growth in this work is that after an actuation cycle, sequential growth can be employed again to adjust performance of the actuator system within the lifetime of the actuator.

Experiments were directed at exploring the electrochemical response through cyclic voltammetry (CV), as well as the mechanical performance through

measuring force output, and both results are shown in Fig. 2.11. To analyze the electrochemical response, the sample at each growth stage was cycled once between -1 and 1 volts at a rate of 50 mV/s. If this plot exhibited loops at the oxidative or reduced peaks where the curve crosses itself, then voltages where the intersections occurred were used as the new voltage bounds for CV tests lasting at least 200 seconds at 50 mV/s. Analyzing the cyclic voltammagrams for each stage of growth for one sample shows both increasing cathodic and anodic capacitances. Looking at the right side of the CV plot in Fig. 2.11(a) (positive voltage potential), the increase in number of growth cycles results in an increase in current density. The left side of the plot (negative voltage potential) also shows a magnitude increase in current density, although in the negative direction. The increase in negative potential voltage magnitude combined with the increase in current density (while keeping a similar curve shape) results in a larger anodic capacitance. Both anodic and cathodic capacitances increase, and are displayed in Fig. 2.11(b). These capacitances are generally normalized with the actuator mass, but the change in mass was not measured since removing and returning the actuator from the cell between additional growth cycles could disrupt electrochemical measurements, skew comparisons, and negate one of the main purposes of the custom test cell. Even small adjustments in electrode spacing can affect electrochemical measurements. The manifestation of the increase in cathodic capacitance was observed through physical testing on a separate sample where a positive step current input of 100 mA resulted in an increase in force output.

The polymer-metal coil composite actuators were held at a fixed length with a slight preload. A 100 mA current step excitation was applied at 5 seconds. Fig. 2.11(c) shows the results for 1 sample at three different growth stages. All three tests exhibit a rise time of approximately 5-6 seconds to reach their steady-state force measurements. It is more important to note, though, that increasing the number of growth steps increases the force generated with the same excitation current. Given that the excitation current had a positive magnitude, this increase in force output correlates with the general increase in cathodic capacitance displayed by the CV tests performed at different growth steps. More specifically, a higher capacitance (created by increasing capacitive polymeric material) allows for a higher charge storage within the polymer, which increases ion mobility capability. Since the ability of the polymer to deform and produce force is a product of mass transfer, more polymeric material will produce more force, but also provide more material for ions to move through for polymer chain insertion or rejection. This means more time is needed for ion propagation, and therefore more time for mechanical response. More testing is being pursued to investigate this tradeoff between speed and strength with these polymer-metal coil composite actuators grown sequentially. This is all in effort to create an actuator system that is not only adjustable for an optimal means, but adjustable by individual actuators for specific, independent tasks.

2.5.2 Extended Lifetime

An additional benefit of sequential growth was repairing degradation over longer actuation tests. One of the main drawbacks from using conducting polymer actuators (especially when comparing to human muscle performance) is cycle life. Preliminary tests illustrate that reducing the regrowth time does not greatly increase polymer material, and therefore strength, but can be used to rectify the decrease in performance over multiple cycles. The initial polymer was fabricated with the methods described above and cycled between -1 V and 1 V at 200 mV/s for 4000 cycles. After 5 cycles, if the cycling results showed the behavior looping back upon itself, then the CV test was run for five samples between those limits. The 5 cycle CV test was performed again at cycle 4000. The amount of growth time used in the initial synthesis was decreased by 75% to only be applied for 30 seconds. The results are shown below in Fig. 2.12.

The results shown in Fig. 2.12 show the evolution from the 5^{th} to the 4000^{th} cycle in the left column. In these tests, the earlier cycle is shown in black and the later cycle is shown in red. The trend is for the CV curve to decrease in both aniodic and cathodic potential as the number of cycles increase. The exception here is in Actuation Stage 2 where the curve seems to shift overall behavior in a positive current and voltage direction. This is the reverse behavior from the previous growth step. The difference before and after a growth stage is performed is shown in the right column. The same color scheme for growth cycle number is used here, so the overall timeline moves from the 4000^{th} cycle in red to the 5^{th} cycle in black after a growth stage. The test progression is shown as

going left to right, and then top to bottom in Fig. 2.12 (Actuation Stage 1 -> Growth Stage 1 -> Actuation Stage 2 -> Growth Stage 2 -> Actuation Stage 3 -> Growth Stage 3). The trends here display an increase in anodic and cathodic potential due to the growth. The shift in behavior shown at Actuation Stage 2 is the reverse of movement from Growth Stage 1, which is the growth stage directly before Actuation Stage 2 is performed. In Growth Stage 1, the actuator CV behavior shifts in both a negative current density and negative potential direction. This is likely due to a shift in the working electrode within the test cell that corrects itself during the next actuation stage. The comparison can still be seen that the growth increases the area of the CV curve while still retaining the same shape. The curve shifts back to the original position in Actuation Stage 2, and the CV curve shows a decrease in area as the actuation cycles are increased.

2.6 Conclusion

The ability to adjust performance and regrow a polymer during its lifetime advances both the field of polymers and the field of actuators. The method of sequential growth has been applied to a metal helix geometry and tested over multiple growth and actuation cycles to exhibit an increase in capacitance and force output, or strength. Specifically here, applying sequential growth to a metal helix actuator geometry, and then allowing additional growth after periods of actuation (using the sequential growth method, again) increases the similarity between artificial and actual muscles.

2.7 Acknowledgements

This work was funded by the National Science Foundation (NSF) (grant DGE-0654414 and NSF IGERT grant CMMI-1031848). The authors thank Dr. Matt DeLong for taking the scanning electron microscope images and Dr. Debra Mascaro for providing research facilities.

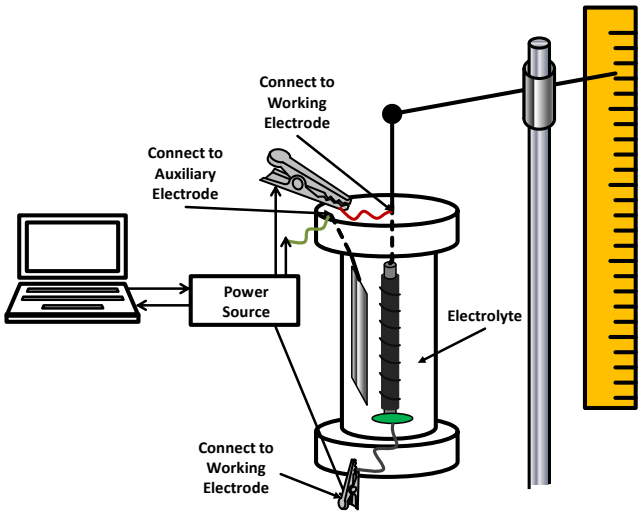

Figure 2.1. The testing cell apparatus adapted from [16]. The polypyrrole actuator is encapsulated in a tube to hold the electrolyte, is attached to a lever to measure strain, and is controlled with a computer.

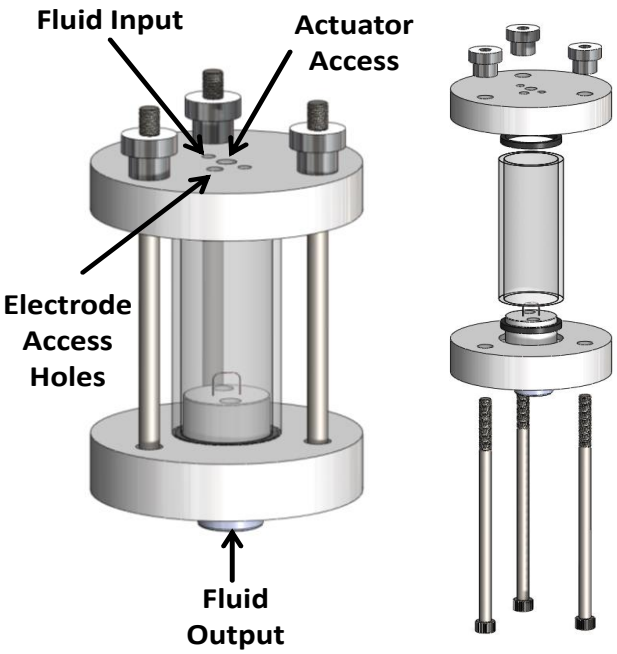

Figure 2.2. Custom test cell design with a glass tube capped with Delrin pucks and sealed with rubber O-rings and held with bolts and nuts.

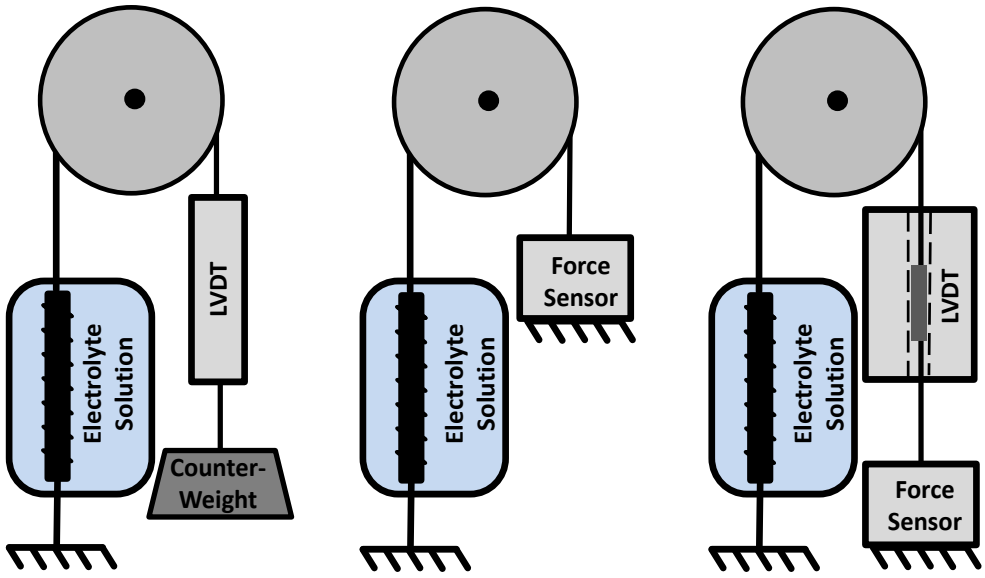

Figure 2.3. The custom testing setup to measure displacement, force, or both displacement and force simultaneously.

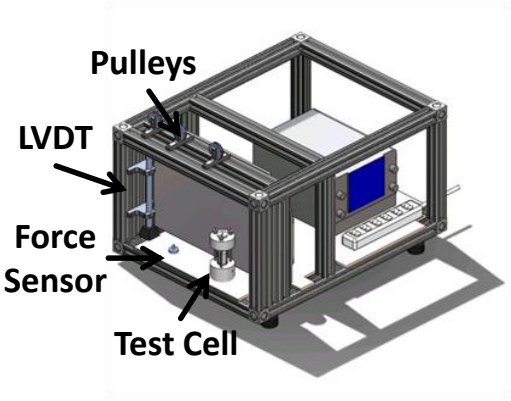

Figure 2.4. Design for the custom test apparatus with a view of the front section.

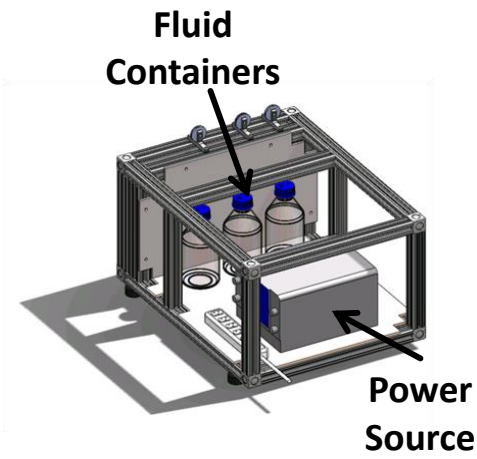

Figure 2.5. Design for the custom test apparatus with a view of the rear section.

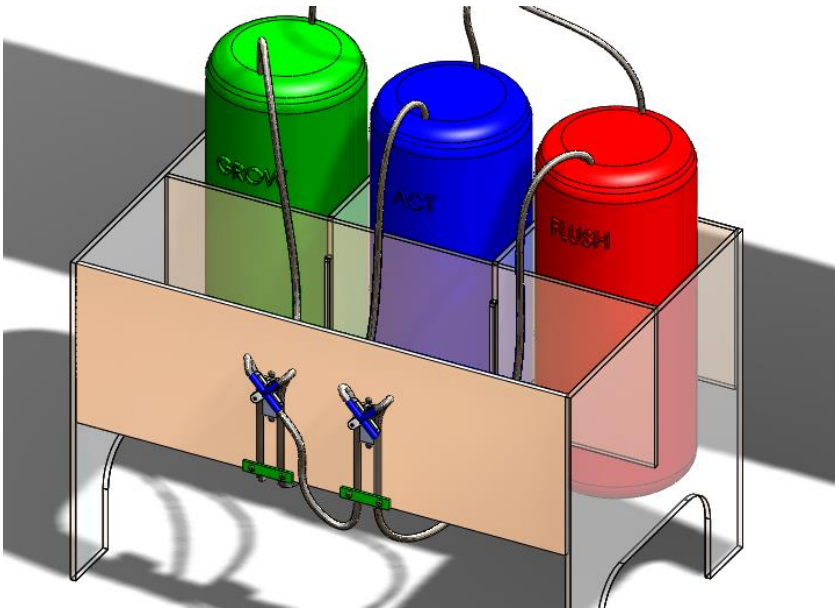

Figure 2.6. Concept design for the custom test apparatus input flow control. The separate flow tubes are kinked or unkinked by servo motors.

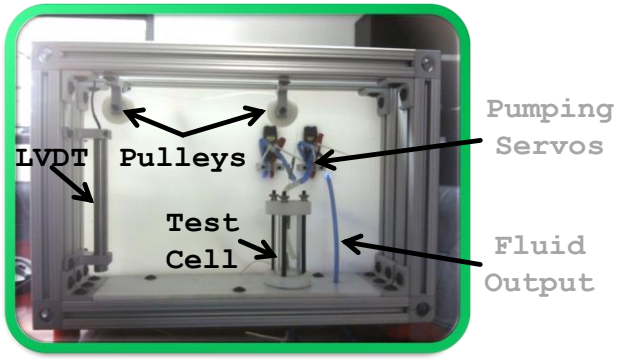

Figure 2.7. Construction for the custom test apparatus with a view of the front section.

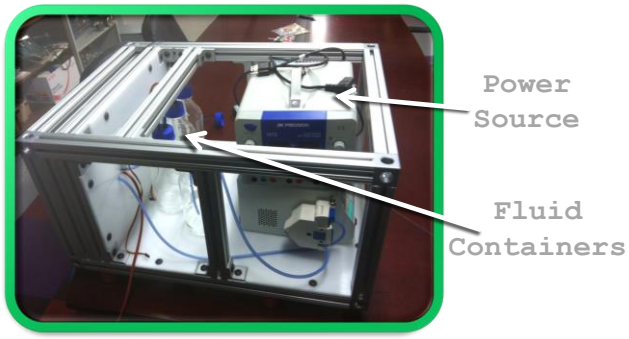

Figure 2.8. Construction for the custom test apparatus with a view of the rear section.

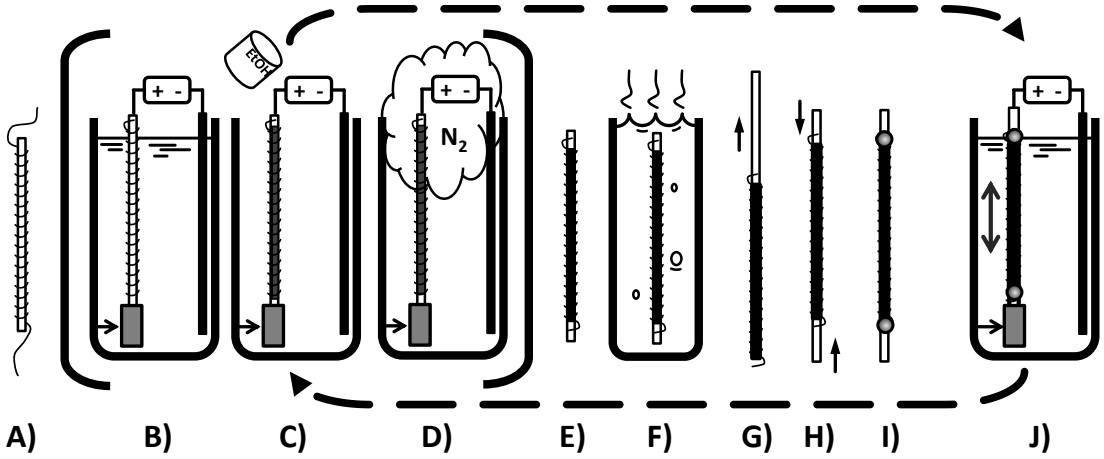

Figure 2.9. The entire initial synthesis process is described. (A) 50 µm tungsten wire is wrapped around the 500 µm nitinol wire as a helix; (B) the polymer is synthesized with the electrodes placed in the growth solution for 2 minutes at room temperature; (C) the growth solution is drained and the polymer rinsed with ethanol (EtOH); (D) the cell is dried with nitrogen gas, and B,C, and D are repeated eight times; (E) the working electrode now coated with polypyrrole is removed from the test cell; (F) the working electrode is placed in boiling distilled water to activate the nitinol core and contract; (G) the working electrode is quickly removed from the boiling distilled water and the contracted nitinol core removed; (H) smaller sections of the core material are inserted into each side of the polymer-metal tube; (I) the electrode sections are attached using silicon adhesive to complete actuator construction; (J) an actuation program is performed and then the entire system can move from (J) to ((B),(C),(D)) and back as needed for optimization. Diagram format adapted from [19].

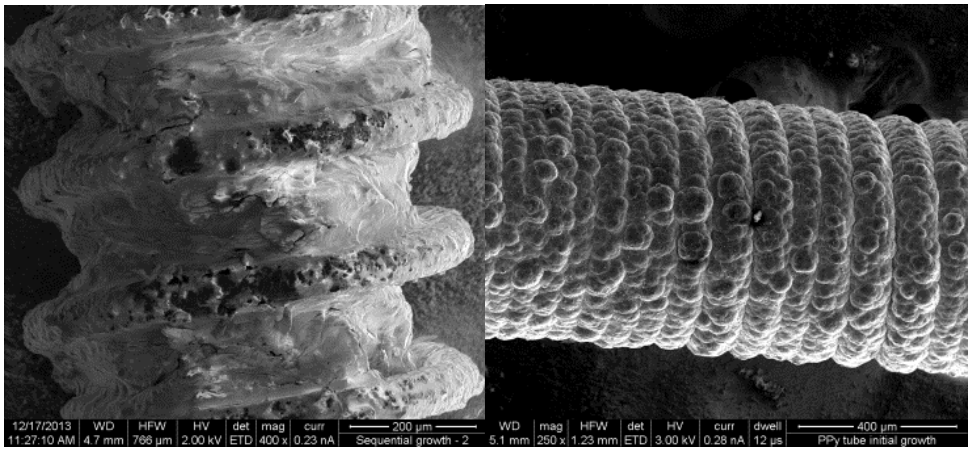

Figure 2.10. SEM photographs of polypyrrole metal-coil composite actuators that have been synthesized using (A) sequential growth and (B) continuous growth.

A)

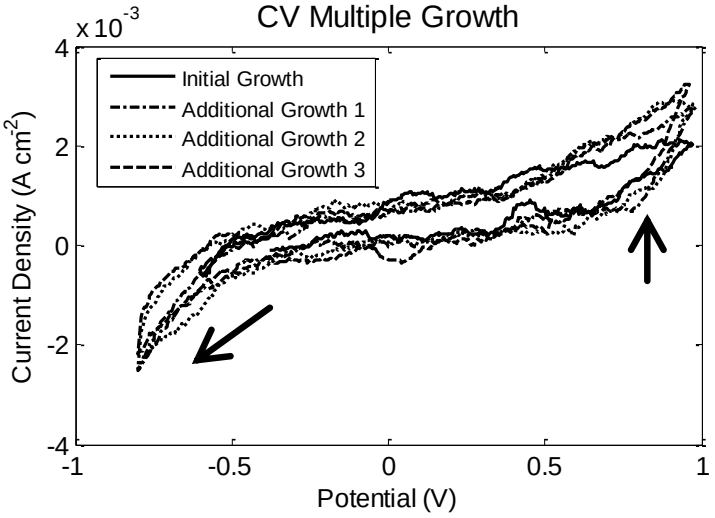

B)

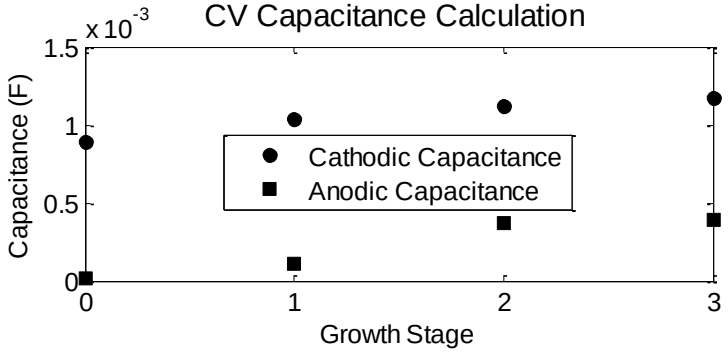

C)

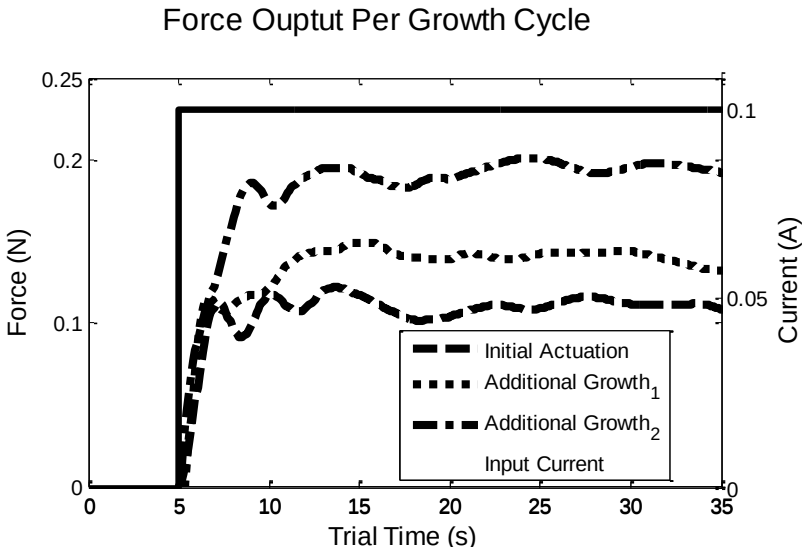

Figure 2.11. These plots show the change in capacitance and force output over multiple growth cycles. (A) shows the 5th cycle of the cyclic voltammagram for multiple growth steps showing an increase in capacitance. (B) shows the cathodic and anodic capacitances for the CV tests displayed in (A). (C) shows the force output for a sample during multiple growth cycles (adapted from [20]).

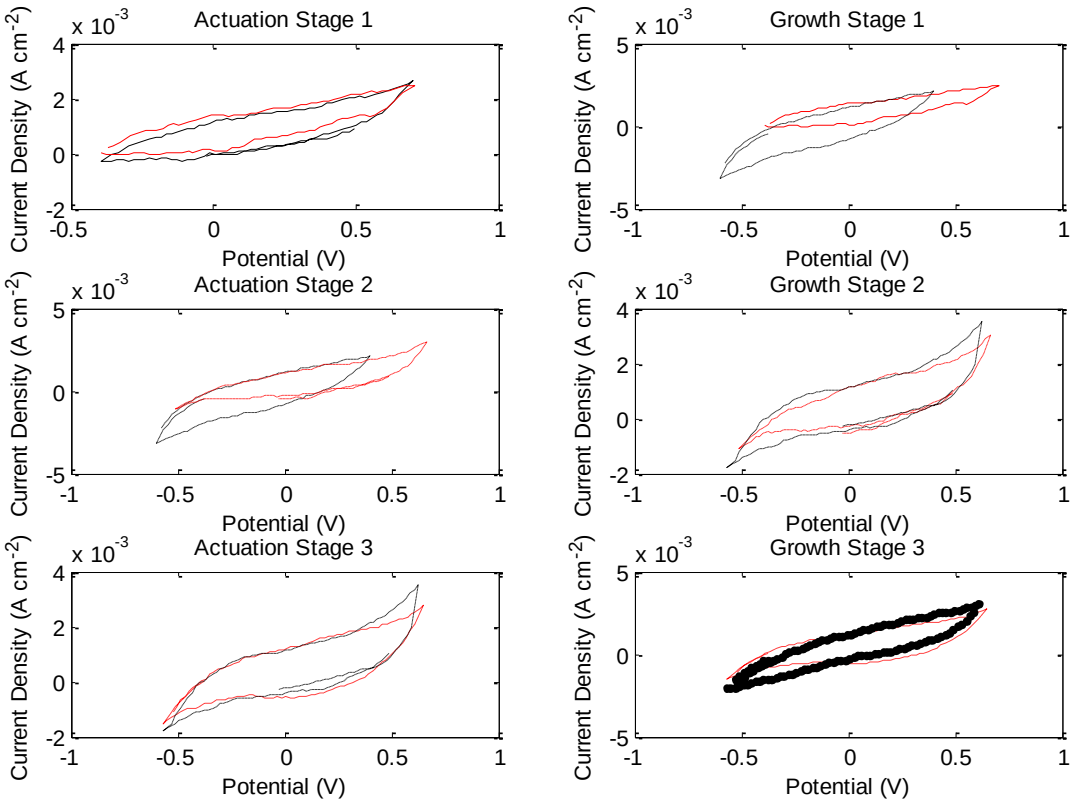

Figure 2.12. Cyclic voltammetry tests for performance repair tests. The plots on the left show the 5th cycle for the sample in black, and the 4000th cycle in red for the same sample. The plots on the right show the 4000th cycle in red, and the 5th cycle of the same sample after a decreased growth stage has been performed.

2.8 References

[1] G. M. Spinks, G. G. Wallace, J. Ding, D. Zhou, B. Xi, and J. Gillespie, "Ionic liquids and polypyrrole helix tubes: bringing the electronic Braille screen closer to reality," in *Smart Structures and Materials*, 2003, pp. 372-380.

[2] J. D. Madden, N. A. Vandesteeg, P. A. Anquetil, P. G. Madden, A. Takshi, R. Z. Pytel*, et al.*, "Artificial muscle technology: physical principles and naval prospects," *Oceanic Engineering, IEEE Journal of,* vol. 29, pp. 706-728, 2004.

[3] T. Shoa, J. D. Madden, T. Mirfakhrai, G. Alici, G. M. Spinks, and G. G. Wallace, "Electromechanical coupling in polypyrrole sensors and actuators," *Sensors and Actuators A: Physical,* vol. 161, pp. 127-133, 2010.

[4] Y. Wu, D. Zhou, G. M. Spinks, P. C. Innis, W. Megill, and G. G. Wallace, "TITAN: a conducting polymer based microfluidic pump," *Smart Materials and Structures,* vol. 14, p. 1511, 2005.

[5] Y. Wu, G. Alici, G. M. Spinks, and G. G. Wallace, "Fast trilayer polypyrrole bending actuators for high speed applications," *Synthetic Metals,* vol. 156, pp. 1017-1022, 2006.

[6] E. W. Jager, "Actuators, biomedicine, and cell-biology," in *SPIE Smart Structures and Materials+ Nondestructive Evaluation and Health Monitoring*, 2012, pp. 834006-834006-10.

[7] R. Baughman, "Conducting polymer artificial muscles," *Synthetic Metals,* vol. 78, pp. 339-353, 1996.

[8] E. Smela, "Conjugated polymer actuators for biomedical applications," *Advanced Materials,* vol. 15, pp. 481-494, 2003.

[9] Y. Tadesse, R. W. Grange, and S. Priya, "Synthesis and cyclic force characterization of helical polypyrrole actuators for artificial facial muscles," *Smart Materials and Structures,* vol. 18, 2009.

[10] T. W. Secord and H. H. Asada, "A humanoid foot with polypyrrole conducting polymer artificial muscles for energy dissipation and storage," in *Robotics and Automation, 2007 IEEE International Conference on*, 2007, pp. 2904-2909.

[11] I. W. Hunter and S. Lafontaine, "A comparison of muscle with artificial actuators," in *Solid-State Sensor and Actuator Workshop, 1992. 5th*

Technical Digest., IEEE, 1992, pp. 178-185.

[12] S. Hara, T. Zama, W. Takashima, and K. Kaneto, "Polypyrrole-metal coil composite actuators as artificial muscle fibres," *Synthetic Metals,* pp. 47-55, 2004.

[13] S. Hara, T. Zama, W. Takashima, and K. Kaneto, "Free-standing polypyrrole actuators with response rate of 10.8%s-1," *Synthetic Metals,* vol. 149, pp. 199-201, 2005.

[14] S. Hara, T. Zama, W. Takashima, and K. Kaneto, "TFSI-doped polypyrrole actuator with 26% strain," *Journal of Materials Chemistry,* vol. 14, pp. 1516-1517, 2004.

[15] P. A. Anquetil, D. Rinderknecht, N. A. Vandesteeg, J. D. Madden, and I. W. Hunter, "Large strain actuation in polypyrrole actuators," in *Proc. of SPIE Vol*, 2004, p. 381.

[16] J. Ding, L. Liu, G. M. Spinks, D. Zhou, G. G. Wallace, and J. Gillespie, "High performance conducting polymer actuators utilising a tubular geometry and helical wire interconnects," *Synthetic Metals,* pp. 391-398, 2003.

[17] T. Zama, S. Hara, W. Takashima, and K. Kaneto, "Fast response polypyrrole actuators with auxiliary electrodes," *Japanese Journal of Applied Physics,* vol. 44, pp. 8153-8160, 2005.

[18] W. Zheng, J. M. Razal, G. M. Spinks, V. T. Truong, P. G. Whitten, and G. G. Wallace, "The role of unbound oligomers in the nucleation and growth of electrodeposited polypyrrole and method for preparing high strength, high conductivity films," *Langmuir,* vol. 28, pp. 10891-7, Jul 24 2012.

[19] J. Ding, D. Zhou, G. Spinks, G. Wallace, S. Forsyth, M. Forsyth*, et al.*, "Use of ionic liquids as electrolytes in electromechanical actuator systems based on inherently conducting polymers," *Chemistry of Materials,* vol. 15, pp. 2392-2398, 2003.

[20] J. Sarrazin and S. A. Mascaro, "Sequential growth and monitoring of a polypyrrole actuator system," in *SPIE Smart Structures and Materials+ Nondestructive Evaluation and Health Monitoring*, 2014, pp. 90563L-90563L-11.

CHAPTER 3

EXTENDED CONTROL: OPEN-LOOP CONTROL AND OPTIMAL PERFORMANCE PREDICTION FOR SEQUENTIALLY GROWN POLYPYRROLE-METAL COIL COMPOSITE ACTUATORS

3.1 Abstract

Electroactive polymer actuator systems have demonstrated performance and behavior similar to human muscle, especially with the recent development of sequential growth cycles during normal operation. The ability to grow sequentially presents a need for multiple growth stage modeling and performance optimization. This work uses simplified control algorithms to identify pertinent model parameters and predict the amount of additional growth needed to reach an optimal polymer actuator system performance. Performance is determined by an algorithm that uses frequency analyses to assign actuator speed and strength values. The optimal amount of growth selection is dependent upon the chosen weighting value. The simplified model accurately predicts the optimal amount of growth to within one stage of growth.

3.2 Introduction

Polypyrrole actuators have emerged as a viable actuator option for a range of robotic applications [1-5] and artificial muscles [6-9]. They have achieved stresses over 20 MPa, strains over 20 %, and strains rates over 10 %s-1 [10-14]. Electroactive polymer (EAP) actuators have not reached the strain and strain rates of human muscle, but do exhibit higher stresses and power densities [15]. Recent advances in polypyrrole actuator systems permit additional growth cycles during actuation cycles [16]. Multiple growth cycles allows for an artificial muscle actuation technology that can be adjusted over its lifetime, but also complicates the modeling and control of the actuator system. This paper presents a way in which to harness the multiple growth steps to achieve an optimal artificial muscle actuation system by analyzing and predicting performance over multiple growth cycles using a simplified actuator model.

Current models for the chemical-electrical system of polypyrrole actuators can be generally grouped into two categories: an admittance/impedance circuit model, and a multiple segment transmission line model. The admittance/impedance circuit model was first presented as a single loop that contains a voltage source, resistances for the electrolyte, electrodes and ion diffusion, a bulk capacitance, and a double-layer capacitance to represent the boundary between the polymer and the electrolyte solution [17]. The model may be simplified by neglecting the double-layer capacitance, due to its quick charging time compared to the rest of the system [18]. This model was used for robust control [19, 20] and expanded specifically for polypyrrole metal-coil

composite actuators [8].

Multiple segment transmission line models evolved by starting with an impedance model and splitting the impedance into multiple resistances and capacitances in an effort to more accurately model the electron (and resulting ion) transport and storage in the polymer system. The transmission line models allow for modeling polymer systems in multiple dimensions and for incorporating certain traits more specifically, such as charge transport, charge distribution, and rate limit effects [3, 21-26]. The polymer actuator system includes the polymer material, electrodes, and electrolytic solution.

Given the recent development that polypyrrole-metal coil composite actuator systems that can regrow during their lifetime, no model has been created that accurately represents the behavior of these actuators over multiple growth cycles. Creating such a model to cover multiple growth steps multiplies any problems found with models of a single stage of growth. Since nothing is known about the polymer evolution over multiple growth cycles, each growth step model needs to be initially treated like a completely different actuator system. This work presents a simplified model and algorithm to monitor performance of the actuator system, and determines the ideal amount of growth required to produce the optimal actuator for the desired performance metric. First, a simplified model for the polymer actuator system is constructed separating the electric and mechanical systems. This allows parameter identification using recursive least squares and state estimation algorithms. Once parameters are identified, the state-space representation can be formulated and a frequency analysis used in

conjunction with a performance cost equation to determine if the optimal amount of growth has been achieved on a mechanical performance basis.

3.3 Experimental Setup

The polypyrrole-metal coil composite actuators were created by combining previous compositions and geometries. The actuators were synthesized, actuated, tested, and re-grown through the use of a custom test cell.

3.3.1 Conducting Polymer Actuator Structure and Synthesis

The polypyrrole-metal coil composite actuators were galvanostatically synthesized in a three-electrode cell (Fig. 3.1) containing an electrolytic solution consisting of 0.25 mol dm-3 polypyrrole, 0.2 mol dm-3 tetrabutylammonium tetrafluoroborate (TBABF4), and methyl benzoate. The working electrode was a 0.250 mm diameter nitinol wire wrapped with a 0.050 mm tungsten wire in a helical geometry. The counter electrode was stainless steel mesh, and the reference electrode was silver wire. Synthesis consisted of 8 sequential cycles; each with a galvanostatic growth step, an ethanol rinse step, and a nitrogen gas drying step (as outlined for polypyrrole film actuators in [27]). Each galvanostaic growth step was performed at 0.001 A for 120 seconds. After the conclusion of the eighth growth cycle, the actuator was heated in boiling distilled water to make the nitinol core contract and ease core removal. The remaining polypyrrole cylinder with the embedded tungsten helix is completed as an actuator by inserting small lengths of core metal in each end to act as electrical leads, and

secured with silicon adhesive. The synthesis scheme is shown in Fig. 3.1.

The actuation solution consisted of an aqueous solution of 1.0 mol dm^{-3} of sodium tetrafluoroborate ($NaBF_4$). Additional growth steps between actuation cycles use the same electrolytic growth solution, galvanostatic excitation and time, and rinse and drying protocol. Electrical excitation was controlled with a Hokuto-Denko HA-151 potentio-galvanostat, and data recorded using LabVIEW.

All chemicals were obtained from Sigma-Aldrich and received as-is, except for the pyrrole which was distilled and stored at approximately 5°C. Electrode materials were obtained from Goodfellow, except for the stainless steel mesh which was obtained from McMaster-Carr and rinsed with acetone before use. All growth and tests were performed at room temperature.

3.3.2 Test Cell Setup

The test cell is made from a glass tube capped on the top and bottom with a rubber O-ring and Delrin puck. The Delrin pucks have holes to accommodate the exchange of solutions for facilitating multiple growth and actuation cycles. The cell is held together by three screws and thumb nuts, allowing for ease of removal and replacement of actuators (Fig. 3.2). During a test routine, the electrodes are sealed in the cell and the eight initial synthesis steps performed. At this point, the working electrode, coated in polypyrrole, must be removed from the cell so that the nitinol core can be removed from the tungsten helix of the working electrode. Once the polypyrrole and embedded tungsten helix actuator have the electrical leads affixed, the actuator is returned to the cell and the

testing actuation and additional growth cycles are performed.

3.3.3 Displacement Measurement System

Actuator displacement was measured using an LVDT and the signals acquired using a National Instruments USB-6009 data acquisition card. A length of fishing line passed over a pulley connected the actuator to the floating core LVDT. The setup allows the addition and removal of counterweights. The tests here were performed with a load of 5grams. Data were collected in LabVIEW and post-processing was performed using Simulink and MATLAB (Fig. 3.3).

3.4 Modeling

The actuator system was modeled by first determining the electrochemical response of the polymer, and then analyzing the mechanical response.

3.4.1 Electrical System

A widely-accepted circuit model for polypyrrole actuators was originally introduced in [17]. The electrical circuit model was adjusted by including a leakage current and ignoring the double layer capacitance due to its quick charging time [28]. This simplified circuit model for a polypyrrole actuator can also be found by first starting with a more detailed electrical model specifically for polypyrrole-metal coil composite actuators [8]. By neglecting the effects of the quick-charging double layer as well as the inductor, the model can be simplified, eventually arriving at a single loop. If the voltage source is exchanged with a

current source in parallel with a resistance, an equivalent electrical model is achieved.

The simplified circuit model covers the electric domain, and considering the simplification in Fig. 3.4a, the model can incorporate characteristics of the electric connectors and electrolytic solution, as well as a component or a superimposed resistance. The combination of the separate elements in this manner should allow for an easier transition to a more complex model in the future.

3.4.2 Stress-Strain Relationship

The charge build-up in the polymer directly creates a change in displacement by inducing a movement of ions into, or out of, the polypyrrole polymer chain. The proportional relationship between charge density (ρ) and electrochemical strain (ε) is described by the coefficient, α in Eq. 3.1.

$$\varepsilon = \alpha\rho \tag{3.1}$$

Polypyrrole actuators have been shown to have a viscoelastic response [28]. This work utilizes a similar mechanical response model, but includes the mechanical response of the embedded metal helix (Fig. 3.5).

3.4.3 Derivation of State Equations

The combined, simplified model for the actuator system can now be used to determine the state-space system. For this purpose, Bond graph analysis (shown

in Fig. 3.6) was used to formulate the state-space equations shown in Eq. 3.2.

$$\begin{bmatrix}\dot{Q}_c\\ \ddot{x}_1\\ \dot{x}_1\\ \dot{x}_2\end{bmatrix}=\begin{bmatrix}\frac{-1}{(R_1+R_2)C} & 0 & 0 & 0\\ 0 & \frac{-b}{m} & \frac{-k_1}{m} & \frac{-k_2}{m}\\ 0 & 1 & 0 & 0\\ \frac{-\alpha}{\forall}\left(\frac{-1}{(R_1+R_2)C}\right) & 1 & 0 & 0\end{bmatrix}\begin{bmatrix}Q_c\\ \dot{x}_1\\ y\\ x_2\end{bmatrix}+\begin{bmatrix}\frac{R_2}{(R_1+R_2)} & 0\\ 0 & 1\\ 0 & 0\\ \frac{-\alpha}{\forall}\left(\frac{R_2}{R_1+R_2}\right) & 0\end{bmatrix}\begin{bmatrix}I_{in}\\ g\end{bmatrix} \quad (3.2)$$

$$y=\begin{bmatrix}0 & 0 & 1 & 0\end{bmatrix}\begin{bmatrix}Q_c\\ \dot{x}_1\\ x_1\\ x_2\end{bmatrix}+\begin{bmatrix}0 & 0\\ 0 & 0\\ 0 & 0\\ 0 & 0\end{bmatrix}\begin{bmatrix}I_{in}\\ g\end{bmatrix}$$

The state-space form of the actuator system using parameter values from Fig. 3.4 and Fig. 3.5 is shown in Eq. 3.2. For the states, Q_c represents the amount of charge in the volume capacitance in the electrical domain, x_1 is the overall actuator displacement, and its derivative is the actuator velocity. The other displacement value, x_2, represents the polymer elasticity element in the mechanical model. The electrical parameters are shown in Fig. 3.4d. The actuator volume and mass are V and m, respectively, and α is the charge-to-strain coefficient. Aligning with the nomenclature in Fig. 3.5, k_1 is the coil spring constant and polymer elasticity parameter, k_2 is the polymer elasticity element parameter, and b is the coil damping parameter.

3.5 Open-loop Control

Open-loop control of the polymer actuator system allows the parameters of the simplified model to be identified. First the response in the electrical domain is determined, and these values are used in predicting the states that could not be

directly measured. The unmeasured states are then used to determine the parameters of the mechanical system model.

Three different samples were fabricated through identical means. All three samples possessed the same geometry, except for length. The samples are labeled Sample A, Sample B, and Sample C and had lengths of 15 mm, 27 mm, and 12 mm, respectively.

3.5.1 Electrical Parameter Identification

The electrical model parameters are determined first, since both the input current and input voltage can be easily measured, and the electrical system influences the mechanical output but the mechanical system does not influence the electrical system [28].

The electrical system model is used to describe the relationship between the input voltage and current. This relationship can be analyzed at multiple time steps to create an array of data values. A recursive least squares algorithm is applied to solve for the electric system parameters (outlined in [16]). Although it is possible that the electrical system parameters can change over time, the change is expected to be minute over the time period covered by the identification data.

3.5.2 Estimating Unknown States

Referring to the system model, the determined electrical system parameters, along with the known inputs and displacement output, can be used to determine

the unmeasurable states, Q_c and x_2, which represent the charge buildup in the volume capacitance of the polymer, and the displacement of the polymer elasticity element, respectively. The unknown state formulation is in Fig. 3.7.

3.5.3 Mechanical System

The parameters of the mechanical system are determined by a recursive least squares algorithm, similar to the electrical system, with the inclusion of the unmeasurable states. Fig. 3.8 shows the process flow formulation of the mechanical domain recursive least squares algorithm. First, the overall displacement, x_1, and its first and second derivatives are determined, along with the polymer elasticity displacement, x_2, at one moment in time. These data are collected at two additional time steps and then rearranged in the matrix format shown in the bottom of Fig. 3.8 to solve for the unknown mechanical model parameters. These parameters are then fed through low pass filters. Once all of the model parameters have been determined, they can be used in the state-space formulation frequency domain analysis.

3.6 Frequency Domain Analysis

3.6.1 Experimental Frequency Analysis

The frequency response of each growth stage was analyzed by determining the sinusoidal response at each half decade value of sinusoidal current input. An example of the raw data is shown in Fig. 3.9.

The raw data required some smoothing and filtering to condition before

results were taken, but the raw data in Fig. 3.8 illustrate the start of a lag in phase.

The Bode plot response shows negative magnitude values at the lowest frequencies. The open-loop response for Sample A in Fig. 3.10 follows a linear trend with consistent response up to approximately 10^{-2} Hz. The linear trend decreases to a negative slope of 20 dB per decade. At approximately 10^{1} Hz, the response takes another decrease in slope to approximately -40 dB per decade. The phase response shows an initial increase in phase lag just before 10^{-3} Hz with pauses around -90 degrees, and then decreases in value again to -180 degrees at the maximum frequency tested.

Although the lower frequency response shows a slightly lower magnitude response, the general Bode plot response from Sample A is also exhibited by Sample B in Fig. 3.11. Sample C also shows a similar Bode plot magnitude output at the lower frequencies, and two sequential linear slope decreases as the frequency value increases in Fig. 3.12.

The general behavior from the Bode plot points was further explored by fitting a series of straight lines to the points and determining a representative Bode plot curve. The curve fitting process is shown in Fig. 3.13.

Once an appropriate Bode plot curve was fit to the experimental data, the 3 dB offset magnitude and corresponding frequency was determined. The 3 dB cutoff acts as a threshold at which the open-loop performance decreases a noticeable amount. The magnitude value associated with the 3 dB cutoff serves as the relative polymer strength for the respective growth stage. The

corresponding frequency at which the 3 dB cutoff strength is found serves as the relative polymer speed capability for the respective growth stage. The cutoff frequency line creation is shown in Fig. 3.14.

This process of performing Bode plot frequency analysis, determining a fitting Bode curve, and establishing the 3 dB cutoff magnitude and frequency was repeated for each growth stage.

3.6.2 Model Based Frequency Analysis

The identification of all of the model parameters allows a Bode analysis at the end of each actuation cycle. Each Bode analysis is used to determine the 3 dB offset and corresponding phase shift at which the 3 dB offset occurs. These two factors are used to determine the actuator performance at the growth level analyzed. The magnitude offset represents the strength of the polymer, and the cutoff frequency represents the speed output of the polymer actuator. The Bode plot results created from a model based upon the parameters calculated during the open-loop experimental testing are shown below.

The model based Bode plot for Sample A in Fig. 3.15 shows a flat linear response with a negative magnitude value at the lower frequencies. Approximately at a frequency of 10^{-2} Hz the model based response decreases with a slope of -40 dB per decade. The phase response decreases at approximately the same time as the experimental results do, but do not stop until -180 degrees are reached, unlike the experimental data which slow lag at -90 degrees before reaching -180 degrees.

The model based Bode plot response for Sample B in Fig. 3.16 also starts with a flat linear response and decreases with a slope of -40 dB per decade at approximately 10^{-2} Hz. The phase response also decreases at approximately the same frequency as the experimental data, and then straightens out at -180 degrees. The behavior is also shown with the model based Bode plot of Sample C in Fig. 3.17.

The model based Bode plots follow the initial response from the experimental based Bode plots with a flat linear response at a negative magnitude value at the lower frequencies. Both the model and experimental Bode plots decrease in magnitude at around 10^{-2} Hz, but the difference is the amount of decrease. The experimental Bode plots make a slope of -20 dB per decade, but then another decrease at a higher frequency. The model based Bode plots make a slope of -40 dB per decade at the cutoff frequency. The model based Bode plots show an increase in initial magnitude as the number of growth stages increase, and a decrease in cutoff frequency as the number of growth stages increase. This makes sense since an increase in polymer thickness results in a stronger and slower actuator. For example, an increased magnitude value and a decreased cutoff frequency value would represent an actuator that has grown stronger and slower compared to previous tests. This is compared on the basis of a consistent load and input level between actuation tests. A larger 3 dB magnitude value represents an actuator that has displaced the load further, and a larger cutoff frequency, or bandwidth value, represents the output of the actuator is lagging further from the input and is therefore considered to be slower. The difference in

experimental and model data is also mirrored with the phase response as the experimental data show a slight pause in the phase lag value decreasing at -90 degrees before meeting the model data that decreased in phase lag value directly to -180 degrees.

3.6.3 Performance Cost Equation

The speed and magnitude values are combined in the cost equation to produce a cost performance value. The performance cost is determined relative to a weighting value, 'w.' The magnitudes for the open-loop tests were all negative, but initial tests inferred that a regression to a point with no growth would be at approximately -25 dB. Therefore, this was used as the Bode plot magnitude basis. Initial tests also showed that samples could all maintain a 10^{-3} Hz input current without reaching the 3 dB cutoff magnitude. The bandwidth values were then selected as the value multiplied by 1^3. These steps make each magnitude and bandwidth value comparable with more similar orders of magnitude for the performance cost evaluation equation shown in Eq. 3.3.

$$Performance\ Cost = \frac{(w)}{Magnitude} + \frac{(1-w)}{Bandwidth} \tag{3.3}$$

The cost function analysis provides a performance cost value for each growth cycle dependent upon the chosen weighting value. The next step was to compare multiple performance values.

Once three performance values were determined, a parabola was fitted

with number of growth cycles being on the x-axis and the performance values on the y-axis. The minimum of a parabola would have the lowest cost and therefore be the optimal growth amount value per the chosen weighting value. Once the parabola is fitted to the three performance data points, the minimum of the parabola is determined. If the minimum is determined to be at a growth value less than the most recent growth number, then it is determined that no more additional growth would improve performance given the weighting value. If the minimum is determined to be greater than the most recent growth value, then it is determined that additional growth will yield a more optimal actuator performance. If additional growth cycles are employed, the curve optimization is repeated, but only the three most recent performance values and growth cycle numbers are used.

3.7 Results and Discussion

First, the model parameters determined by the recursive least squares algorithms are analyzed, and the performance growth optimization are analyzed.

3.7.1 Parameter Evolutions

The parameter identification algorithms first reach steady-state values with the electrical model, and then these values are used to determine the mechanical system values in a cascade behavior. The electrical domain values generally have clear results, as can be seen in the example below.

This electrical parameter rises from zero to the initial guess of 50 during the

first 5 seconds of operation. This is when the RLS algorithm initiates, and the model parameter value is reached and held since a noticeable change in value is not reached to change the model parameter values. An example is shown in Fig. 3.18. The mechanical domain values were not always quite as clear. This is likely due to the large range in input frequencies tested. The RLS has a specific delay used that is meant to be large enough to capture the behavior and not be greatly subjected to noise, and also short enough to capture discrete changes in behavior. At the lower frequencies tested, the RLS equations can be populated with very similar values providing singularities in the matrix inversions. Such an example is shown in Fig. 3.19. Here, the mechanical system value was taken to be approximately $5x10^6$ and this is where the RLS response returns.

The parameter evolution over the multiple growth cycles is shown in Fig. 3.20. The left column of parameter values in Fig. 3.20 show the electrical system parameters at each growth stage for Sample A. The resistances R_1 and R_2 exhibit a general increase in magnitude as the number of growth stages increases. The volume capacitance, C shows an increase in value for the first couple of stages, and then a slight decrease during growth Stages 4 and 5. The right column of Fig. 3.20 shows the evolution of the mechanical system parameters over multiple growth stages for Sample A. The capacitance values k_1 and k_2, and the damping value b generally increases over all stages as the number of growth stages increases.

The parameter resistance values for Sample B shown in Fig. 3.21 also increase as the number of growth stages increases. The capacitance parameter

takes more of a stepwise approach with slight decreases in value for the third and fifth growth stages. All of the mechanical values for Sample B (shown in the right column in Fig. 3.21) increase until the fifth growth stage. At this stage, k_1 and k_2 slightly decrease while b only slightly increases.

Unlike the previous two samples, Sample C shows an increase in every parameter value as the number of growth stages increases, shown in Fig. 3.22.

The general increasing trends in the parameters are most likely the result of an increase of polymeric material. A thicker polymer would create a higher resistance, and allows for a larger electrical capacitance. The trend in the mechanical system parameters could be due to the fact that operational conditions between growth steps did not fully excite the complete polymer response. Although the evolution of the model parameters could not be predicted, it indicates that, not only is more research required, but, until these polymers are better understood, each growth stage should be treated as a unique actuator.

The parameter evaluation was also performed in a case where the polymer actuator was purposely overoxidized. The polymer had a triangular input current with an amplitude of one amp and a frequency of 12.5×10^{-3} Hz. The results shown in Fig. 3.23 show an initial convergence for R_2, the only electrical system parameter that is not determined with additional arithmetic. It then starts to increase at approximately 40 seconds and then becomes erratic at about 60 seconds. This behavior is shown similarly by R_1 while the results from the capacitance, C, are seen with a closer scale in Fig. 3.24. The capacitance shows

an initial convergence up to 20 seconds, and then an increase up to 50 seconds. The capacitance also shows erratic behavior after 60 seconds, marking the point at which overoxidation has occurred. Further testing with the model evaluation can be used to observe and prevent overoxidation.

3.7.2 Frequency Domain Results

The frequency magnitude plots show the experimental data, the experimental data curve fitting, and the model based data for each growth stage of each sample.

The experimental data curve fitting data from Sample A show an initial magnitude distribution similar to the experimental data; lower frequency magnitudes increase with increasing growth stage and then decrease sooner as frequency increases. All growth stages for Sample A produced a close coupling, so the curves fit to the experimental data almost overlap as the frequency increases, as can be seen in Fig. 3.25. The general experimental data fitting model is similar for Sample B in Fig. 3.26, but the curves are more distinct and less clustered as the frequency values increase.

The general experimental data fitting model for Sample C is similar to Sample A with the curves clustering closer together less distinctly as the frequency values increase. The results from Sample C are shown in Fig. 3.27.

3.7.3 Cutoff Frequency Results

Further analysis of the Bode plots shows the progression of cutoff magnitudes and frequencies. The cutoff magnitudes exhibit the general trend of increasing with additional growth while the frequencies generally decrease with increasing growth cycles. The data from Sample A shown in Fig. 3.28 start with a cutoff magnitude of just above 10 dB and rise approximately 4 dB each growth cycle. The frequency cutoff starts at approximately $6.4x10^{-3}$ Hz and decreases up to $0.4x10^{-3}$ Hz during each growth cycle.

Sample B has an initial cutoff magnitude of approximately 5.1 dB and rises between 0.75 dB and 1.3 dB each growth stage to end up at 8.7 dB. The cutoff frequencies for Sample B start at just above $3.7x10^{-3}$ Hz and decrease between $0.1x10^{-3}$ Hz and $2.5x10^{-3}$ Hz at each growth stage to end up at approximately $3.15x10^{-3}$ Hz.

The cutoff magnitudes for Sample C start at approximately 13 dB and rise between 3 dB and 8 dB during each growth stage. The cutoff frequencies for Sample C start at 13^{-3} Hz and decrease between $0.1x10^{-3}$ and $0.7x10^{-3}$ Hz during each growth stage to end up just below $11.7x10^{-3}$ Hz.

Although all of the samples exhibit different ranges for the cutoff magnitudes and frequencies, the behaviors are all similar. Even though these cutoff values were determined from a fitted Bode plot curve tailored to the experimental data, the qualitative behavior is consistent between samples. Next, the cutoff magnitudes and frequencies from the model parameters are evaluated.

The data from the Sample A model start with a cutoff magnitude of just under

10 dB and rise approximately 3 dB each growth cycle. The frequency cutoff starts at approximately $6.9x10^{-3}$ Hz and decreases between $0.3x10^{-3}$ Hz and $0.5x10^{-3}$ Hz during each growth cycle.

Sample B has an initial cutoff magnitude of approximately 4.6 dB and rises between 0.4 dB and 0.8 dB each growth stage to end up at 7.2 dB. The cutoff frequencies for Sample B start at just above $4x10^{-3}$ Hz and decrease between $0.1x10^{-3}$ Hz and $0.3x10^{-3}$ Hz at each growth stage to end up at approximately $3.3x10^{-3}$ Hz.

The cutoff magnitudes for Sample C start at approximately 12 dB and rise between 3 dB and 8 dB during each growth stage. The cutoff frequencies for Sample C start at $12x10^{-3}$ Hz and decrease between $0.5x10^{-3}$ and $2.0x10^{-3}$ Hz during each growth stage to end up just below $7.5x10^{-3}$ Hz.

The model derived cutoff plots exhibits values that are different from the experimental data, yet the general behaviors are preserved. This conserved trend mirrored between the experimental data and model derived data represents the basis for using the model data to determine and predict polymer behavior between successive growth stages.

3.7.4 Cost Function-Performance Analysis Comparison

3.7.4.1 Cost Function-Performance Analysis Experimental Data

The determined parameter values were next assembled into the state-space model for each growth cycle, and the model used in a Bode analysis. The performance costs were determined and plotted for the first three growth cycles

using a predetermined weighting value of 0.5, which favors strength and speed equally.

Once three performance cost values were determined, the quadratic curve fitting algorithm was used to determine a quadratic curve to predict the polymer actuator performance over additional growth cycles so the minimum cost could be determined. The quadratic curve fitting shows a minimum value, or most optimal growth value. The minimum is shown with an upside down triangle in the plot below. The entire process is shown in Fig. 3.29.

First, the performance cost values are determined using the performance cost equation and predetermined weighting value. Real-time examples will perform the analysis one growth stage at a time, but for initial evaluations, multiple growth stages were performed to verify results. In this first example, 5 growth stages were performed. The example with five different cost values is shown in Fig. 3.29.

The cost performance algorithm is only initially concerned with the first three growth stages. The first three growth stages are used to determine a best fit parabolic curve. Next, the minimum of the fit parabola is determined and represents not only the minimum of the parabola, but a minimum performance cost in the growth stage behavior and therefore the most optimal amount of growth for the predetermined weighting value. The example in Fig. 3.30 shows a minimum performance cost at a growth number of 2.43.

The actual implementation of this algorithm would instruct the operator to stop growth since the optimal amount of growth was already surpassed. For the sake

of verifying the example, though, the next growth stage was analyzed.

With four different performance values available, the cost performance algorithm is still only concerned with the three most recent values. These three values are used to determine a best fit parabola, and again, the minimum of this parabola is determined. In this example, the minimum of the parabola created by cost performance values from Stages 2 through 4 was calculated to be 2.3 and can be seen in Fig. 3.31.

This test confirms that the optimal amount of growth has been surpassed, and two different trials reiterate that the optimal amount of growth would be at approximately 2.4 on the growth scale. This example was taken from an actual series of sample tests, and although it helped to explain the use of the cost performance algorithm, it also shows that the size of growth steps was so large that optimal stages of growth could be surpassed before the first three growth steps were achieved to allow proper use of the algorithm. This group of samples motivated a smaller growth period for subsequent tests and results from the revised growth procedure are shown in Fig. 3.31.

The cost evaluation algorithm results are first shown for Sample A in Fig. 3.32. The curve fitted parabolas are shown with dotted lines, and the minimums of the fitted curves are displayed with inverted triangles. All three performance minimums for Sample A are grouped around the fourth growth stage.

The performance cost analysis for Sample B in Fig. 3.33 shows an initial optimal growth at growth Stage 5. Both additional growth stage performance tests show optimal growth at the fourth growth stage.

Sample C shows a different optimal growth evolution in Fig. 3.34. The first and second optimal growth amounts are around 12 and 6, respectively (not pictured in Fig 3.34). The third optimal growth analysis shows an optimal growth at just less than five growth stages. Next, the same performance cost analysis was performed with the model parameters.

3.7.4.2 Cost Function-Performance Analysis Model Data

The optimal growth analysis for Sample A shows the optimal growths grouped around three as a growth stage value in Fig. 3.35.

The optimal growth values from the performance cost analysis of the Sample B model data are grouped between four and five on the growth stage axis in Fig. 3.36.

The cost performance analysis for the model data of Sample C has a large initial, optimal performance cost value at almost eight (not pictured in Fig. 3.37), and then the additional optimal growth analyses are between three and a half and four on the growth axis.

Next, the cost performance was compared between the experimental and model data sets.

3.7.4.3 Cost Function-Performance Analysis All Data

The experimental and model data for Sample A both provide an initial optimal growth value between three and four growth stages, but the experimental data are much closer to four while the model data are much closer to three.

Performance cost values for Sample A are shown in Table 3.1. Using just the model data as a guide would instruct no additional growth at this stage while the experimental data would encourage one more growth stage. Either way, an additional growth stage was performed during this experiment. The second optimal growth value (which uses growth stage information from growth Stages 2, 3, and 4) is approximately 3.7 from both the experimental and model data sets.

This optimal growth point would be calculated after the fourth growth stage and would therefore instruct no more additional growth for the actuator. Nonetheless, an additional growth stage was performed and the resulting optimal growth stage is determined to be just above four for the experimental data and just below three for the model data. Although, optimal growth is reached after just one additional growth stage beyond the three stages needed to start the cost values and model data determined optimal growth values are consistently less than one growth stage in difference.

The experimental and model data for Sample B both present an optimal growth amount between four and five with the experimental data value being closer to five and the model data value closer to four. Both model sets therefore recommend additional growth beyond the third growth stage. The second optimal growth value determined from the experimental data determines that the additional amount of growth is reached at the fourth growth stage. This is reiterated by the third optimal growth value determined by the experimental data set for Sample B.

The second optimal growth value determined by the model data set is closer

to five and could encourage additional growth from Stage 4 to Stage 5. The third optimal growth value is then determined to be four on the growth stage. Again, the optimal growth values are different between the experimental and model data sets, but they are consistently less than one full growth stage between the experimental and model data for Sample B.

The initial optimal growth stage from both data sets for Sample C recommend multiple growth steps needed to reach the optimal amount of growth. The second optimal growth value determined by the experimental data set instructs an additional stage to five, and then the third optimal growth stage reiterates that that stage has been achieved. Both the second and third optimal growth values determined by the model values are slightly above 3.5. Sample C shows a large difference in optimal growth values between the experimental data set and model data set. Following the cost performance analysis using the experimental data would have an optimal actuator at five growth stages, and following the model data would create an optimal actuator at four growth stages. This means the optimal growth values from each data set are different by multiple growth stages, but the final amount of growth using each formulation would produce actuators separated by one stage of growth.

All of the previous analyses were performed at a weighting value of 0.5 which equally favors the speed and strength values. Additional analyses were performed using different weighting values. Decreasing the weighting value from 0.5 to 0.3 shows a desired increase in optimal growth for Sample A. The third optimal growth value from the experimental data would recommend an additional

growth stage to six, and the third optimal growth value from the model data would reiterate that five is the optimal amount of growth stages. The end stages of growth are different between the experimental and model data, but both are greater than the desired optimal amount of growth using a weighting value of 0.5.The difference in weighting value for Sample A is shown in Table 3.2.

Decreasing the weighting value again shows an increase in desirable amount of growth stages. The analysis for Sample A with a weighting value of 0.1 is shown in Table 3.2 where the first, second, and third optimal growth values would instruct an additional growth stage.

Next, the weighting value was increased above 0.5. Increasing the weighting value favors fewer growth cycles, as can be viewed by the second and third optimal growth values for both the experimental and model data with Sample A. The anomaly is the first optimal growth value for the experimental data, which would instruct additional growth. In this case the model based optimal growth values are more consistent and conservative than the experimental based optimal growth values.

The general behavior of decreasing the weighting value and obtaining higher amounts of desired growth, and increasing the weighting value to obtain lower amounts of desired growth is shown below for Sample B in Table 3.3.

Decreasing the weighting value to 0.3 shows the desired optimal growth values to be six and five for the experimental and model data, respectively. Increasing the weighting value to 0.7 describes an actuator that has already reached its optimal amount of growth by the third growth stage according to both the

experimental and model data.

A larger weighting value, which greatly favors speed over strength, presents an optimal growth between the initial growth and the first additional growth stages. The increase in weighting value, which specifies a faster actuator response over actuator strength, favors less growth. This is consistent with the parameter evolution information that shows that increasing growth generally increases both capacitance and resistance. The increase in capacitance allows for more charge storage and ion storage, and therefore a higher force output, but the increase in resistance and material would slow ion and charge transport to achieve the maximal force output. The larger force output therefore requires more material and more growth. A lower weighting value should be selected to favor strength over speed.

3.8 Conclusion

The ability of polypyrrole-metal coil composite actuators to regrow during their lifetime of operation necessitates a means by which to judge and compare performance. This work first looks to better understand how the actuators evolve during multiple growth cycles by analyzing experimental Bode plots and using a simplified model and determining the model parameters at each growth stage. These experimental and model parameters are used in a frequency analysis and a performance cost value determined using a specific performance weighting value. These performance cost values were compared as the number of growth stages was increased between the experimental and model data. The model

data with parameters determined during operation acts as an accurate optimal growth stage predictor.

This work will be extended by first implementing shorter growth times in an attempt to not surpass the optimal growth level before the optimization algorithm can be employed, and then, additional growth times based upon the performance prediction curves. Also, the parameter determination algorithms will be used to create closed-loop controllers for these nonlinear, polymeric actuators exercising multiple growth stages.

3.9 Acknowledgements

The authors would like to thank Dr. Debra Mascaro and Dr. Kent Udell for use of their facilities and lab space.

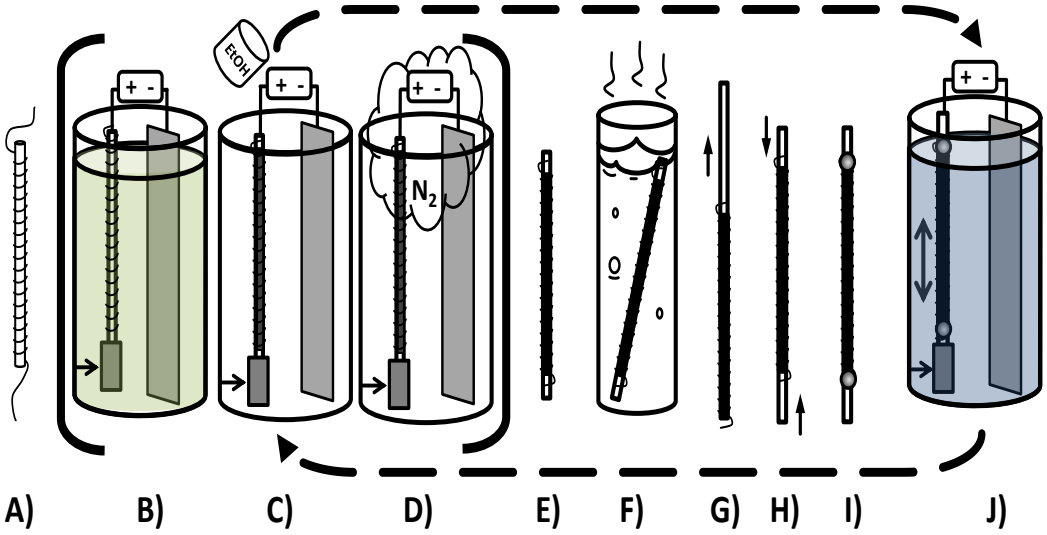

Figure 3.1. The polypyrrole-metal coil composite synthesis process is illustrated. The smaller tungsten wire is wrapped in a helix around the nitinol core material in A). Polypyrrole is synthesized on the tungsten/nitinol combination working electrode in B) when placed in the growth solution. After a 2 minute growth step, the polypyrrole is rinsed with ethanol (EtOH) in C) and dried in nitrogen (N2) gas in D). Steps B), C), and D) are repeated in succession eight times. Then the polypyrrole-coated tungsten/nitinol working electrode is removed from the cell in E) and placed in boiling distilled water in F). This contracts the nitinol core to allow for easier removal in G) while still leaving the tungsten helix embedded in the polypyrrole. Small core pieces are reinserted in the tips of the actuator in H) and affixed with silicon adhesive in I). At this point the initial synthesis of the actuator is complete and can be placed back in the cell with actuation solution, in J). Additional growth steps involve repeating steps B), C), and D) before returning to step J).

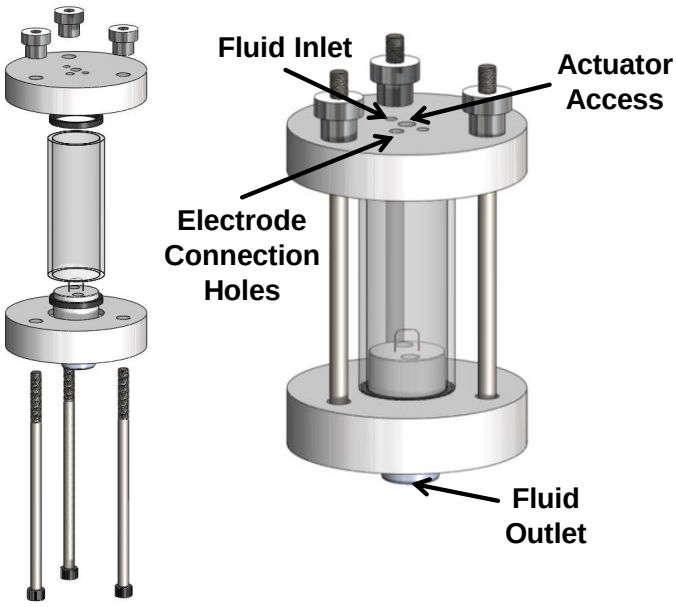

Figure 3.2. The custom test cell is displayed with two Delrin pucks sealing a glass tube chamber and held by three bolts and thumb screws (adapted from [16]).

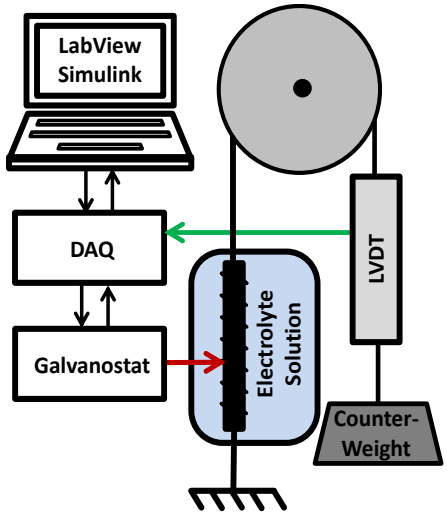

Figure 3.3. The experimental setup for testing polymer actuator displacement, and control and analysis with a power source (Galvanostat), data acquisition card (DAQ), and laptop with the specified software installed

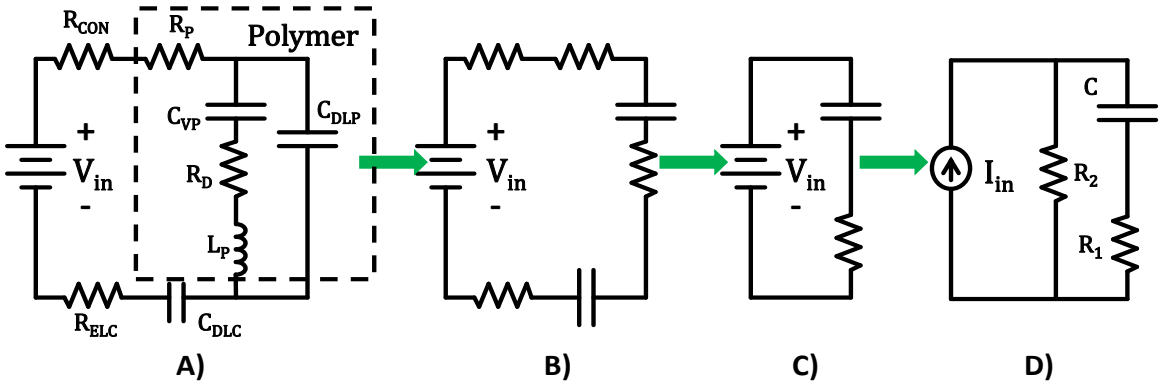

Figure 3.4. Electrical system model. A) shows the circuit model for a polymer metal-coil composite actuator, where RCON is the contact resistance between the wire helix and the polymer, RP is the polymer bulk resistance, CVP is the bulk volumetric capacitance of the polymer, RD is the diffusion resistance, LP is the inductance of the polymer metal-coil system, CDLP is the double layer capacitance at the polymer and electrolyte boundary, CDLC is the double layer capacitance at the counter electrode and electrolyte boundary, and RELC is the electrolyte resistance model reduction. The inductance and double layer capacitance, CDLP, are neglected to get the circuit model in B). The series combinations are made to get the simplification in C), and the voltage source is replaced with a current source and resistance to get the simplified circuit in D) (modified from [21]).

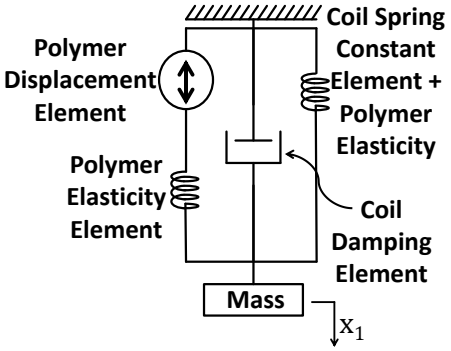

Figure 3.5. Model shown for the mechanical system including the polymer response and the embedded metal helix influence [16]. The state x_1 is shown as the overall displacement. The state x_2 represents the change in displacement of the polymer elasticity element.

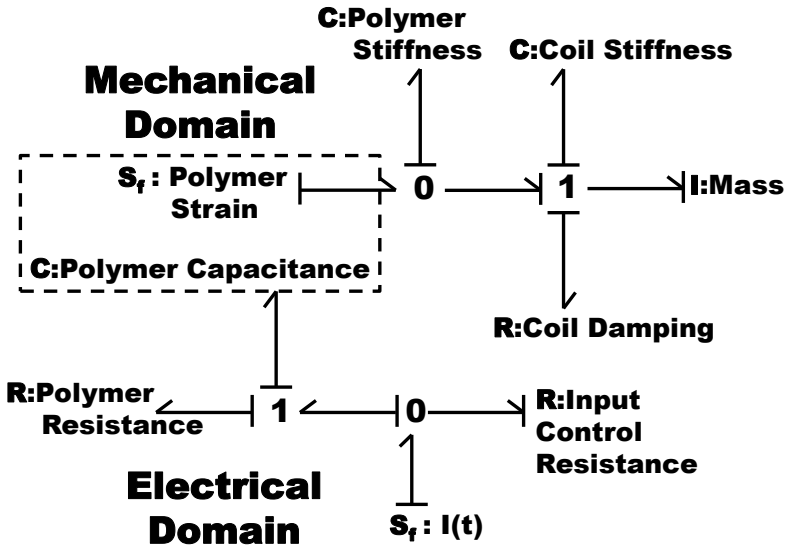

Figure 3.6. Bond graph for polymer model. The dashed line represents the connection between the mechanical and electrical domains.

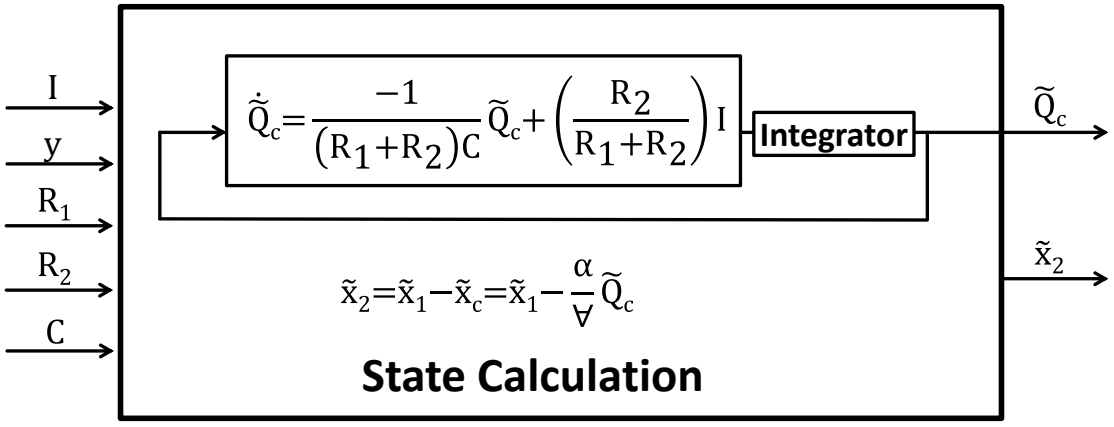

Figure 3.7. Unknown state estimation algorithm is shown. V is the polymer volume.

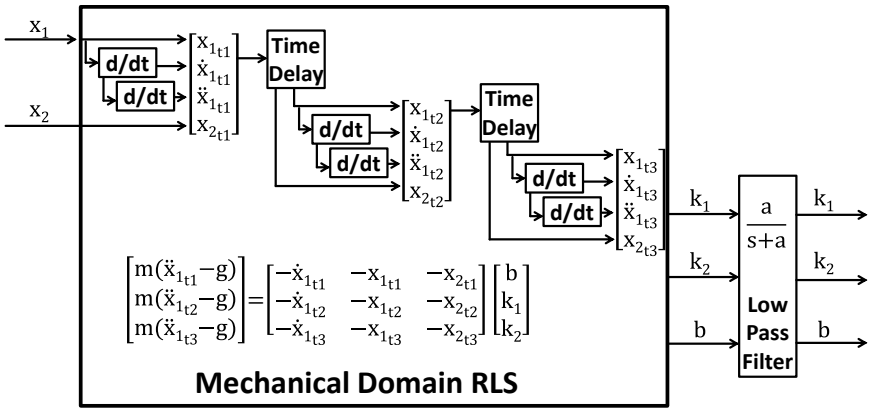

Figure 3.8. The mechanical system recursive least squares algorithm.

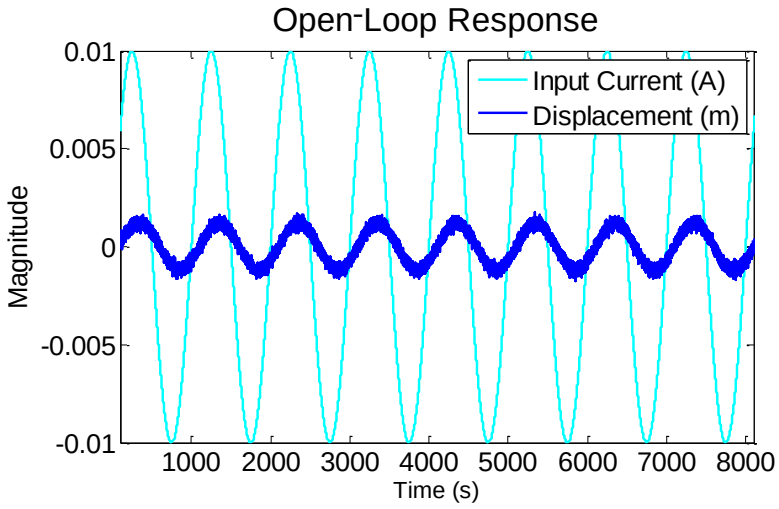

Figure 3.9. Raw data from a frequency test. The current input is shown in teal, and the resulting output is shown in dark blue.

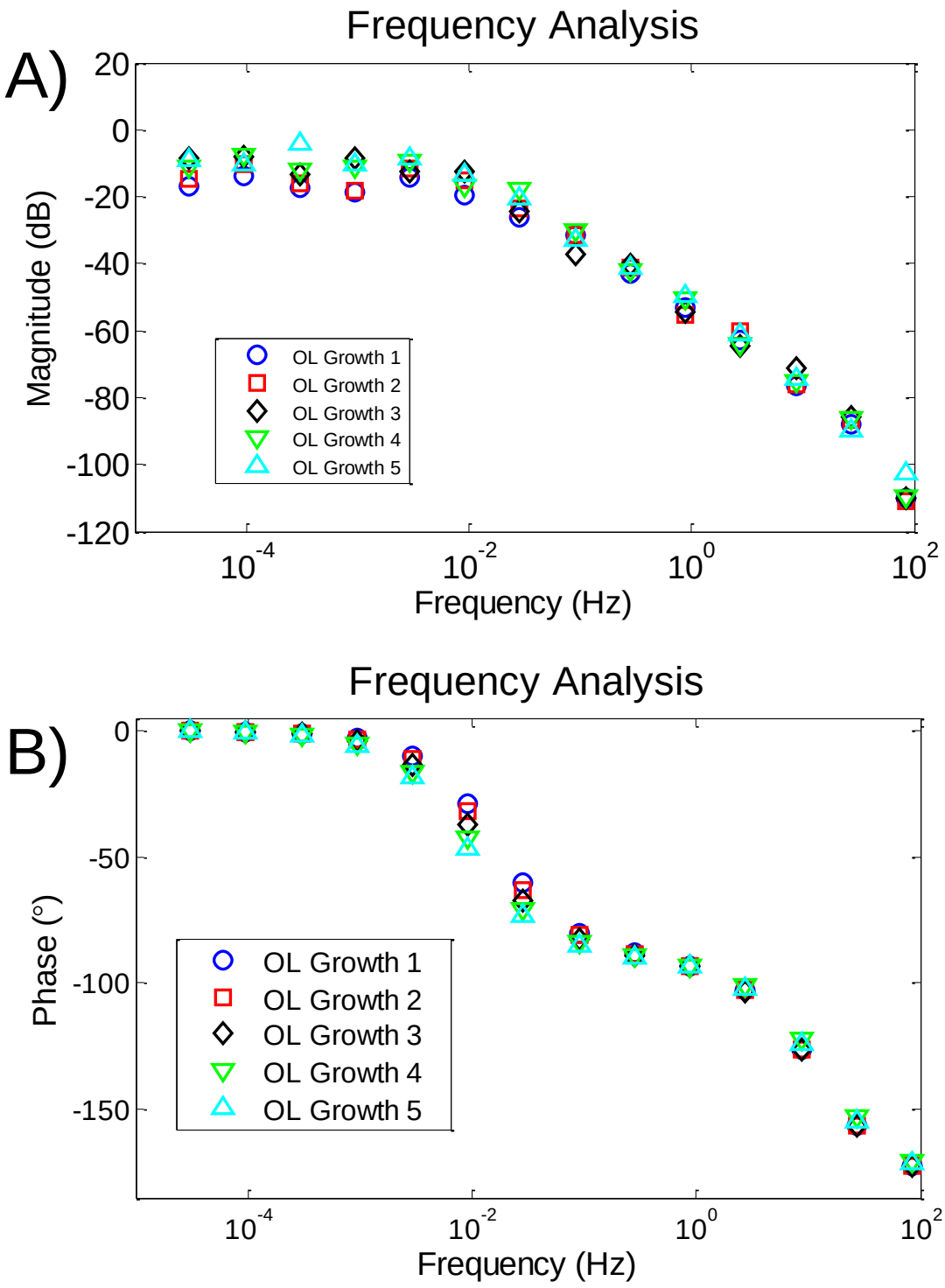

Figure 3.10. Experimental testing Bode plot points for Sample A. The top plot, A), shows the magnitude response from the Bode analysis while the bottom plot, B), shows the phase response for the Bode analysis.

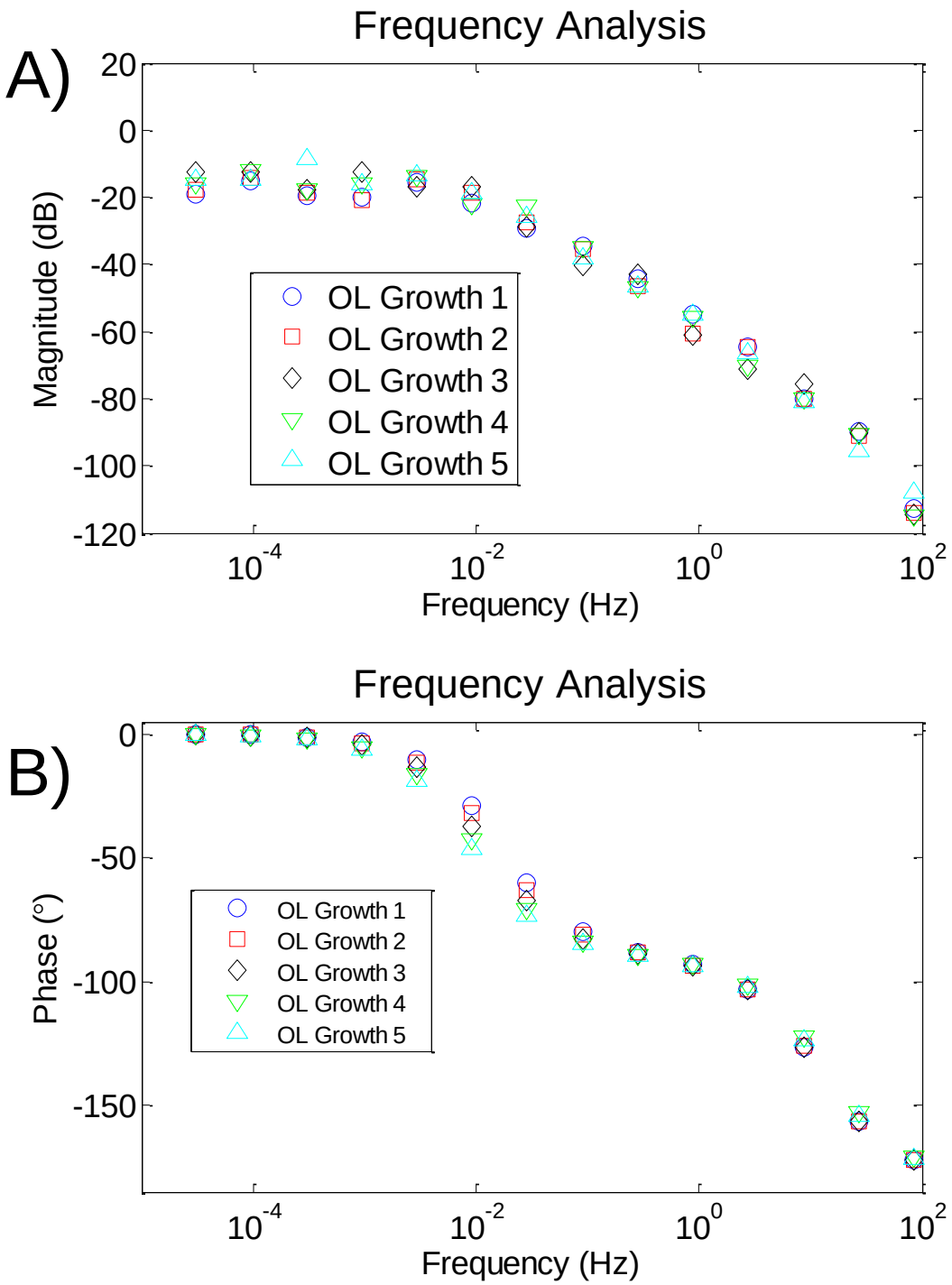

Figure 3.11. Experimental testing Bode plot points for Sample B. The top plot, A), shows the magnitude response from the Bode analysis while the bottom plot, B), shows the phase response for the Bode analysis.

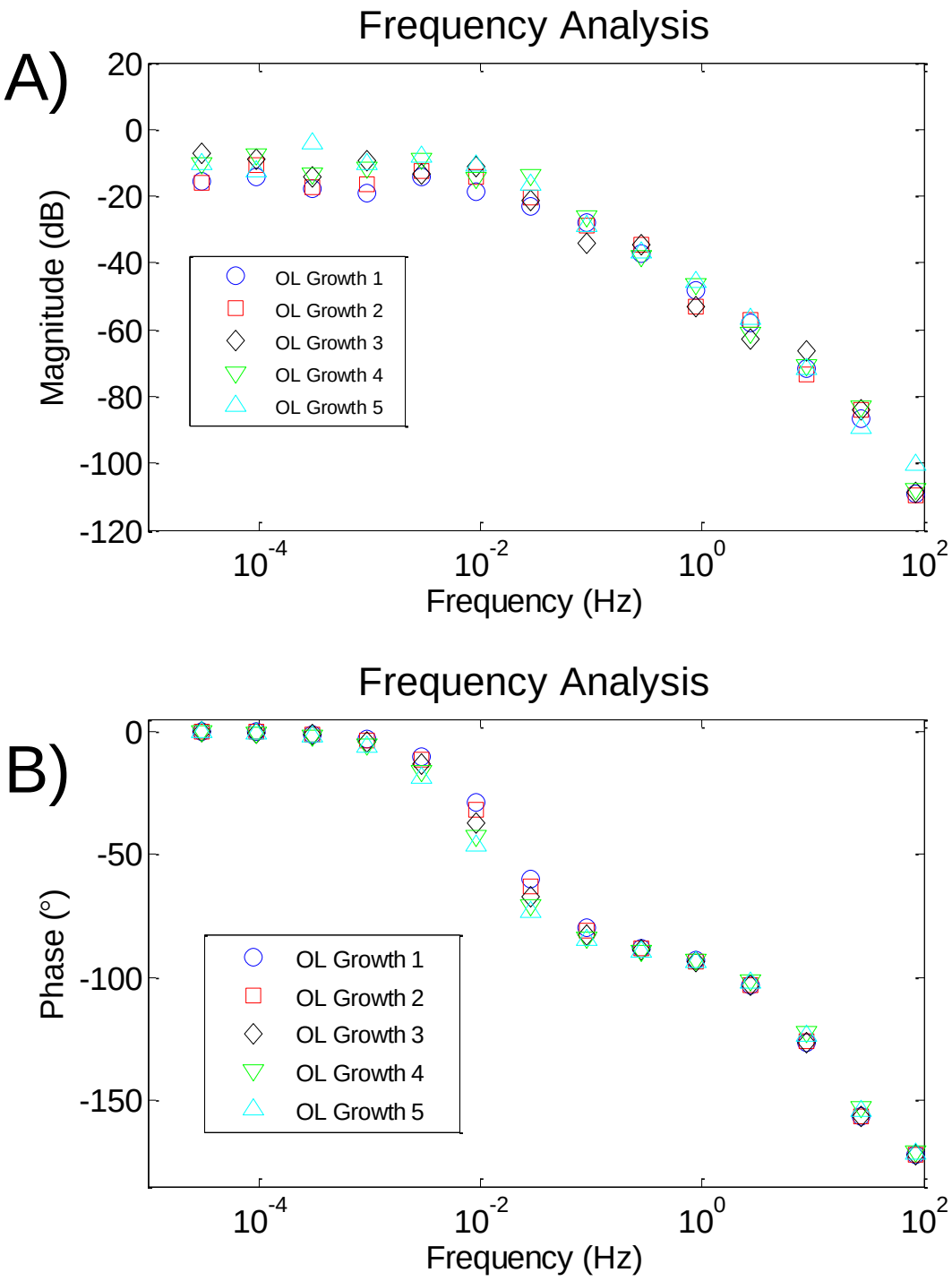

Figure 3.12. Experimental testing Bode plot points for Sample C. The top plot, A), shows the magnitude response from the Bode analysis while the bottom plot, B), shows the phase response for the Bode analysis.

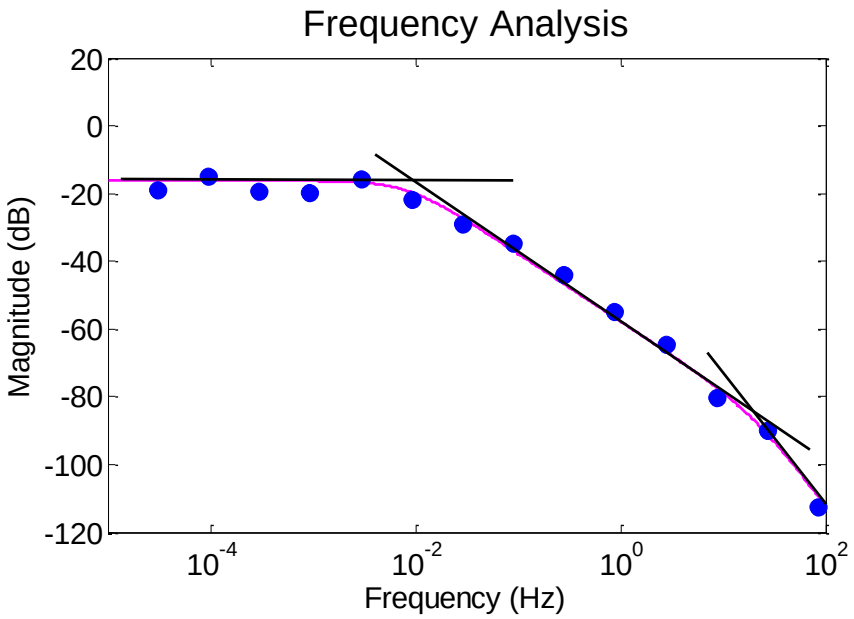

Figure 3.13. Magnitude Bode plot model fitting example using straight line segments to fit the data. The resulting curve fit is shown as a violet line.

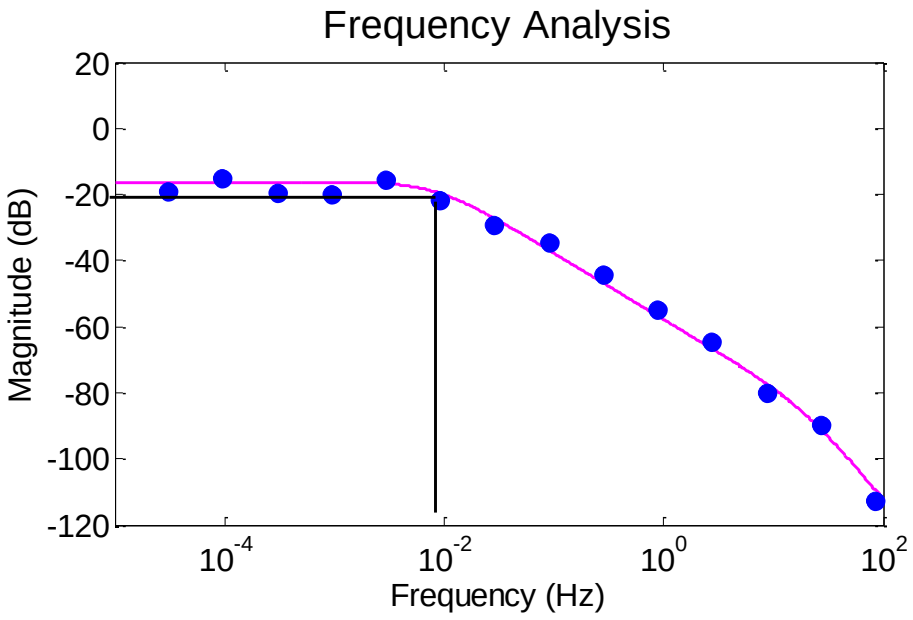

Figure 3.14. Bode plot 3 dB magnitude cutoff frequency and magnitude formulation. The magnitude is the value that is 3 dB below the initial values, and the cutoff frequency is the frequency at which the 3 dB cutoff magnitude is reached.

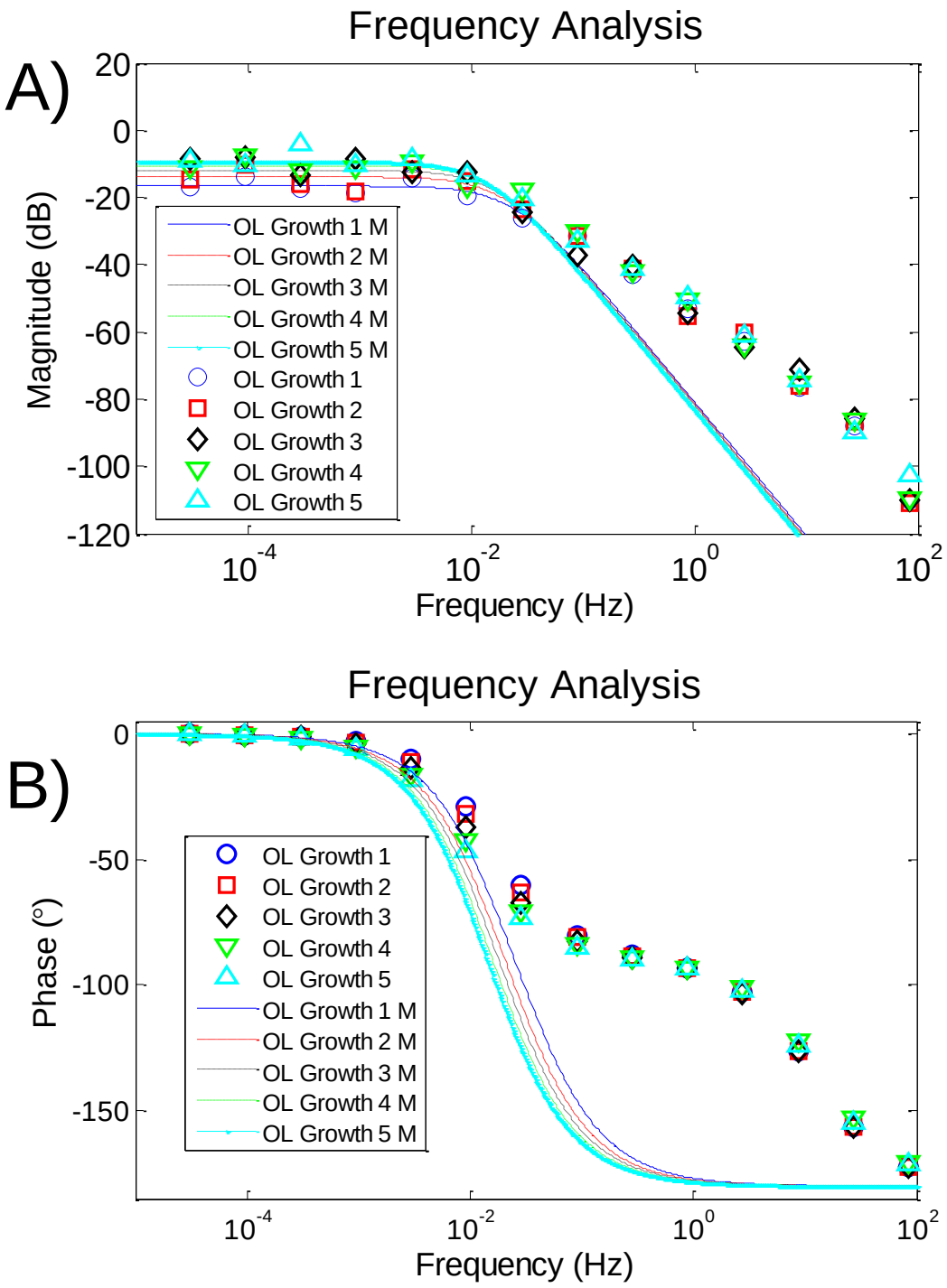

Figure 3.15. Model parameter based Bode plot curve fit for each growth stage with Sample A. The top plot, A), shows the magnitude response from the Bode analysis while the bottom plot, B), shows the phase response for the Bode analysis.

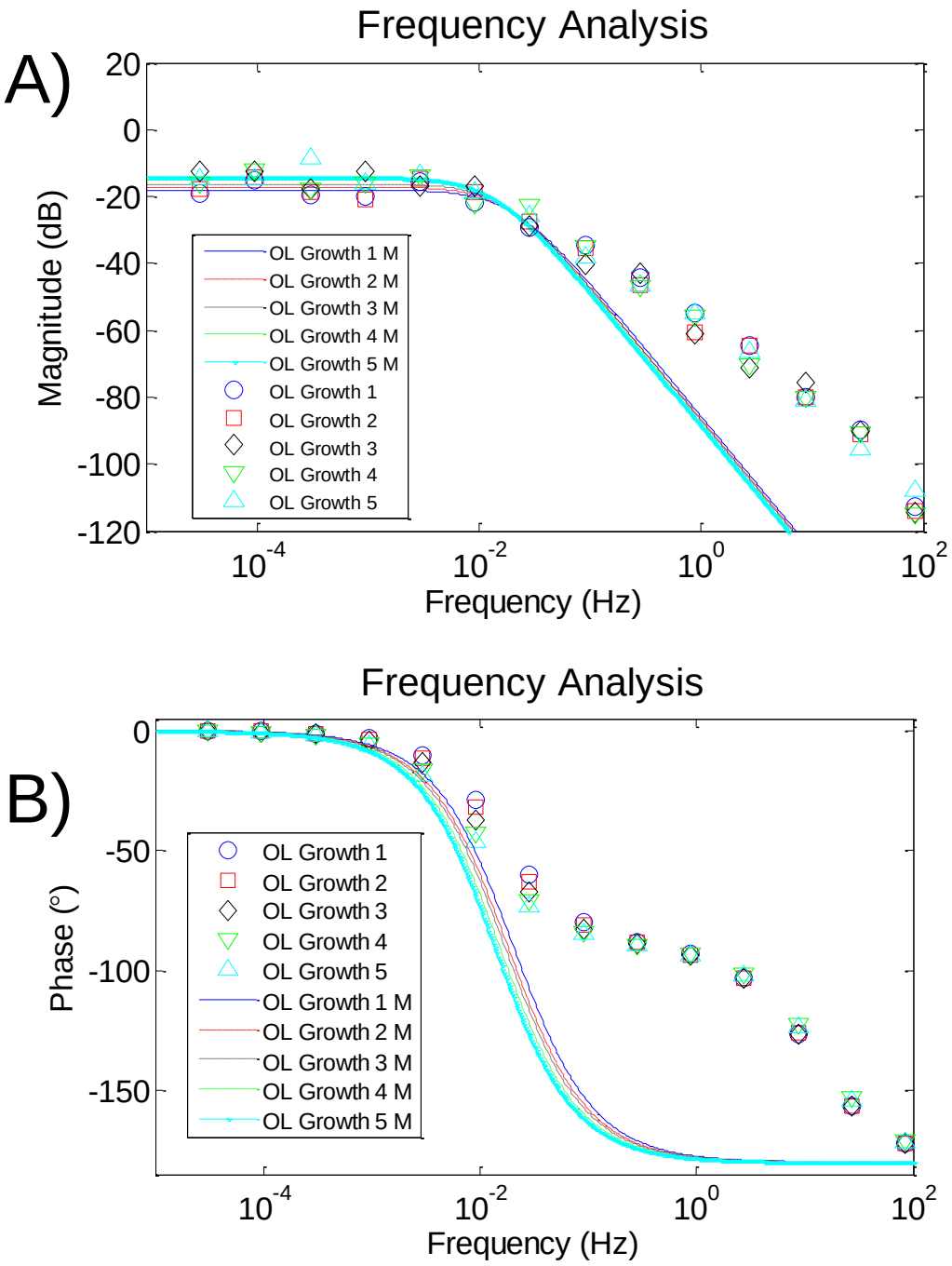

Figure 3.16. Model parameter based Bode plot curve fit for each growth stage with Sample B. The top plot, A), shows the magnitude response from the Bode analysis while the bottom plot, B), shows the phase response for the Bode analysis.

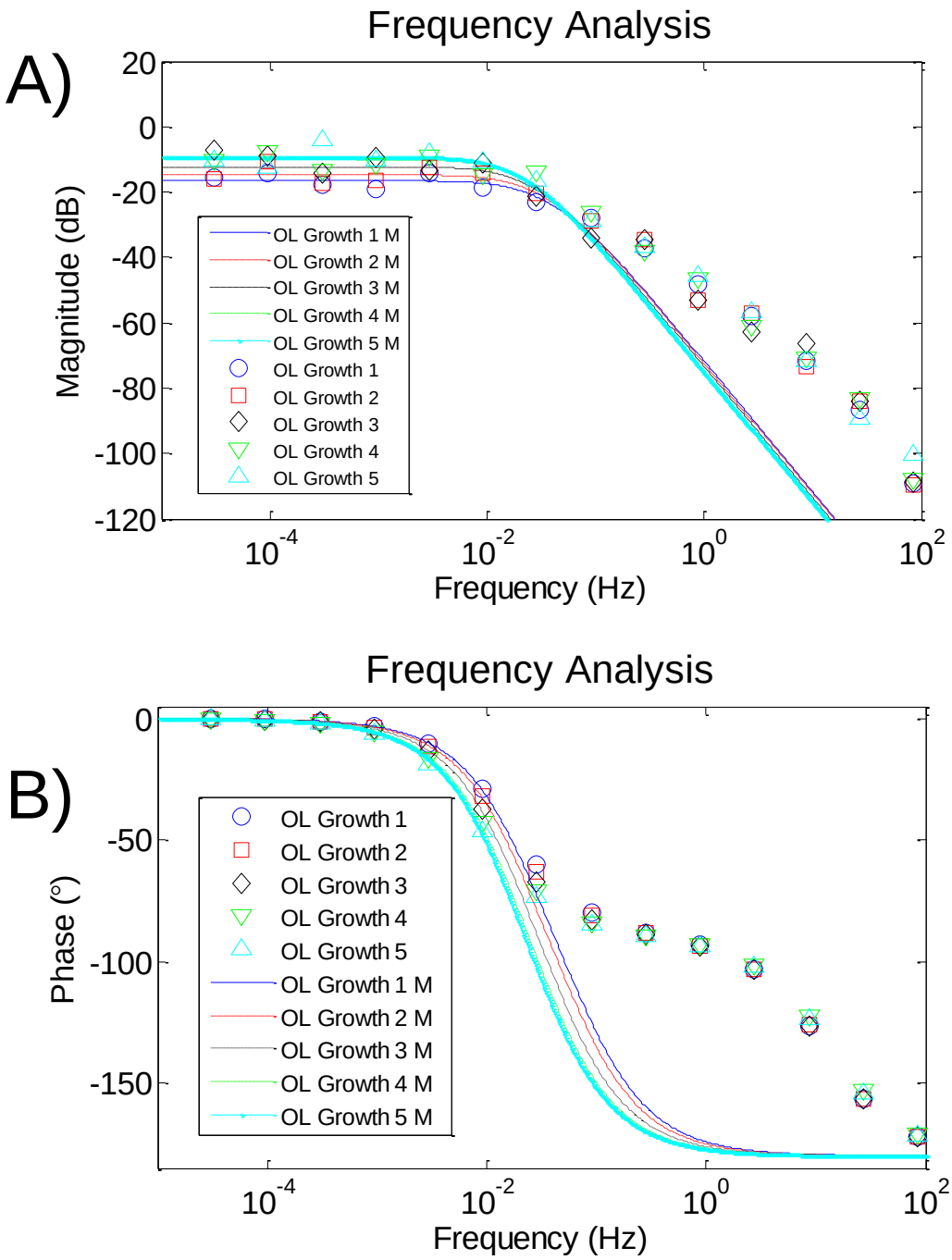

Figure 3.17. Model parameter based Bode plot curve fit for each growth stage with Sample C. The top plot, A), shows the magnitude response from the Bode analysis while the bottom plot, B), shows the phase response for the Bode analysis.

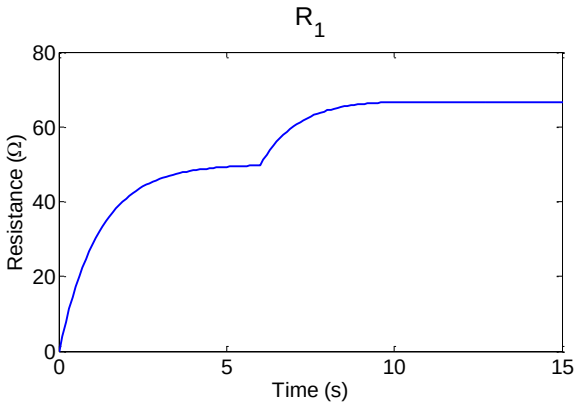

Figure 3.18. Model parameter evaluation for an electrical system parameter.

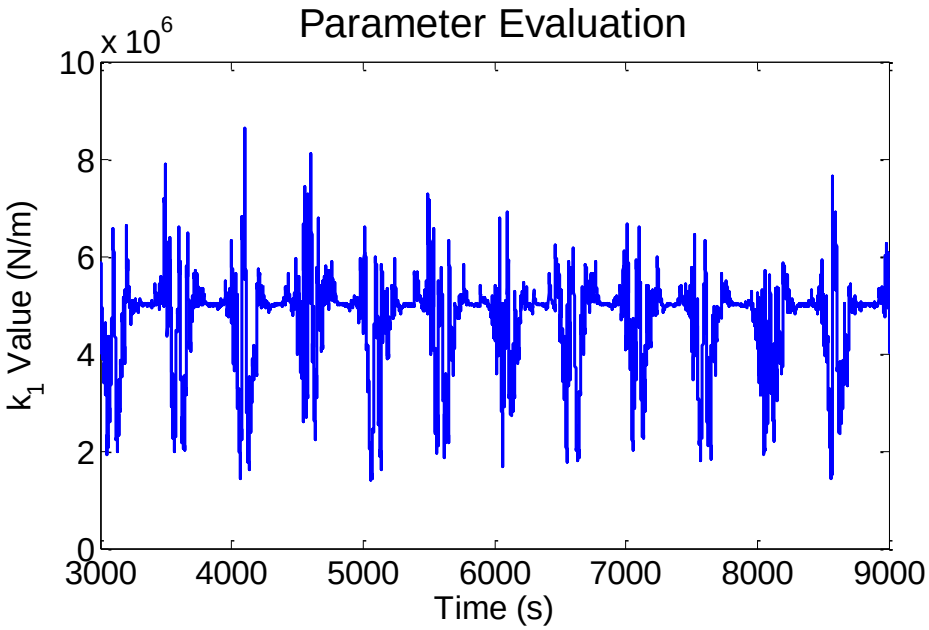

Figure 3.19. Model parameter evaluation for a mechanical system parameter.

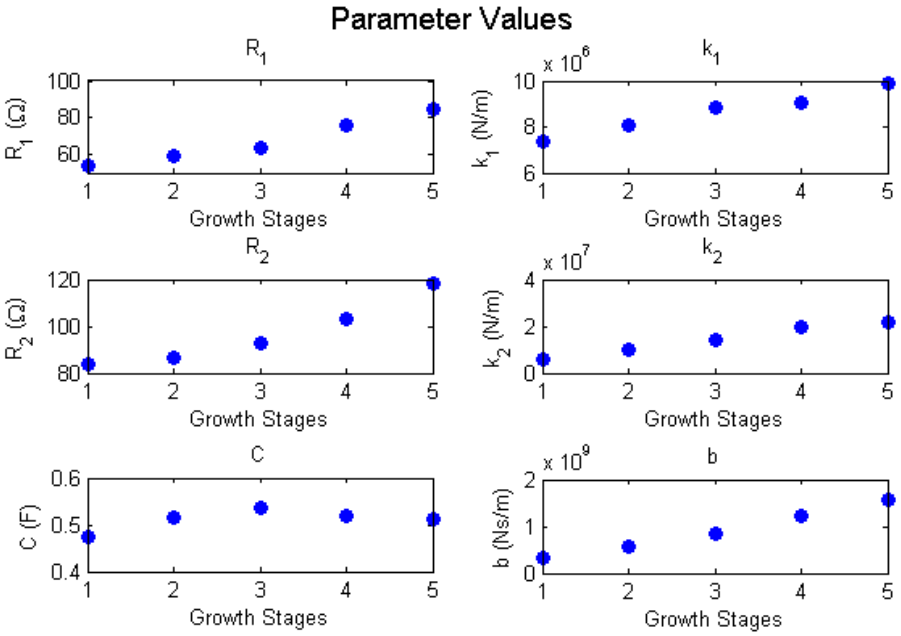

Figure 3.20. Model parameter evolution over multiple growth cycles for Sample A.

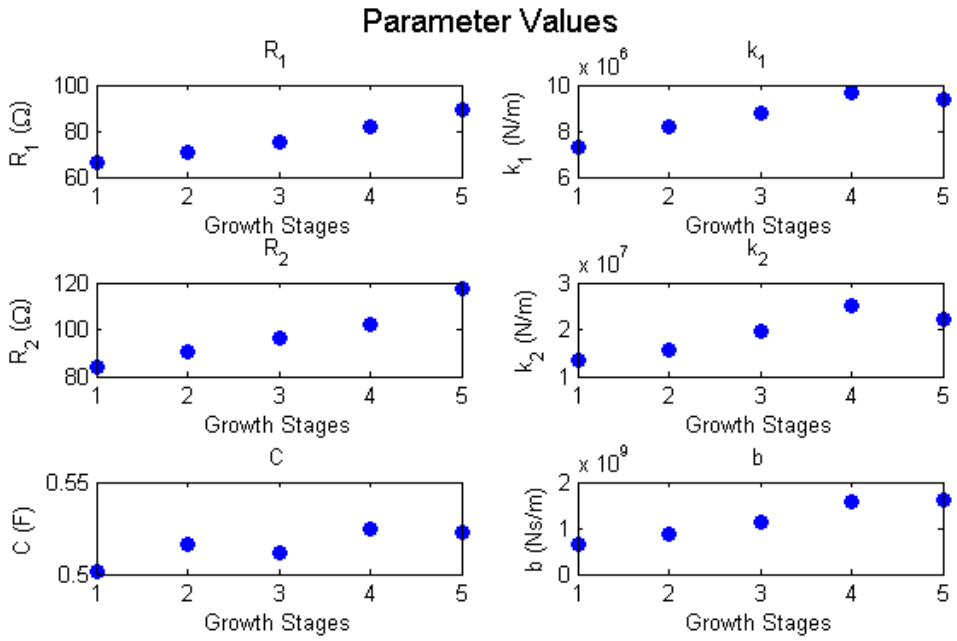

Figure 3.21. Model parameter evolution over multiple growth cycles for Sample B.

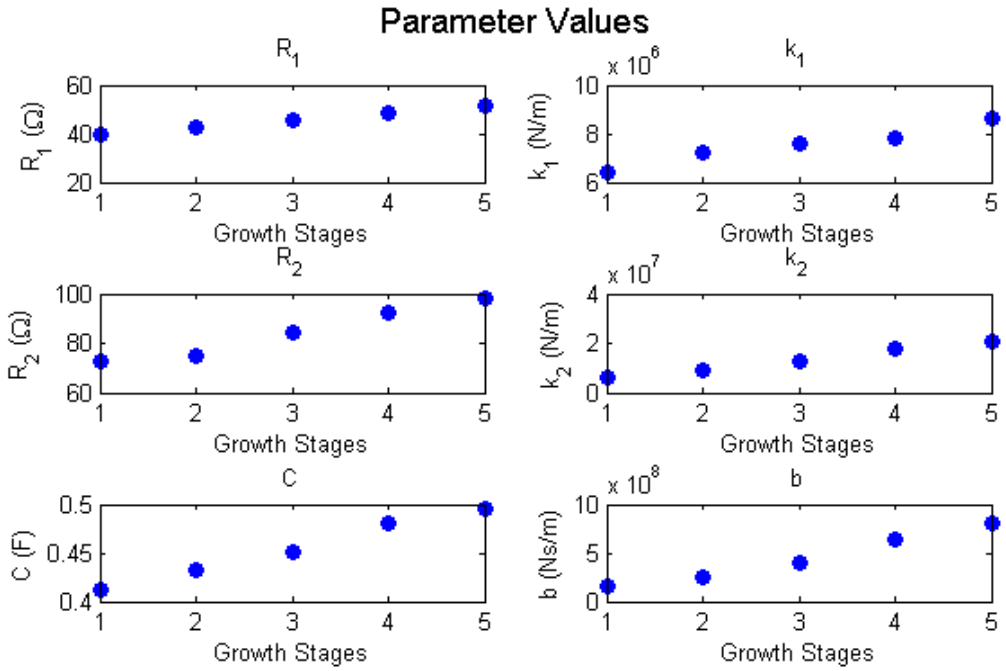

Figure 3.22. Model parameter evolution over multiple growth cycles for Sample C.

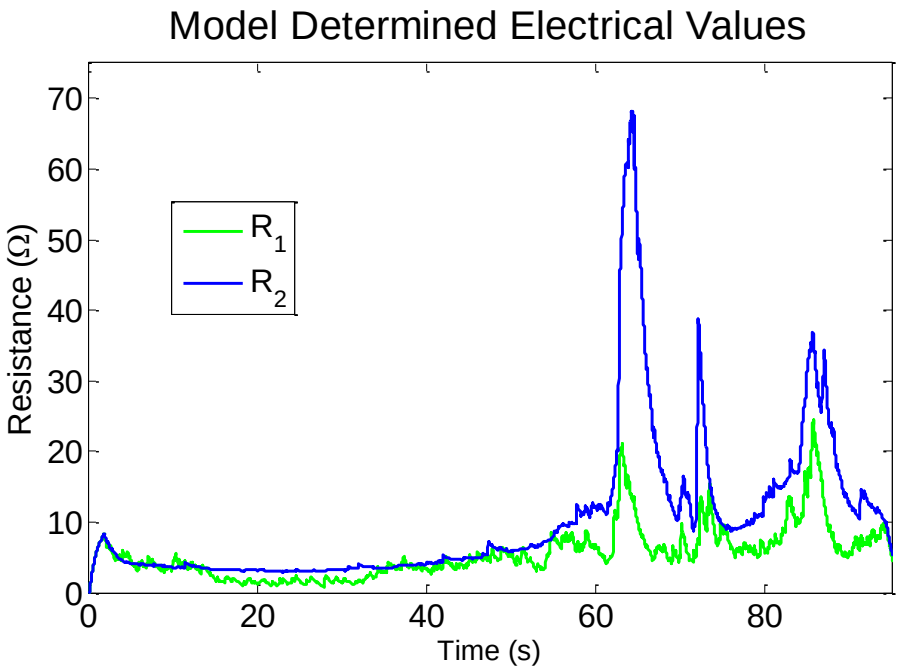

Figure 3.23. Electrical system resistance value results from a purposefully overoxidizing experiment.

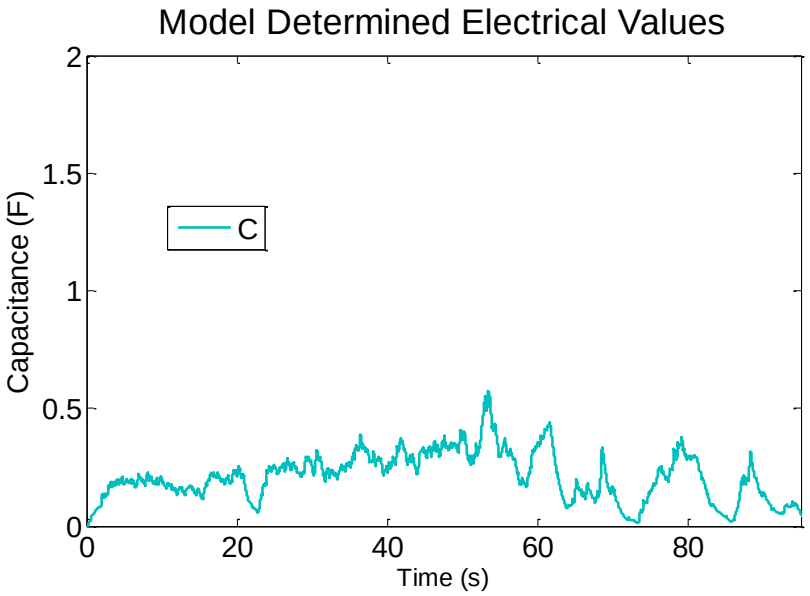

Figure 3.24. A close up of the electrical system results from a purposefully overoxidizing experiment to show the capacitance value results.

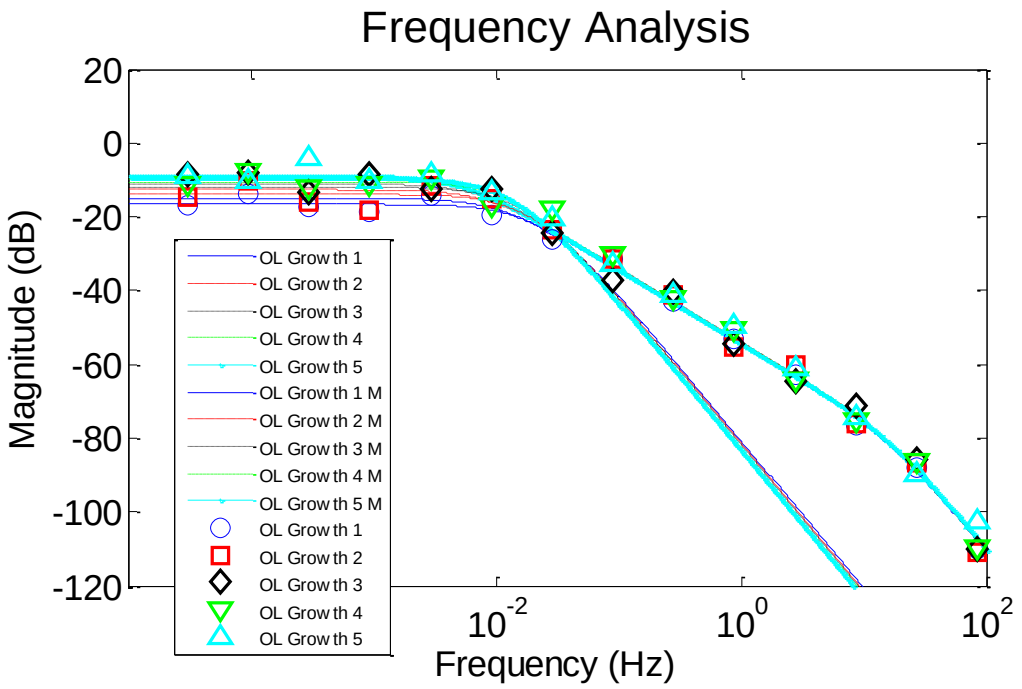

Figure 3.25. Bode plot magnitude results for open-loop control of Sample A.

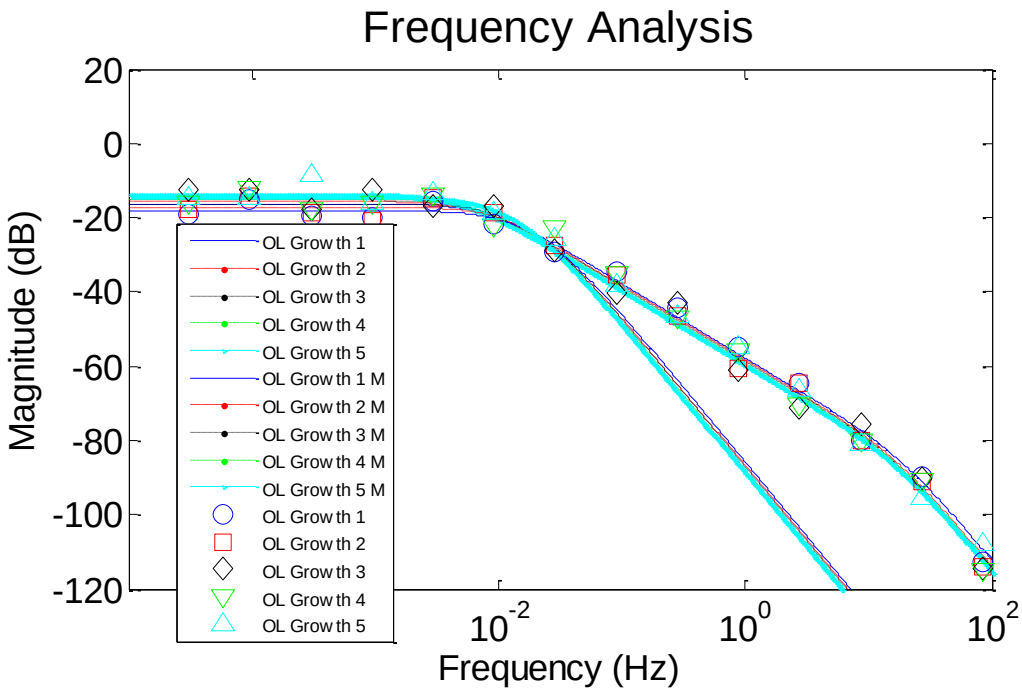

Figure 3.26. Bode plot magnitude results for open-loop control of Sample B.

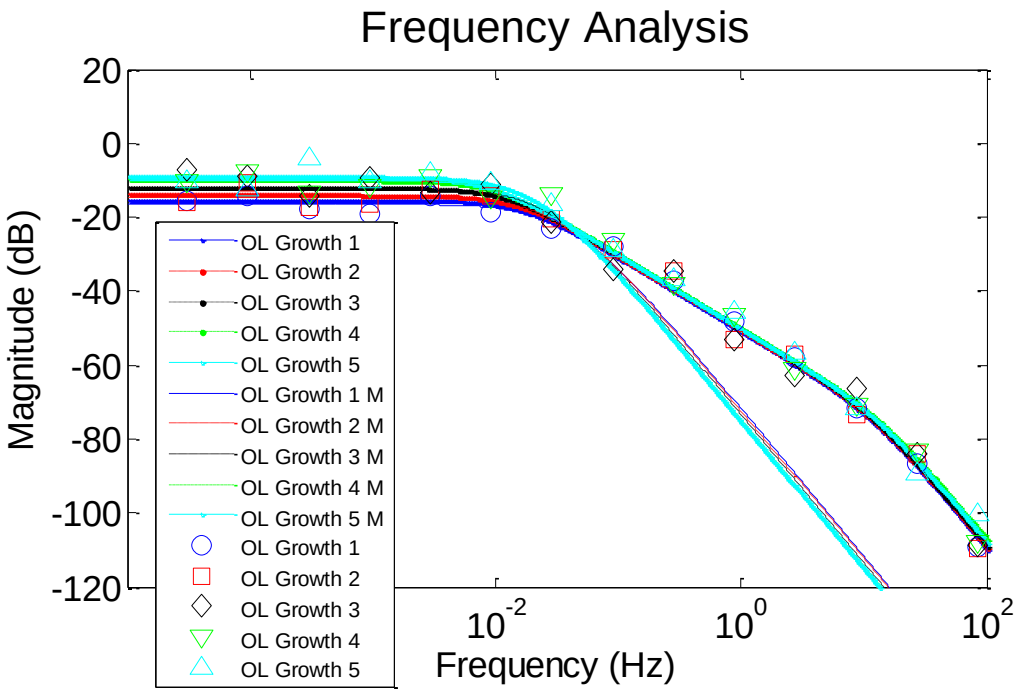

Figure 3.27. Bode plot magnitude results for open-loop control of Sample C.

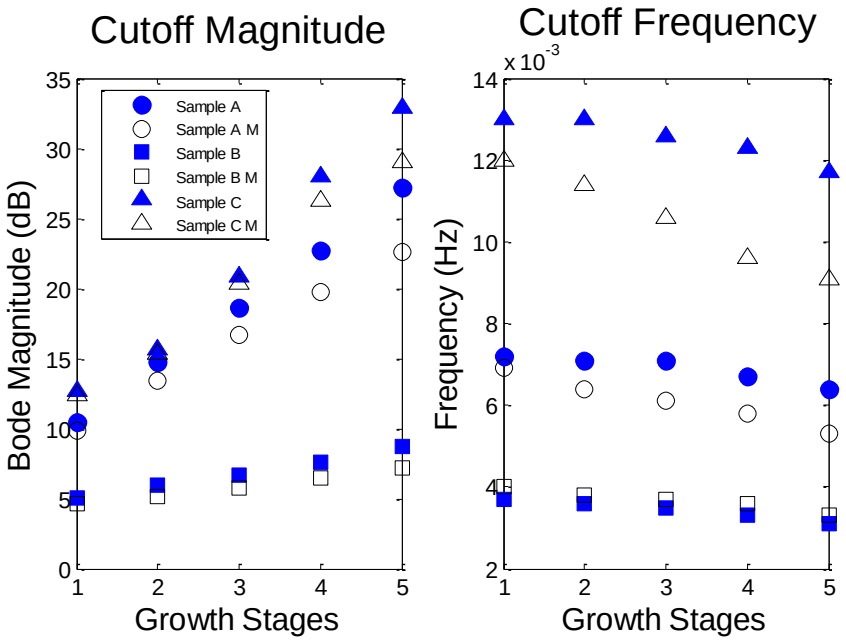

Figure 3.28. The resulting cutoff magnitudes and frequencies from the frequency analyses for each growth stage of each sample experimental and model data (denoted with the 'M').

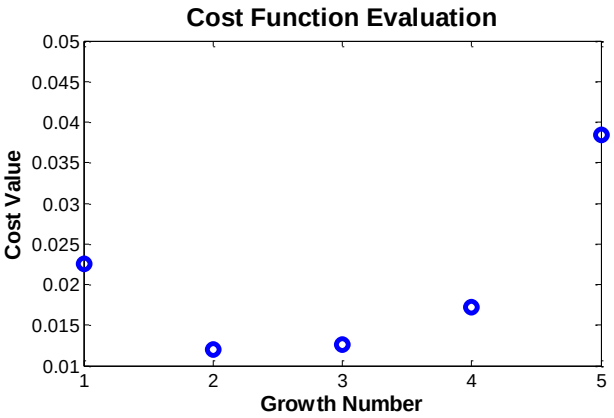

Figure 3.29. Performance cost function evaluation example using five performance values.

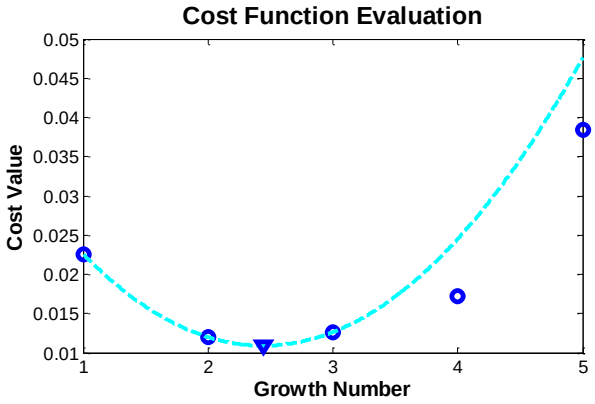

Figure 3.30. Performance cost function evaluation example. The minimum of the curve is determined for the quadratic curve fitted for the three most recent performance cost values.

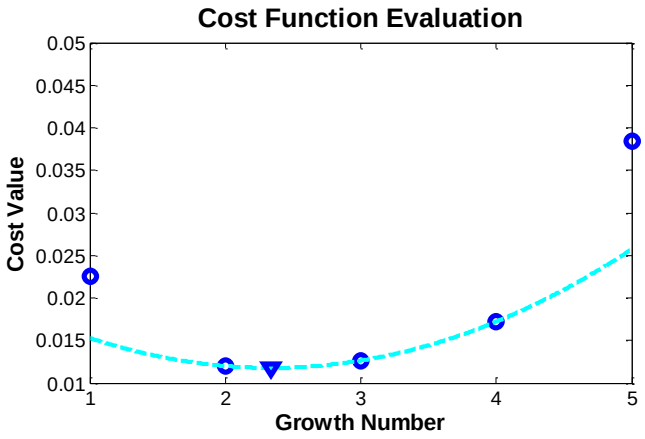

Figure 3.31. The minimum of the curve is determined for the quadratic curve fitted for the three most recent performance cost values.

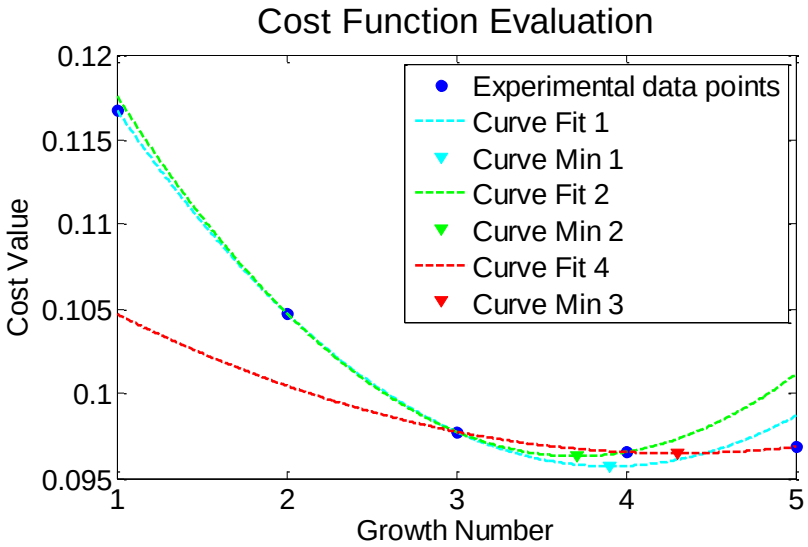

Figure 3.32. The performance cost evaluation for Sample A with a weighting value of 0.5. The performance values are shown with blue dots. The minimum of the curve is determined for the quadratic curve fitting for each sequential set of three performance cost values, and is shown with an inverted triangle with a color matching the quadratic curve.

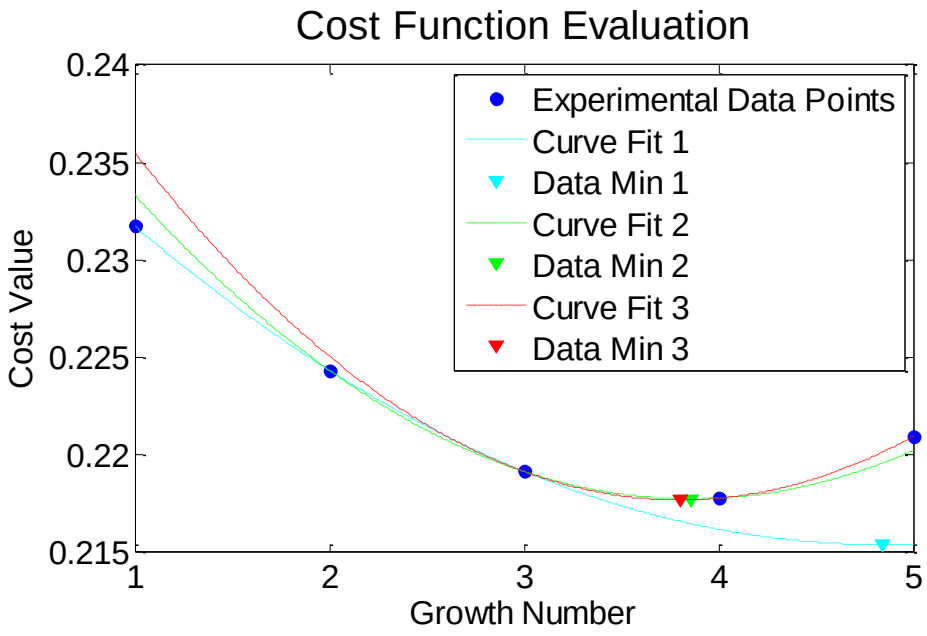

Figure 3.33. The performance cost evaluation for Sample B with a weighting value of 0.5. The minimum of the curve is determined for the quadratic curve fitting for each sequential set of three performance cost values, and is shown with an inverted triangle.

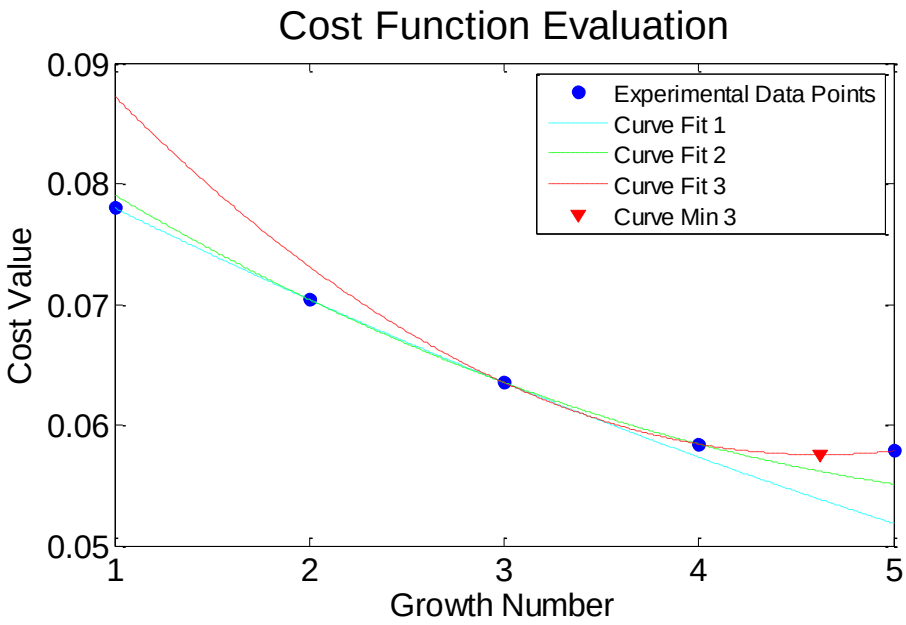

Figure 3.34. The performance cost evaluation for Sample C with a weighting value of 0.5. The minimum of the curve is determined for the quadratic curve fitting for each sequential set of three performance cost values, and is shown with an inverted triangle.

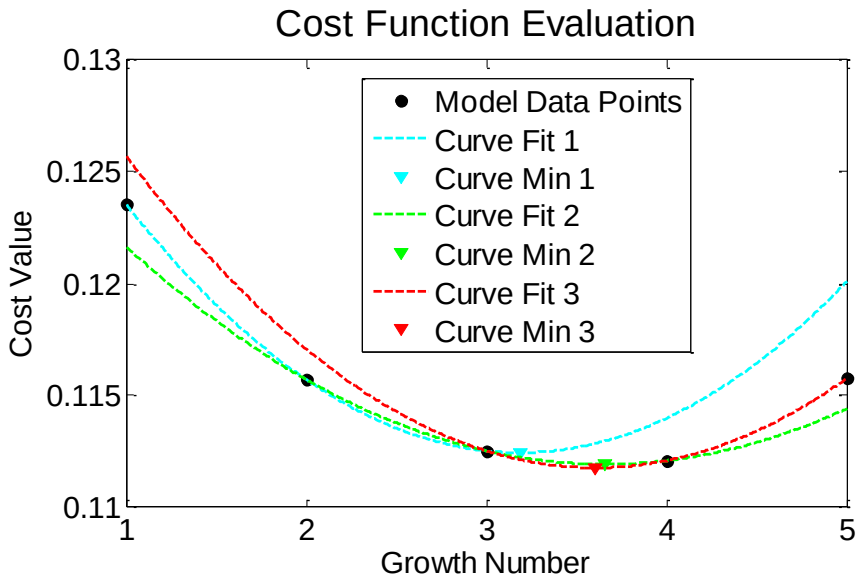

Figure 3.35. The performance cost evaluation for Sample A model data with a weighting value of 0.5. The minimum of the curve is determined for the quadratic curve fitting for each sequential set of three performance cost values, and is shown with an inverted triangle.

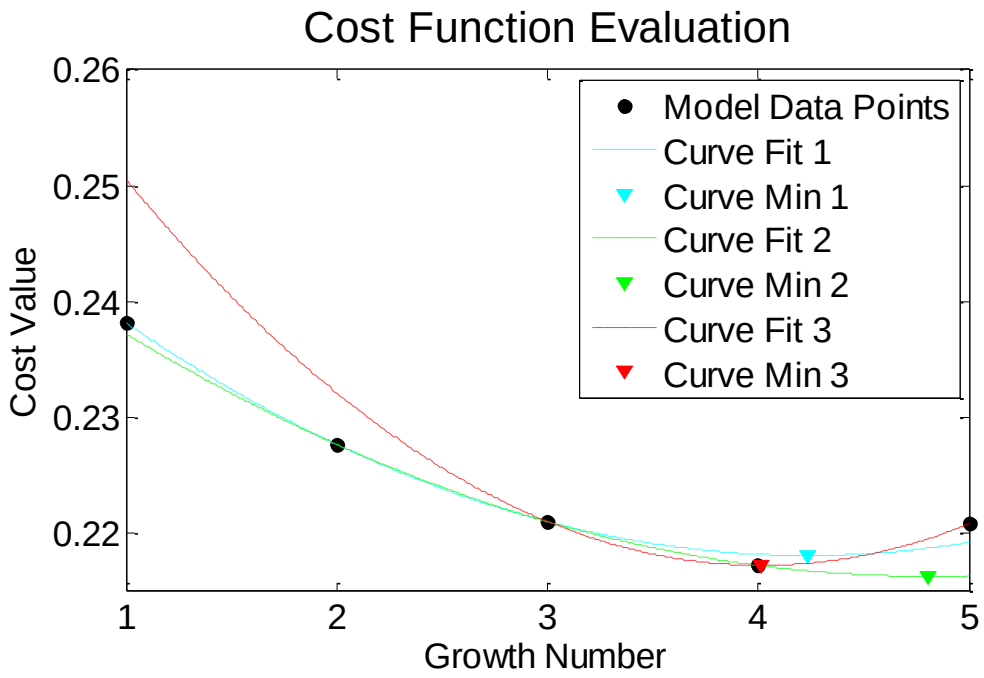

Figure 3.36. The performance cost evaluation for Sample B model data with a weighting value of 0.5. The minimum of the curve is determined for the quadratic curve fitting for each sequential set of three performance cost values, and is shown with an inverted triangle.

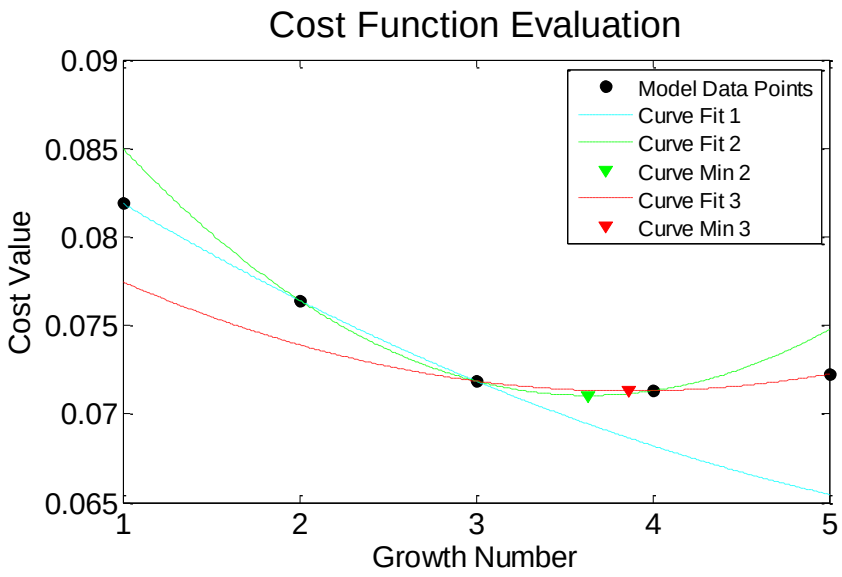

Figure 3.37. The performance cost evaluation for Sample C model data with a weighting value of 0.5. The minimum of the curve is determined for the quadratic curve fitting for each sequential set of three performance cost values, and is shown with an inverted triangle.

Table 3.1. The performance cost evaluation for Samples A, B, and C: experimental and model data with a weighting value of 0.5.

Sample	Weighting Value	Performance Cost Value	1	2	3
A	0.5	Experimental	3.9	3.7	4.3
		Model	3.2	3.7	3.6
B	0.5	Experimental	4.8	3.9	3.8
		Model	4.2	4.8	4.0
C	0.5	Experimental	12.3	6.3	4.6
		Model	7.5	3.6	3.5

Table 3.2. The performance cost evaluation for Sample A: experimental and model data with weighting values of 0.3, 0.1, and 0.7.

Sample	Weighting Value	Performance Cost Value	1	2	3
A	0.3	Experimental	3.7	4.4	5.9
		Model	3.5	4.6	4.6
A	0.1	Experimental	3.6	5.3	6.9
		Model	3.6	5.2	5.8
A	0.7	Experimental	5.2	3.2	1.4
		Model	1.6	1.8	2.8

Table 3.3. The performance cost evaluation for Sample B: experimental and model data with weighting values of 0.3 and 0.7.

Sample	Weighting Value	Performance Cost Value	1	2	3
B	0.3	Experimental	4.3	7.1	6.4
		Model	4.5	14.8	5.1
B	0.7	Experimental	2.3	2.5	2.7
		Model	3.3	2.8	3.1

3.10 References

[1] G. M. Spinks, G. G. Wallace, J. Ding, D. Zhou, B. Xi, and J. Gillespie, "Ionic liquids and polypyrrole helix tubes: bringing the electronic Braille screen closer to reality," in *Smart Structures and Materials*, 2003, pp. 372-380.

[2] J. D. Madden, N. A. Vandesteeg, P. A. Anquetil, P. G. Madden, A. Takshi, R. Z. Pytel*, et al.*, "Artificial muscle technology: physical principles and naval prospects," *Oceanic Engineering, IEEE Journal of,* vol. 29, pp. 706-728, 2004.

[3] T. Shoa, J. D. Madden, C.-W. E. Fok, and T. Mirfakhrai, "Rate limits in conducting polymers," *Advances in Science and Technology,* vol. 61, pp. 26-33, 2008.

[4] Y. Wu, D. Zhou, G. M. Spinks, P. C. Innis, W. Megill, and G. G. Wallace, "TITAN: a conducting polymer based microfluidic pump," *Smart Materials and Structures,* vol. 14, p. 1511, 2005.

[5] G. Alici and N. N. Huynh, "Predicting force output of trilayer polymer actuators," *Sensors and Actuators A: Physical,* vol. 132, pp. 616-625, 2006.

[6] R. Baughman, "Conducting polymer artificial muscles," *Synthetic Metals,* vol. 78, pp. 339-353, 1996.

[7] E. Smela, "Conjugated polymer actuators for biomedical applications," *Advanced Materials,* vol. 15, pp. 481-494, 2003.

[8] Y. Tadesse, R. W. Grange, and S. Priya, "Synthesis and cyclic force characterization of helical polypyrrole actuators for artificial facial muscles," *Smart Materials and Structures,* vol. 18, 2009.

[9] T. W. Secord and H. H. Asada, "A humanoid foot with polypyrrole conducting polymer artificial muscles for energy dissipation and storage," in *Robotics and Automation, 2007 IEEE International Conference on*, 2007, pp. 2904-2909.

[10] S. Hara, T. Zama, W. Takashima, and K. Kaneto, "Polypyrrole-metal coil composite actuators as artificial muscle fibres," *Synthetic Metals,* pp. 47-55, 2004.

[11] S. Hara, T. Zama, W. Takashima, and K. Kaneto, "Free-standing polypyrrole actuators with response rate of 10.8%s-1," *Synthetic Metals,* vol. 149, pp. 199-201, 2005.

[12] S. Hara, T. Zama, W. Takashima, and K. Kaneto, "TFSI-doped polypyrrole actuator with 26% strain," *Journal of Materials Chemistry,* vol. 14, pp. 1516-1517, 2004.

[13] P. A. Anquetil, D. Rinderknecht, N. A. Vandesteeg, J. D. Madden, and I. W. Hunter, "Large strain actuation in polypyrrole actuators," in *Proc. of SPIE Vol*, 2004, p. 381.

[14] J. Ding, L. Liu, G. M. Spinks, D. Zhou, G. G. Wallace, and J. Gillespie, "High performance conducting polymer actuators utilising a tubular geometry and helical wire interconnects," *Synthetic Metals,* pp. 391-398, 2003.

[15] I. W. Hunter and S. Lafontaine, "A comparison of muscle with artificial actuators," in *Solid-State Sensor and Actuator Workshop, 1992. 5th Technical Digest, IEEE*, 1992, pp. 178-185.

[16] J. Sarrazin and S. A. Mascaro, "Sequential growth and monitoring of a polypyrrole actuator system," in *SPIE Smart Structures and Materials+ Nondestructive Evaluation and Health Monitoring*, 2014, pp. 90563L-90563L-11.

[17] J. D. W. Madden, "Conducting polymer actuators," PhD, Massachusetts Institute of Technology, 2000.

[18] P. G. A. Madden, "Development and modeling of conducting polymer actuators and the fabrication of a conducting polymer based feedback loop," PhD, Massachusetts Institute of Technology, 2003.

[19] A. A. A. Moghadam, K. Torabi, M. Moavenian, and R. Davoodi, "Dynamic modeling and robust control of an L-shaped microrobot based on fast trilayer polypyrrole-bending actuators," *Journal of Intelligent Material Systems and Structures,* vol. 24, pp. 484-498, 2013.

[20] Y. Fang, X. Tan, and G. Alici, "Robust adaptive control of conjugated polymer actuators," *Control Systems Technology, IEEE Transactions on,* vol. 16, pp. 600-612, 2008.

[21] J. D. Madden, P. G. Madden, and I. W. Hunter, "Conducting polymer actuators as engineering materials," in *Proceedings of SPIE*, 2002, p. 176.

[22] J. F. Rubinson and Y. P. Kayinamura, "Charge transport in conducting polymers: insights from impedance spectroscopy," *Chemical Society Reviews,* vol. 38, pp. 3339-3347, 2009.

[23] T. Shoa, J. D. Madden, N. R. Munce, and V. Yang, "Analytical modeling of

a conducting polymer-driven catheter," *Polymer International,* vol. 59, pp. 343-351, 2010.

[24] T. Shoa, D. S. Yoo, K. Walus, and J. D. W. Madden, "A dynamic electromechanical model for electrochemically driven conducting polymer actuators," *Mechatronics, IEEE/ASME Transactions on,* vol. 16, pp. 42-49, 2011.

[25] C. H. Nguyen, G. Alici, and G. G. Wallace, "Modelling trilayer conjugated polymer actuators for their sensorless position control," *Sensors and Actuators A: Physical,* vol. 185, pp. 82-91, 2012.

[26] C. H. Nguyen, G. Alici, and G. Wallace, "An Advanced Mathematical Model and its Experimental Verification for Trilayer Conjugated Polymer Actuators," *Mechatronics, IEEE/ASME Transactions on,* vol. 19, pp. 1279-1288, 2013.

[27] W. Zheng, J. M. Razal, G. M. Spinks, V. T. Truong, P. G. Whitten, and G. G. Wallace, "The role of unbound oligomers in the nucleation and growth of electrodeposited polypyrrole and method for preparing high strength, high conductivity films," *Langmuir,* vol. 28, pp. 10891-7, Jul 24 2012.

[28] D. B. McCombie, T. W. Secord, and H. H. Asada, "Modeling and observer design for polypyrrole conducting polymer actuator control systems," presented at the *The First IEEE/RAS-EMBS International Conference on Biomedical Robotics and Biomechatronics*, 2006.

CHAPTER 4

MODEL-BASED PD CONTROL

4.1 Abstract

Electroactive polymers (EAPs) are demonstrating increased use and possible applications at the microscale, and also at the macroscale due to their performance which is comparable to human muscle mechanical performance. The recent inclusion of sequential growth steps during operation increases the range of possible uses. This necessitates the need for enhanced modeling and control. Both tasks are made more complex due to the problems with obtaining trustworthy feedback. Also, previous work aimed at identifying a model for control requires a certain amount of calibration time for system identification. This work shows a simplified model-based PD feedback control that can be adjusted and adapted over each growth step. Also, the simplified model is shown to accurately represent actuator performance, and the change in actuator performance over multiple growth stages.

4.2 Introduction

Electroactive polymer (EAP) actuators are being applied to a variety of sensors and actuators [1, 2]. Conducting polymers are a subset of EAPs that

generate a change in volume in response to an electrical input causing ion migration. Specifically, polypyrrole based actuators are smart material actuator candidates due to their low activation voltage and current, biocompatibility, and mechanical performance reaching stresses over 20 MPa, strains over 20 %, and strains rates over 10 %s-1 [3-7], which is comparable to human muscle. Along with the performance characteristic, limitations exist in the form of repeatable manufacturability, large time constants [8, 9], unidentified system dynamics, hysteresis, drift, and poor lifetimes [10-12]. Although adjusting the actuator system chemistry and manufacturing has shown improvements in performance [4, 5, 13], this work applies methods based upon a simplified system model that is updated during operation.

Polypyrrole actuators have been one of the actuator materials to fall in the category of ‘artificial muscles’ and this is made more accurate due to the recent inclusion of sequential growth steps during operation. Sequential growth is the ability to grow more polymeric material with certain actuator architectures and support systems to adjust actuator performance during the operational life cycle of the actuator. In the case of polyprrole-metal coil composite actuators, an increase in polymer material shows an increase in force output, but also results in a slower actuation due to the necessary increase in electrical and molecular diffusion in the actuator system [14]. The increase of polypyrrole actuator systems to mimic human muscle through multiple growth steps presents the additional issue of making modeling and control more complex since each growth step produces a new system and response. This is another reason to use a

control system that can adapt over time, and adapt over multiple growth steps.

Much of the current advances in polypyrrole and similar polymer actuators has been directed at bilayer or trilayer bending actuators. In these configurations, the EAP is synthesized on either one or both sides of a thin, bendable substrate. Activating the polymer would contract or expand the polymer, and since the polymer lies above or below the midline of the entire actuator, the actuator bends.

Robust adaptive control was developed and applied to trilayer polypyrrole actuators by Fang et al. [15]. First, a simplified model was constructed, and then the model parameters were adapted during operation by a self-tuning regulator. The robust adaptive controller proved to effectively reduce tracking error compared to a static model controller and a PID controller, especially after longer periods of operation. A purely feedforward controller is applied to trilayer actuators by John et al. [16] where a frequency analysis is used to identify the system, and then this model is inverted and combined with a low-pass filter to feed the desired input forward. This work presents a controller that combines parts of both of these works and applies to a linear polypyrrole actuator, not a bending actuator.

First, the simplified model is used to determine representative values in the electrical and mechanical systems. These parameters are combined in a model of the polymer system to observe and predict performance, as well as to determine applicable PD gain values. The closed-loop performance is then monitored for each growth stage, and an optimal amount of growth for a desired

weighting value that can favor either speed or strength is determined.

4.3 Experimental and Data Collection

The experimental setup, actuator synthesis, and data collection process is outlined in the previous chapter.

4.4 Control

Position error control was compensated with a closed-loop control algorithm. The closed-loop control uses a conventional proportional derivative (PD) feedback control. PD control was selected to accommodate dynamic, sinusoidal trajectories. An integral control was not included due to the inherent lag with integral control of dynamic trajectories. The unique part of this controller is that the PD gains are calculated for each growth stage based upon the model parameters determined from the RLS algorithm. The open-loop response exhibits a second-order type behavior, so the PD gains are calculated to dictate a response with a settling time of 5 seconds and a damping ratio of at least 0.7. Initial comparisons between the experimental and model data sets for one growth stage are shown in Fig. 4.1. The experimental data set refers to the data obtained by the open-loop Bode plot tests and the simulated model data refers to the model created by performing the recursive least squares analysis during testing and plugging the resulting values into the simplified model. The different data sets exhibit similar root locus plots (as shown in Fig. 4.1). The calculated controller gains were also similar, reiterating that the values determined by the

simulated model determined data could be used to elicit the same desired response in the actual system.

The fourth order state-space system model simplifies down to a third order transfer function, so the experimental model data produces three open-loop poles on the root locus with one being extremely fast and therefore not shown above. The two dominant open-loop poles for the experimental data are located at -6.23×10^{-3} and -1.29×10^{1}. The simulated model root locus was created using the recursively derived values in the state-space representation, so the simulated model data produces four poles and one zero. This summarizes as one fast open-loop pole like the experimental data ($\sim -2 \times 10^{11}$), and three open-loop poles closer to the origin. One open-loop pole is much closer to the origin than the other two, and is positioned near an open-loop zero. Analyzing the model-based root locus beyond the slower pole and zero shows a system with three open-loop poles similar to the experimental data root locus, making both models reduce to a third order model. The open-loop poles from the simulated model are situated at -2.42×10^{-2}, -1.09×10^{-2}, and -2.35×10^{-12}. Due to the proximity of the open-loop pole and zero (-1.05×10^{-11}) near the origin, the two open-loop poles farther from the origin in the simulated model produce the second order open-loop Bode plot response shown previously, and the space between these experimental model open-loop poles is also reflected in the stepped open-loop Bode plot response for the experimental data shown previously. The feedback controller places a closed-loop zero at -2×10^{4} and places the desired closed-loop complex pole pairs at $-2.24 \times 10^{4} \pm 2.24 \times 10^{4}i$ and $-2.56 \times 10^{4} \pm 2.56 \times 10^{4}i$ for the experimental and

simulated models, respectively.

Preliminary tests show that gains calculated to have a larger settling time generally results in inputs that exceed the capability of the potentiostat and potentially exceed the safe input to the polymer actuators. To compensate, the proportional gain values were reduced to 20% of the calculated value. This greatly changed the closed-loop poles to be at $-5.12\text{x}10^{-1} \pm 1.33\text{x}10^{2}\text{i}$ and $-4.85\text{x}10^{-1} \pm 1.36\text{x}10^{2}\text{i}$ for the experimental and simulated models, respectively. The additional closed-loop zero in the simulated model data does not move from the open-loop position of $-1.05\text{x}10^{-11}$ in the closed-loop root locus, but the open-loop pole at $-2.35\text{x}10^{-12}$ quickly moves to an actual closed-loop position at the zero of $-1.05\text{x}10^{-11}$, where they effectively cancel each other, leaving the complex pair as the dominant closed-loop poles. Further testing is required to determine the most optimal way to incorporate pole placement techniques within the confines of hardware limitations. The entire control scheme diagram is shown below in Fig. 4.2.

4.5 Results and Discussion

The testing results from a closed-loop control example are shown below in Fig. 4.3. PD feedback control supplied accurate tracking at lower frequencies.

The frequency results from the open-loop and closed-loop control over the multiple growth steps are shown below. This PD feedback control extended the achievable frequency approximately two orders of magnitude from the open-loop results.

4.5.1 Frequency Results

This PD feedback results for Sample A are shown in Fig. 4.4. The magnitudes are close to and slightly above zero at the lower frequencies. This illustrates the improved tracking of the polymer with the use of feedback control since the ideal case where the ratio of actual to desired displacement is 1 would have a Bode plot magnitude value of 0 dB. This trend continues up to a frequency less than 10^0 Hz. At this point, the experimental values take a noticeable dip, and then continue to decrease as the testing frequency increases.

The phase response exhibits a similar response as the open-loop response by decreasing in value, pausing, and then decreasing again. The differences are that the first decrease is at a frequency almost two orders of magnitude larger than the open-loop response, and the pause and final phases are not as low as the open-loop response. The closed-loop response pauses at just above -20 degrees and then finally reaches -90 degrees.

The differences between growth stages follow a similar behavior as the open-loop control where an increase in growth equates to an increase in magnitude. The closed-loop response for Samples B and C (shown in Fig. 4.5 and Fig. 4.6, respectively) are similar to Sample A with an extended magnitude behavior up to approximately 10^0 Hz and then a dip and continuing decrease in magnitude response. The closed-loop phase responses follow similar behaviors as well.

4.5.2 Frequency and Model Results

The model parameters determined with the open-loop experiments were combined with the PD gain values, and the model control predictions shown in Fig. 4.7. The model-based feedback control frequency response for Sample A shows a consistent linear magnitude response for the lower frequencies, and a spiking increase in magnitude that is followed by a rapid decline in magnitude. The decline in magnitude occurs at a similar point to the dip in experimental data points. Similar to the experimental points, the model based curves increase in magnitude with increasing growth stage, and then dip down sooner as frequency value is increased. The phase response from the model is also much different from the experimental data, taking a large dip down to approximately -140 degrees, and then rising up to -90 degrees. This rise is likely due to the influence of the slightly different algorithm used to determine the simulated model data and create an additional closed-loop zero near the origin. Although the two formulations are different, the difference occurs at a higher frequency where performance degrades. The model also greatly varies from the experimental data at these higher frequencies requiring model refinement for operation at higher frequencies. The need to reduce the desired gain based upon hardware restrictions also created an underdamped system in the root locus analysis (shown in Fig 4.1). This underdamped system is represented by the resonance peak in the magnitude portion of the model-based Bode plots, for example, in Fig. 4.7. The model-based control response for Sample B is similar to Sample A with the noticeable spike and decrease in behavior. The model-based responses

from Sample B in Fig. 4.8 exhibit almost an overlapping behavior as the frequency values are increased. The phase response takes the same noticeable dip as seen with the model data response for Sample A. The model based frequency predictions are also similar for Sample C in Fig. 4.9, except for the more widely distributed response between growth stages as the frequency is increased. The phase response is similar to Sample B and Sample C, and the wide distribution can also be observed here.

4.5.3 Cutoff Values

The cutoff values were determined by the same means as the open-loop response. The main difference was that only straight lines were used to be fitted to the data and the cutoff value determined. This was in lieu of the additional step of fitting a curve to the lines since the behavior of the open-loop data was not necessarily identified as a common Bode plot behavior curve.

The initial cutoff magnitude for Sample A shown in Fig. 4.10 is approximately 0.71 dB and rises between 0.05 dB and 0.3 dB until it reaches 1.4 dB during the 5^{th} growth cycle. The cutoff frequency starts at approximately 0.89 Hz and decreases between 0.1 Hz and 0.2 Hz to reach 0.41 Hz at the 5^{th} growth cycle.

Sample B has an initial cutoff magnitude of approximately 0.22 dB and rises between 0.0 dB and 0.09 dB each growth stage to end up at 0.38 dB. The cutoff frequencies for Sample B start at just below 0.8 Hz and decrease between 0.01 Hz and 0.2 Hz at each growth stage to end up just above 0.3 Hz.

The cutoff magnitudes for Sample C start at approximately 0.47 dB and rise

between 0.08 dB and 0.15 dB during each growth stage to end up at 0.82 dB. The cutoff frequencies for Sample C start at approximately 0.9 Hz and decrease between 0.05 Hz and 0.2 Hz during each growth stage to end up just above 0.5 Hz. Next, the model data were analyzed.

The initial cutoff magnitude for the Sample A model data is approximately 0.65 dB and rises between 0.05 dB and 0.3 dB until it reaches 1.35 dB during the 5^{th} growth cycle. The cutoff frequency starts at approximately 0.35 Hz and decreases approximately 0.02 Hz to reach 0.25 Hz at the 5^{th} growth cycle.

The Sample B model data have an initial cutoff magnitude of approximately 0.18 dB and rise between 0.01 dB and 0.08 dB each growth stage to end up at 0.345 dB. The cutoff frequencies for Sample B start at just above 0.3 Hz and decrease approximately 0.01 Hz at each growth stage to end up just below 0.3 Hz.

The cutoff magnitudes for the Sample C model data start at approximately 0.45 dB and rise between 0.03 dB and 0.12 dB during each growth stage. The cutoff frequencies for Sample C start at approximately 0.7 Hz and decrease between 0.02 Hz and 0.25 Hz during each growth stage to end up just above 0.3 Hz.

4.5.4 Cost Performance Values

The performance values are displayed for the closed-loop tests, as well as the open-loop experiments from the previous chapter. The performance values for Sample A all fall between three and just above four and are shown in Table

4.1.

The first two optimal performance values from both the experimental and model closed-loop results of Sample A show an optimal amount of growth to be between three and three and a half. The third optimal performance value from both sets of data recommends a fourth stage of growth to reach the optimal amount. For Sample A, the closed-loop test values follow a similar trend to the open-loop test values which start at approximately three and increase to approximately four as the number of algorithm analysis values increase. For all three values, the model values are larger than the experimental values, and there is never a difference over 0.3 between the experimental and model data sets for the closed-loop analysis.

The optimal growth values for Sample B in Table 4.2 show a successive increase from just under three to just under four for the experimental data. The model data make a similar increase between the first and second value, and decreases slightly on the third.

For a weighting value of 0.5 on the closed-loop data of Sample B, the optimal amount of growth is calculated to be less than the achieved level of growth. The optimal growth values from the experimental and model never differ more than 0.3 for each growth stage of analysis.

The closed-loop cost performance analysis for Sample C shown in Table 4.3 follows a similar behavior to the model based performance values from the open-loop analysis. The first optimal growth value for the closed-loop experimental and model data is at least two additional stages. After this stage, the optimal growth

is reduced, but the additional optimal performance values do not differ more than 0.1 between the experimental and model values.

4.5.5 Maximum Gain Algorithm

The PD gains used in the closed-loop test were formulated at less than optimal conditions due to the fact that the potentiostat has a current magnitude input limit of one amp. The feedback gains were also limited in an effort to limit the current input to avoid over oxidation of the polymer. The relatively small dip in the closed-loop magnitude response alludes to the possibility in selectively increasing the gains at higher magnitudes to improve performance. The amount of gain increase was determined by looking at the phase plot of the frequency response and using the phase offset at the desired frequency to determine the predicted tracking error. The maximum proportional gain possible would then be the largest magnitude that could be multiplied by the error while still maintaining an input less than the value that could exceed the power source's capability or polymer safety limit.

To avoid needing extensive frequency tests, the phase shift could be taken by the phase shift predicted by the model data, but the error between the experimental data and model data is too great. The model data were used to create a more accurate, but still conservative phase shift estimate. The model phase shift data start at 0 degrees and takes a large dip to approximately -135 degrees before leveling out at -90 degrees. The experimental data phase shift makes a much smaller shift and then gradually decreases to -90 degrees. The

conservative phase prediction uses a negative arc tangent curve to predict the actual phase shift from the model data. The conservative phase prediction starts at -10 degrees at the lower frequencies. The center of the arc tangent curve was determined by finding the midpoint frequency between where the model frequency takes its initial dip in magnitude from 0 degrees and where the frequency rises to meet the final phase value of -90 degrees. The change in magnitude for the arc tangent will always be from the initial -10 degrees to the final -90 degrees. The goal is to create a predictive phase behavior that is consistently conservative, but also follows the general behavior of the experimental data. The predictive phase plot for Sample A is shown below in Fig. 4.11.

The resulting predictive phase curve approaches the dip in experimental data, but manages to remain conservative and below the experimental data. Next, the conservative phase plot curve can be used to reference the phase shift at any frequency, and that frequency can be used to calculate the ideal error in tracking. The maximum allowed input current divided by the calculated maximum frequency provides the maximum allowable increase in proportional gain from the already assigned, 'safe' PD gains. This gain calculation algorithm now adjusts the previous model diagram to further refine the PD gain selections. The entire system schematic is shown in Fig. 4.12.

4.6 Conclusion

Sequentially grown polypyrrole-metal coil composite actuators were synthesized, and a feedback PD controller instituted. First, a simplified model was used to track representative model parameters. Then, multiple frequency tests were performed to track actuator performance. Both the experimental and model data were compared to determine representative speed and strength parameters and these were combined in a cost performance analysis. Although the closed-loop cost performance points did not produce better optimal growth predictions than the open-loop results determined in the previous chapter, the model followed the experimental data closely. Finally, in an effort to maximize feedback control performance, an algorithm was created to determine the maximum proportional gain at higher frequencies where performance decreases.

4.7 Acknowledgements

The authors would like to thank Dr. Debra Mascaro and Dr. Kent Udell for use of their facilities and lab space.

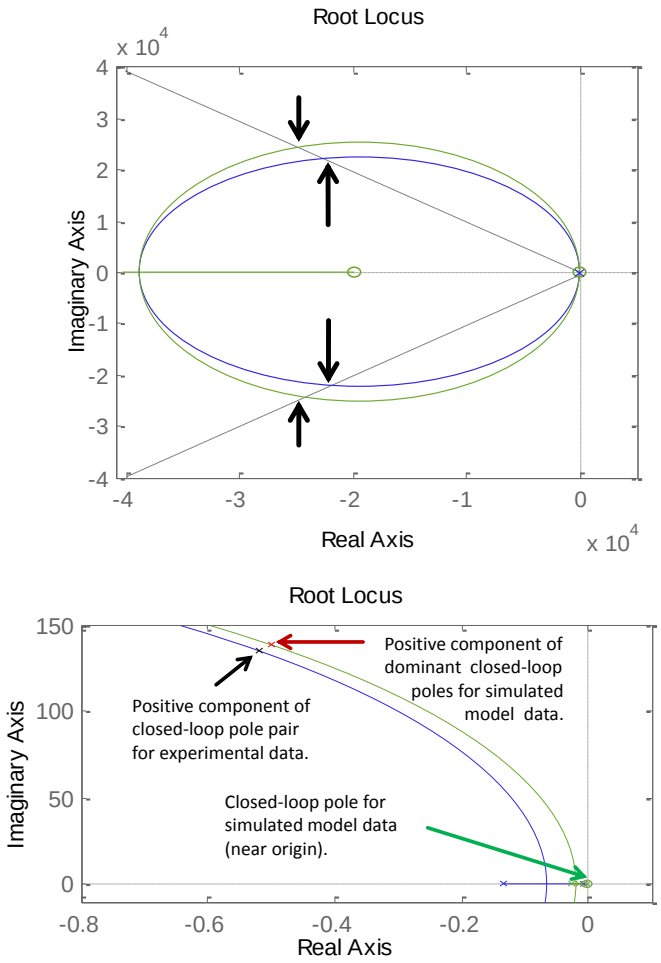

Figure 4.1. Close-up root loci of experimental and simulated models for one growth stage at two different scales with the experimental data shown in blue and the simulated model shown in green. The dashed angled lines represent a damping ratio of 0.7 and the black arrows show the placement of the desired closed-loop pole pairs in the first plot. The poles and arrows in the second plot show the determined closed-loop poles due to hardware restrictions (black for experimental data and red for simulated model data).

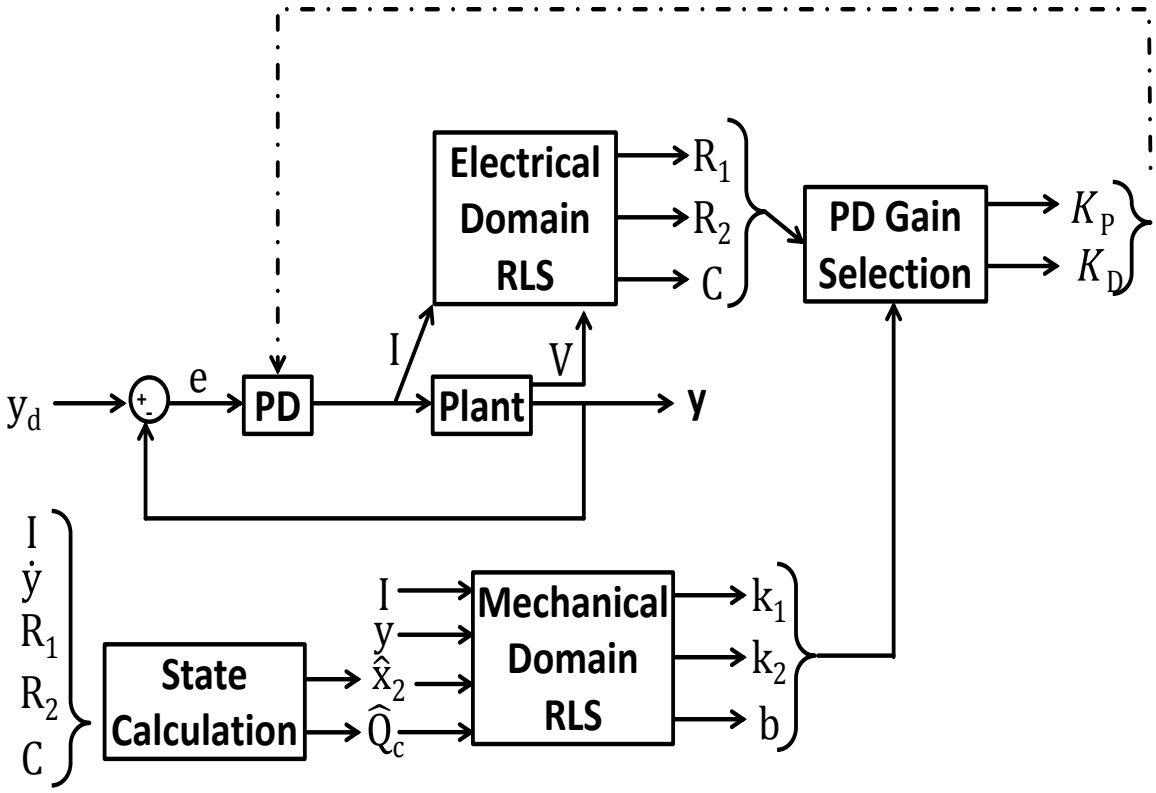

Figure 4.2. Block diagram of model parameter analysis and feedback control scheme.

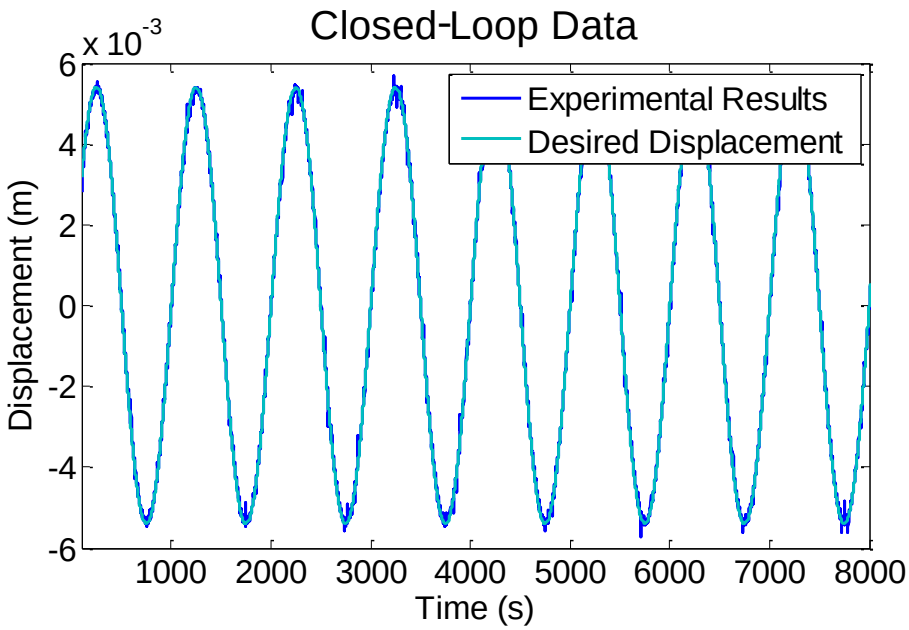

Figure 4.3. Experimental results for a closed-loop frequency test. The desired input is shown in yellow, and the actual is shown in blue.

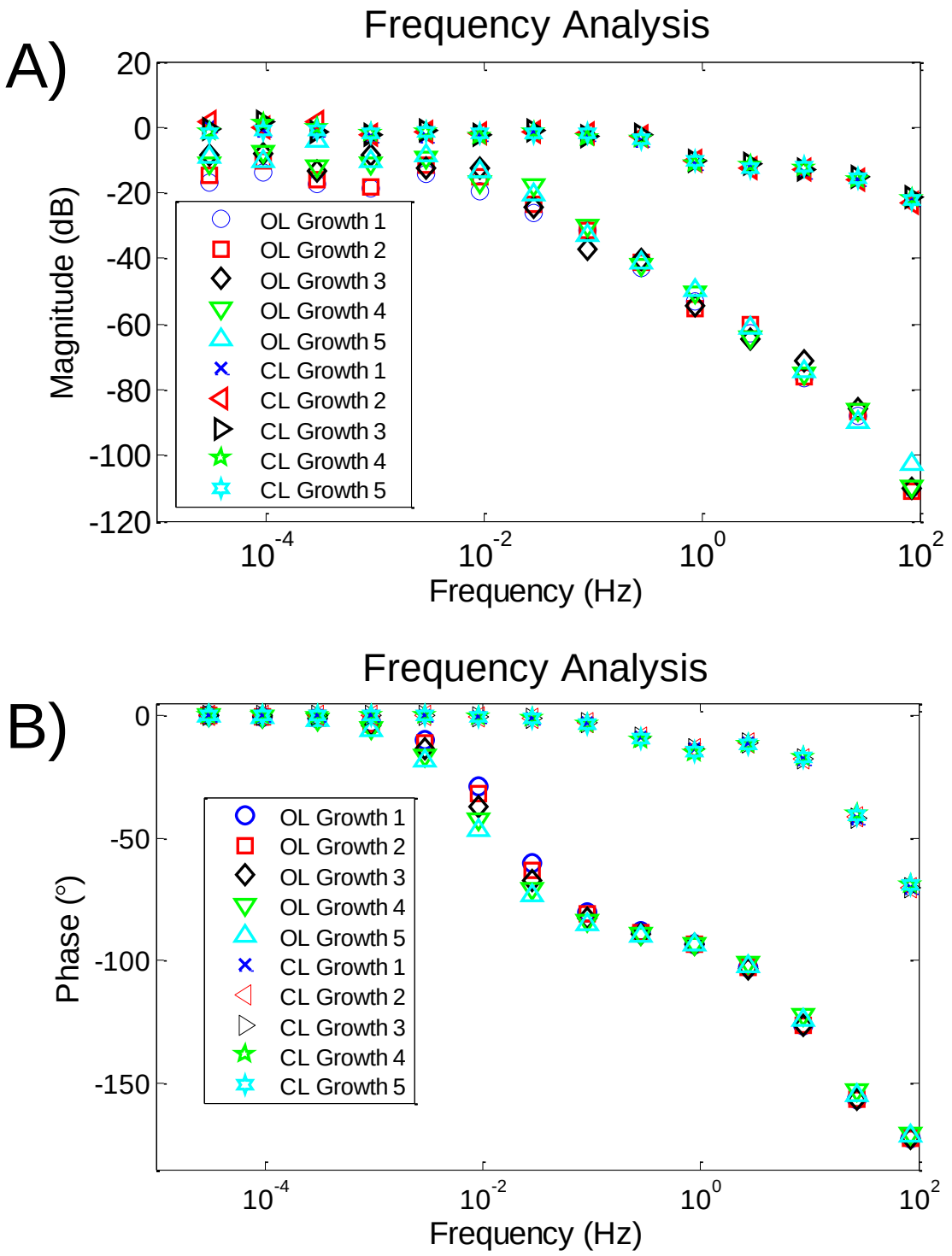

Figure 4.4. Bode plot magnitude results for open-loop and PD feedback control for Sample A. The top plot, A), shows the magnitude response from the Bode analysis while the bottom plot, B), shows the phase response for the Bode analysis.

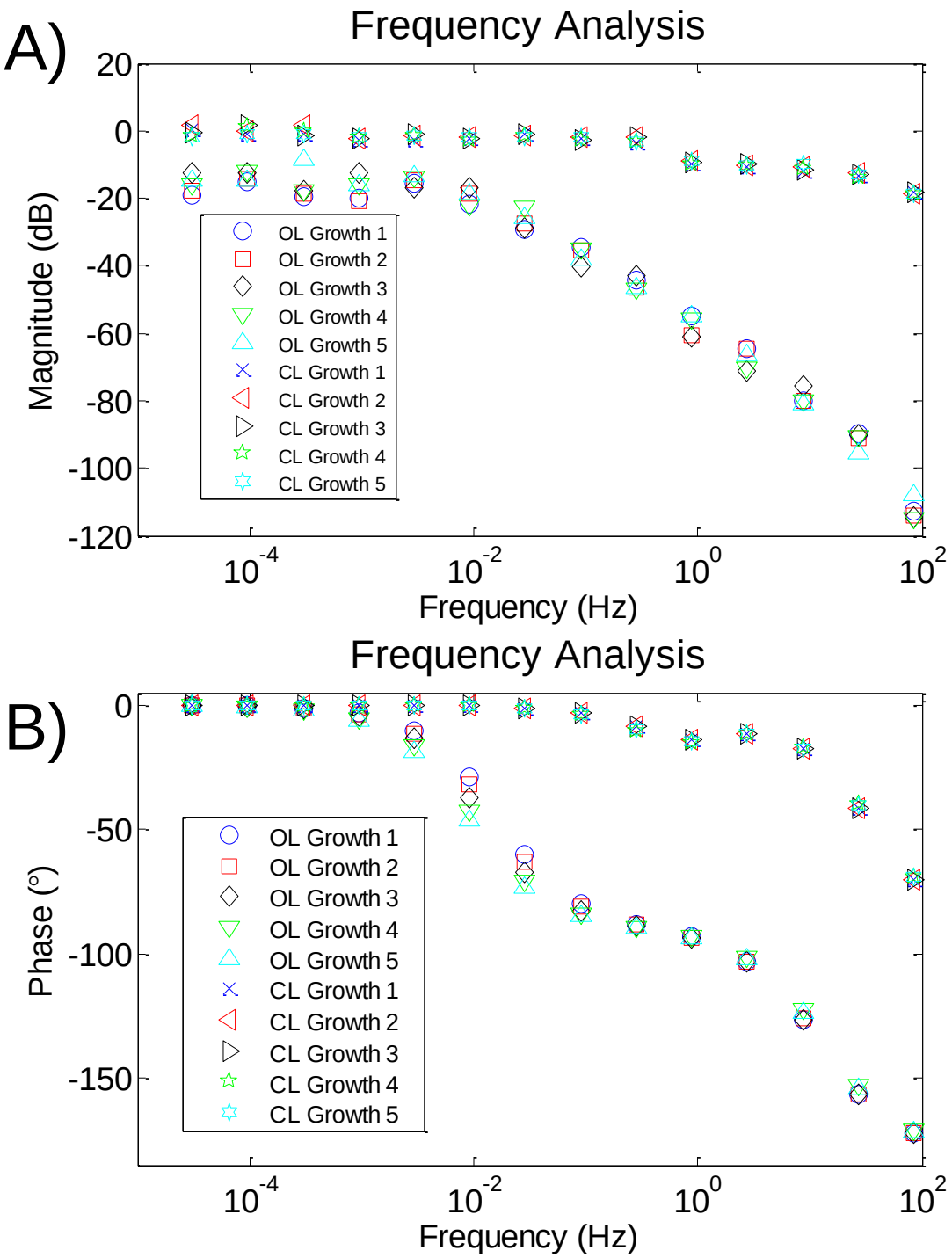

Figure 4.5. Bode plot magnitude results for open-loop and PD feedback control for Sample B. The top plot, A), shows the magnitude response from the Bode analysis while the bottom plot, B), shows the phase response for the Bode analysis.

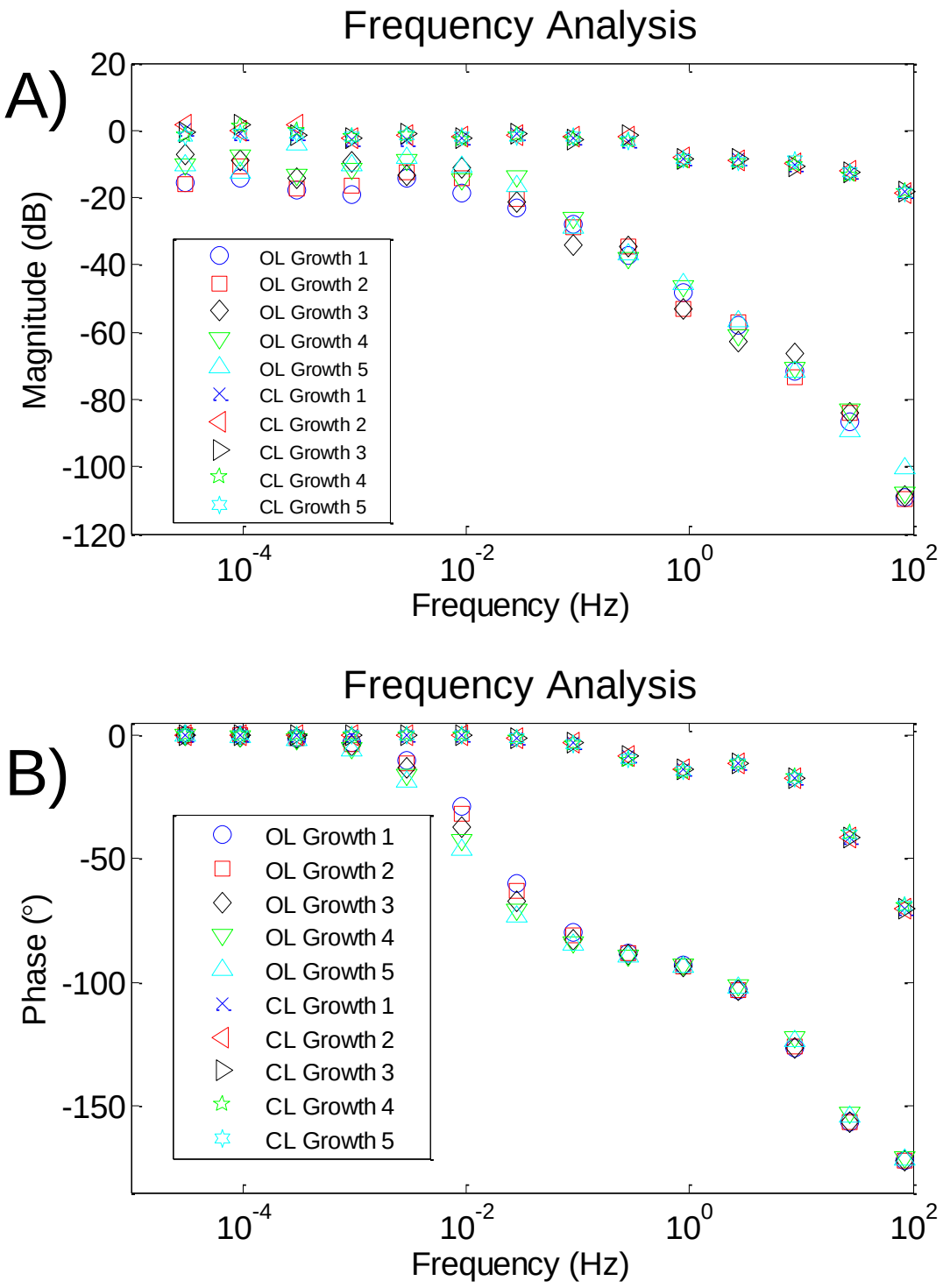

Figure 4.6. Bode plot magnitude results for open-loop and PD feedback control for Sample C. The top plot, A), shows the magnitude response from the Bode analysis while the bottom plot, B), shows the phase response for the Bode analysis.

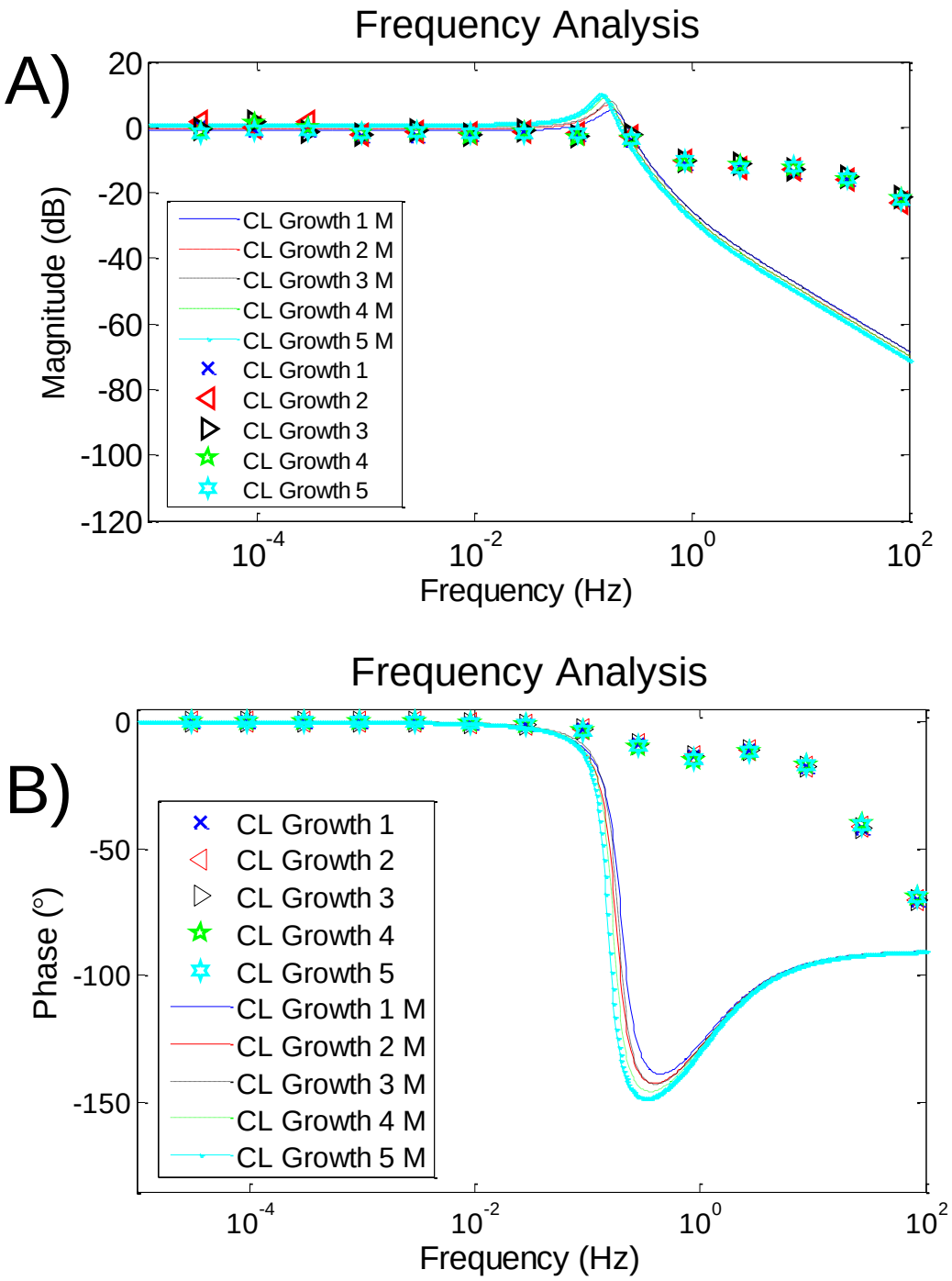

Figure 4.7. Bode plot magnitude results for PD feedback control and model predicted feedback response for Sample A. The top plot, A), shows the magnitude response from the Bode analysis while the bottom plot, B), shows the phase response for the Bode analysis.

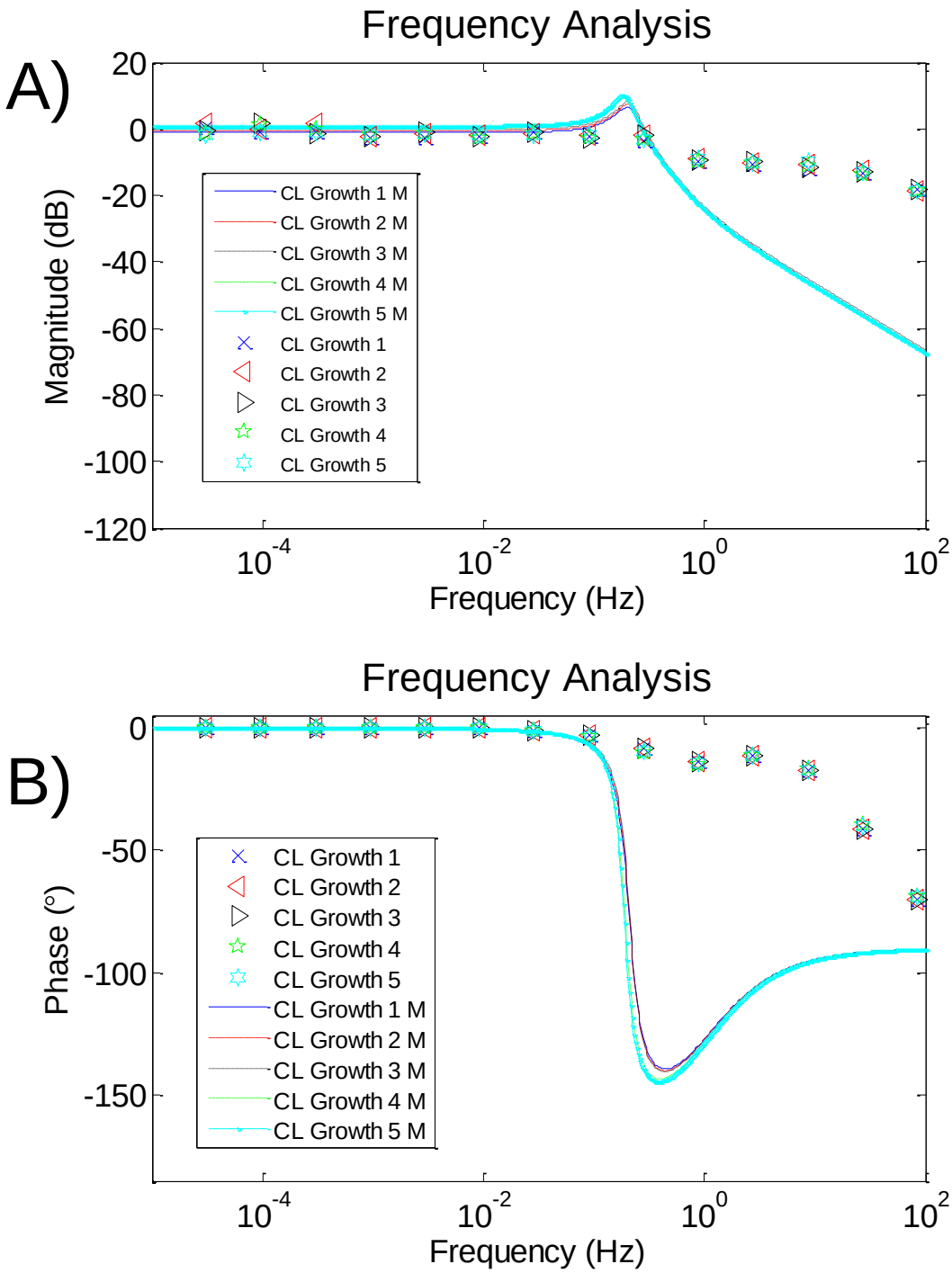

Figure 4.8. Bode plot magnitude results for PD feedback control and model predicted feedback response for Sample B. The top plot, A), shows the magnitude response from the Bode analysis while the bottom plot, B), shows the phase response for the Bode analysis.

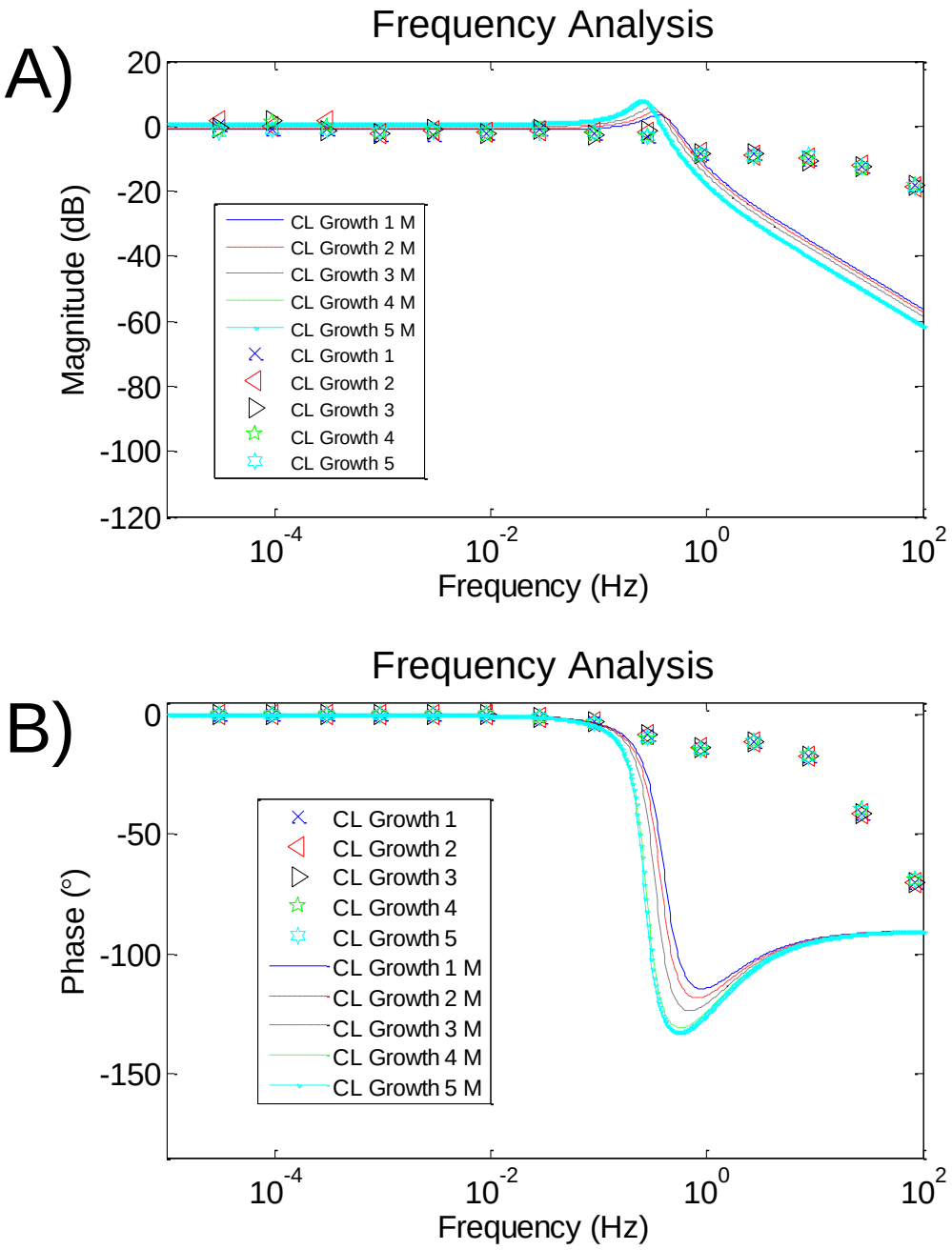

Figure 4.9. Bode plot magnitude results for PD feedback control and model predicted feedback response for Sample C. The top plot, A), shows the magnitude response from the Bode analysis while the bottom plot, B), shows the phase response for the Bode analysis.

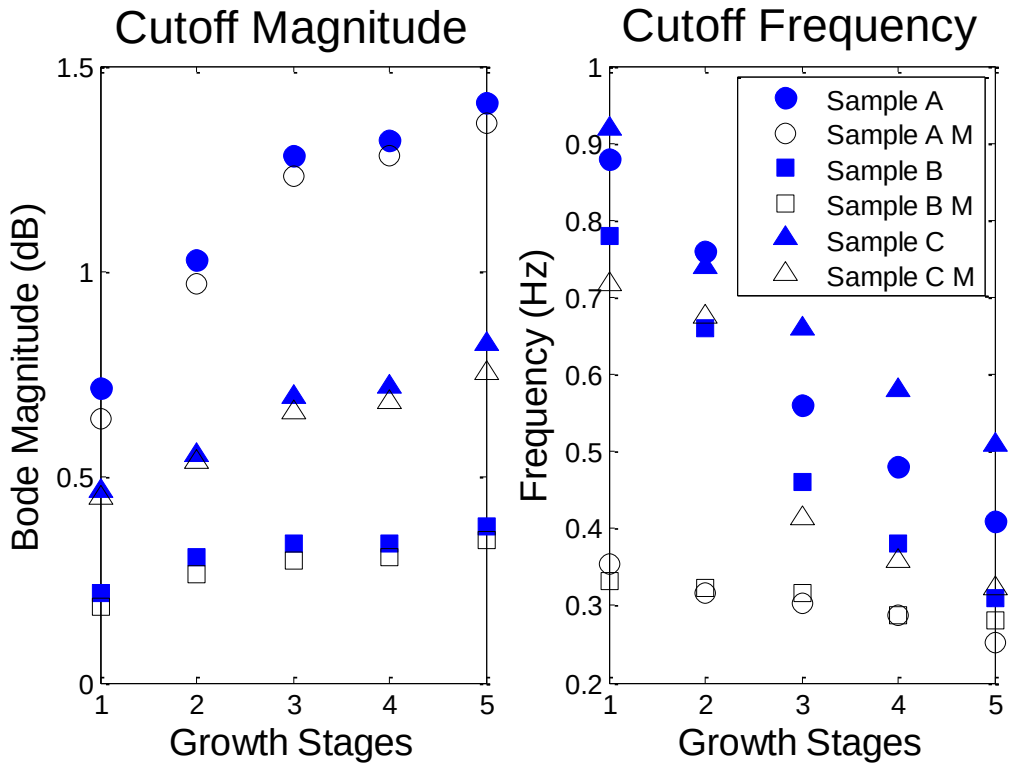

Figure 4.10. The resulting cutoff magnitudes and frequencies from the PD feedback frequency analyses for each growth stage of the samples from both experimental and model data.

Table 4.1. The performance cost evaluation for Sample A: experimental and model data with a weighting value of 0.5.

Sample		Performance Cost Value	1	2	3
A	Open-loop	Experimental	3.9	3.7	4.3
		Model	3.2	3.7	3.6
	Closed-loop	Experimental	3.1	3.5	3.9
		Model	3.3	3.5	4.1

Table 4.2. The performance cost evaluation for Sample B: experimental and model data with a weighting value of 0.5.

Sample		Performance Cost Value	1	2	3
B	Open-loop	Experimental	4.8	3.9	3.8
		Model	4.2	4.8	4.0
	Closed-loop	Experimental	2.7	3.3	3.7
		Model	2.9	3.6	3.4

Table 4.3. The performance cost evaluation for Sample C: experimental and model data with a weighting value of 0.5.

Sample		Performance Cost Value	1	2	3
C	Open-loop	Experimental	12.3	6.3	4.6
		Model	7.5	3.6	3.9
	Closed-loop	Experimental	6.7	3.6	3.3
		Model	5.1	3.6	3.4

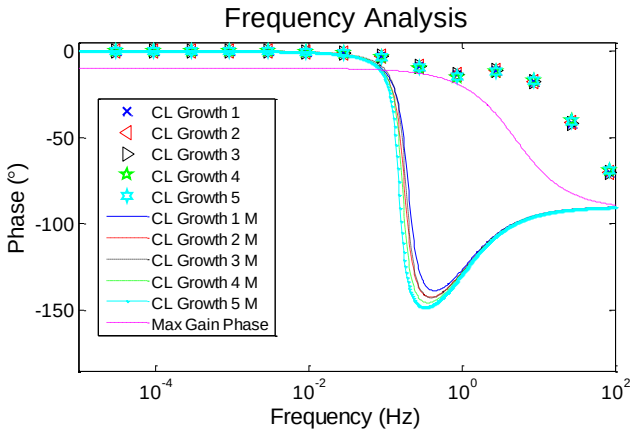

Figure 4.11. The resulting phase plot for the closed-loop experimental and model data, as well as the predictive phase plot using the model data for Sample A.

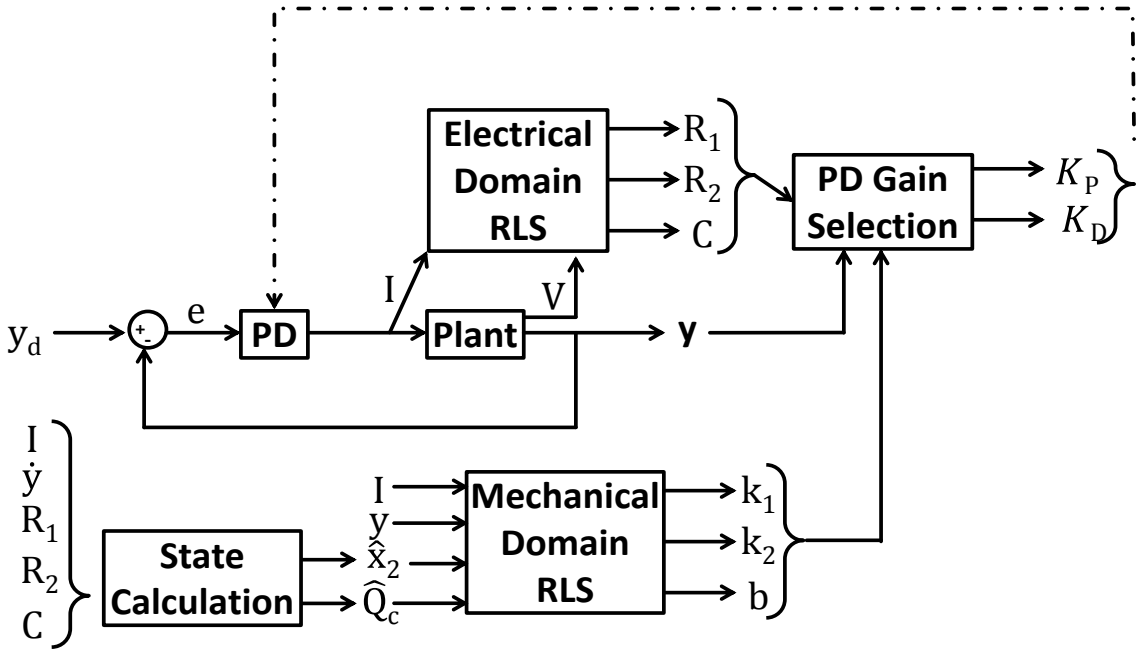

Figure 4.12. Block diagram of model parameter analysis and feedback control scheme using maximum predictive proportional algorithm.

4.8 References

[1] R. Baughman, "Conducting polymer artificial muscles," *Synthetic Metals,* vol. 78, pp. 339-353, 1996.

[2] E. Smela, "Conjugated polymer actuators for biomedical applications," *Advanced Materials,* vol. 15, pp. 481-494, 2003.

[3] S. Hara, T. Zama, W. Takashima, and K. Kaneto, "Polypyrrole-metal coil composite actuators as artificial muscle fibres," *Synthetic Metals,* pp. 47-55, 2004.

[4] S. Hara, T. Zama, W. Takashima, and K. Kaneto, "Free-standing polypyrrole actuators with response rate of 10.8%s-1," *Synthetic Metals,* vol. 149, pp. 199-201, 2005.

[5] S. Hara, T. Zama, W. Takashima, and K. Kaneto, "TFSI-doped polypyrrole actuator with 26% strain," *Journal of Materials Chemistry,* vol. 14, pp. 1516-1517, 2004.

[6] P. A. Anquetil, D. Rinderknecht, N. A. Vandesteeg, J. D. Madden, and I. W. Hunter, "Large strain actuation in polypyrrole actuators," in *Proc. of SPIE Vol*, 2004, p. 381.

[7] J. Ding, L. Liu, G. M. Spinks, D. Zhou, G. G. Wallace, and J. Gillespie, "High performance conducting polymer actuators utilising a tubular geometry and helical wire interconnects," *Synthetic Metals,* pp. 391-398, 2003.

[8] G. Alici and N. N. Huynh, "Predicting force output of trilayer polymer actuators," *Sensors and Actuators A: Physical,* vol. 132, pp. 616-625, 2006.

[9] Y. Wu, G. Alici, G. M. Spinks, and G. G. Wallace, "Fast trilayer polypyrrole bending actuators for high speed applications," *Synthetic Metals,* vol. 156, pp. 1017-1022, 2006.

[10] J. D. Madden, R. A. Cush, T. S. Kanigan, and I. W. Hunter, "Fast contracting polypyrrole actuators," *Synthetic Metals,* vol. 113, pp. 185-192, 2000.

[11] G. Alici and N. N. Huynh, "Performance quantification of conducting polymer actuators for real applications: a microgripping system," *Mechatronics, IEEE/ASME Transactions on,* vol. 12, pp. 73-84, 2007.

[12] P. G. Madden, J. D. Madden, P. A. Anquetil, N. A. Vandesteeg, and I. W.

Hunter, "The relation of conducting polymer actuator material properties to performance," *Oceanic Engineering, IEEE Journal of,* vol. 29, pp. 696-705, 2004.

[13] T. Zama, S. Hara, W. Takashima, and K. Kaneto, "Comparison of conducting polymer actuators based on polypyrrole doped with BF 4−, PF 6−, CF 3 SO 3−, and ClO 4−," *Bulletin of the Chemical Society of Japan,* vol. 78, pp. 506-511, 2005.

[14] J. Sarrazin and S. A. Mascaro, "Sequential growth and monitoring of a polypyrrole actuator system," in *SPIE Smart Structures and Materials+ Nondestructive Evaluation and Health Monitoring*, 2014, pp. 90563L-90563L-11.

[15] Y. Fang, X. Tan, and G. Alici, "Robust adaptive control of conjugated polymer actuators," *Control Systems Technology, IEEE Transactions on,* vol. 16, pp. 600-612, 2008.

[16] S. W. John, G. Alici, and C. D. Cook, "Inversion-based feedforward control of polypyrrole trilayer bender actuators," *Mechatronics, IEEE/ASME Transactions on,* vol. 15, pp. 149-156, 2010.

CHAPTER 5

CONCLUSION

This work presents multiple advancements in the field of electroactive polymer actuators. The main contributions start with (1) a new testing apparatus and synthesis method that allows for multiple, sequential growth steps, (2) the implementation of a simplified model for behavior tracking and optimal growth prediction, and (3) the implementation of proportional-derivative feedback control with gains determined by the simplified model data. These objectives can be combined to create an optimal artificial muscle actuator system that can be recursively fabricated, the control scheme determined, and the optimal amount of growth determined.

The custom testing apparatus allows for the easy change out of different actuators, as well as the ease of operational solution exchanging. The application of sequential growth to helical metal electrodes is novel, and the inclusion of the metal helix as a working electrode allows for the method of sequential growth to be repeated and customize conductive polymer actuators. The amount of growth to reach an optimal state required open-loop operation to determine the optimal state.

The open-loop operation of the conducting polymer actuators illustrated the

available operating range over multiple frequencies, and the change in capability as the number of growth stages is increased. Cutoff values were determined to get representative speed and strength values for each actuator at each growth stage. These values were used in a performance cost analysis to assign a performance value. Although this value could be used to determine the optimal amount of growth, the extensive amount of tests required to acquire the frequency response data makes the process cumbersome. A simplified model was used to determine representative model parameters and perform the same growth analysis and prediction using these model parameters, which can be collected during normal operation. The model determined values proved to provide representative data that could be used to predict optimal growth instead of requiring multiple tests at a range of input frequencies. Next, the open-loop response was improved by implementing closed-loop feedback control.

A proportional-derivative controller was applied to the conducting polymer actuators. Although the PD gain selection was limited by the power source potential and polymer over oxidation, an additional algorithm was presented to find the maximal proportional gain allowable at the larger input frequencies where actuator performance decreases. The closed-loop results also show that the optimal amount of growth is better determined by the open-loop results than the closed-loop results.

These three contributions work in tandem to not only further the state of conducting polymer actuators, but to close the distance separating artificial and actual muscles. They also work in tandem in the recursive actuator optimization

that moves between actuator prototyping, control refinement, and actuator adjustment as necessary. The conducting polymers are artificial muscles, but now have a more dynamic life cycle that can be adjusted as operating conditions and polymer response changes; just like natural muscles.

5.1 Future Work

The first step for future work entails performing multiple actuation tests with a wider variety of amplitudes and trajectories. This will help determine the success and shortcomings of the simplified model. It should also help with the next task of exploring the influence of creep on the actuators.

The current simplified model does not include parameters to model the creep in the system. The model could be expanded to include a creep, damping parameter. The creep influence should be easier to recognize by adjusting the input parameters as mentioned in the previous paragraph.

Another main area to improve upon is the electrolyte selection and actuator geometries. It is possible the novel combination of sequential growth and metal helix could benefit from a different doping electrolyte than the substituents used here. It is also possible to look at different actuator geometries. Previous groups have already looked at incorporating a metal wire as the working electrode in a zigzag pattern resulting in a polymer-metal serpentine arrangement actuator that results in large, flat polymer actuators. This arrangement could increase counter ion transport since both sides of the polymer are exposed to the actuation and growth electrolytic solutions.

Another important aspect to improve upon is determining a method for reliably measuring the polymer thickness during operation without needing to destroy the samples. Characterizing the thickness over multiple cycles, and the amount by which is changed during each growth cycle would improve polymer modeling and optimal growth prediction. A vision system is likely the easiest sensor system to implement, and once the change in thickness is reliably characterized for each growth stage, it may be possible to determine the exact amount of thickness change by the change in simplified model parameters.

Once the simplified model is proven to handle a range of inputs and trajectories, the optimal amount of growth change needed to reach an optimal thickness will have more unique and specific growth stage times and current inputs compared to the constant currents and time periods used in these tests.

APPENDIX A

TESTING APPARATUS

A.1 Equipment

The helical coils were created with a manual hand crank mechanism. The core wire is spun while a guide travels down the core and feeds the coil wire. The model design is shown below in Fig. A.1. The completed mechanism is shown in the Fig. A.2. The image in Fig. A.3 below shows a close up of a partially created coil over the core wire material.

A.2 Test Cell

The first iteration of the assembled test cell is shown in Fig. A.4. The test cell in its disassembled form is shown in Fig. A.5, and a picture showing hand to scale is shown in Fig. A.6.

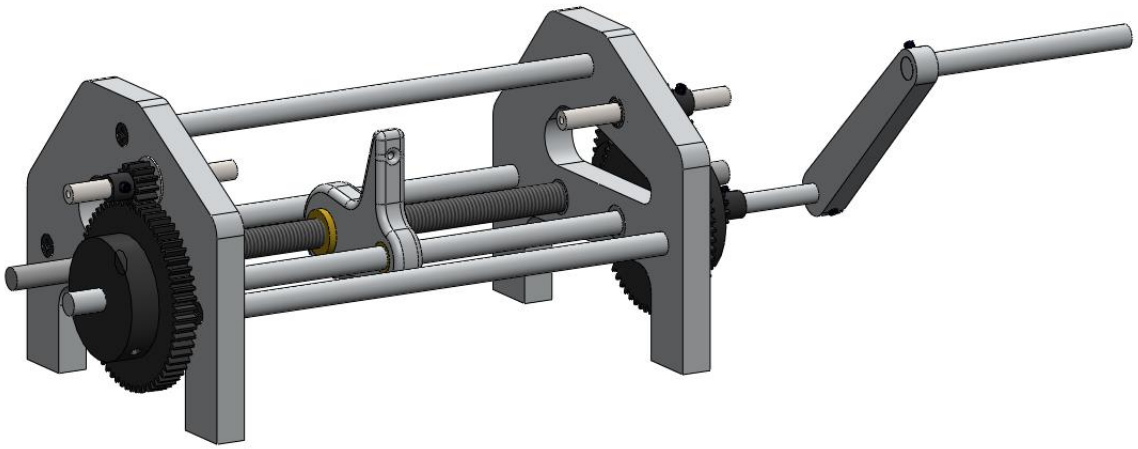

Figure A.1. Schematic of coil winder mechanism used for metal coil creation.

Figure A.2. Picture of coil winder mechanism used for metal coil creation.

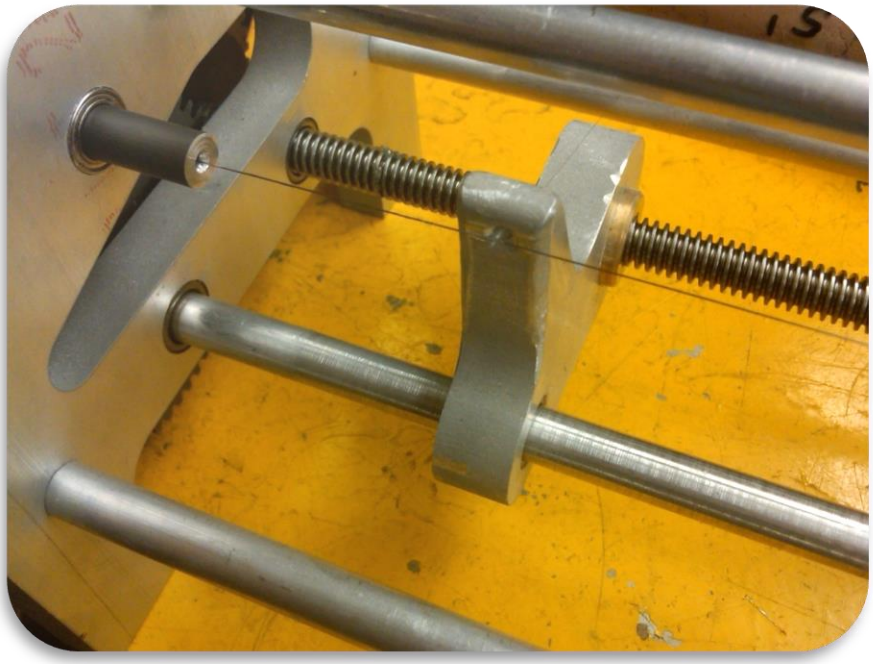

Figure A.3. Close up picture of coil winder mechanism used for metal coil creation.

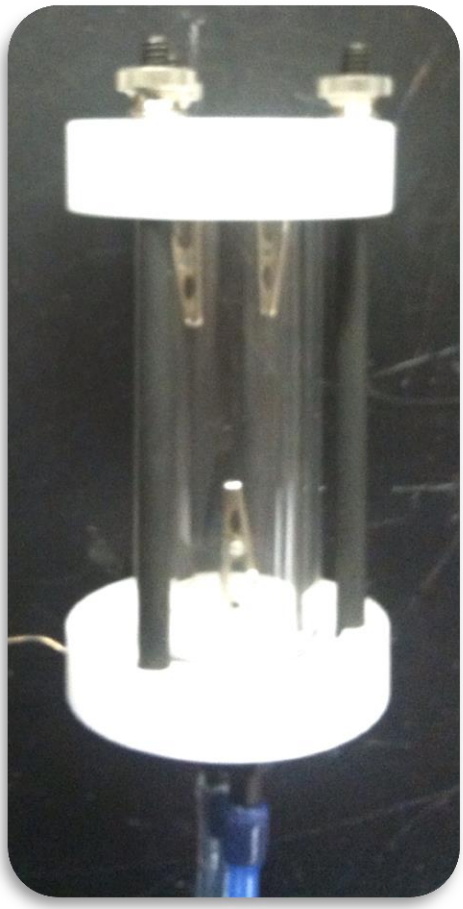

Figure A.4. Picture of the initial test cell used for experimental testing.

Figure A.5. Picture of the initial test cell used for experimental testing disassembled.

Figure A.6. Picture of the initial test cell used for experimental testing.

APPENDIX B

ACTUATOR IMAGES

B.1 Scanning Electron Microscope Images

SEM images for different growth stages of an actuator sample are shown here. The first three images look at one actuator at three different growth stages. The initial growth is shown in Fig. B.1, the additional growth is shown in Fig. B.2, and the next additional growth stage is shown in Fig. B.3.

The next series of figures looks at different magnification scales of polymers synthesized through separate techniques. A continuous growth actuator is shown in Fig. B.4 with a scale bar of 300 µm. The scale bar is decreased to 100 µm in Fig. B.5, 50 µm in Fig. B.6, and 20 µm in Fig. B.7. A sequential growth actuator is shown in Fig. B.8 with a scale bar of 300 µm. The scale bar is decreased to 100 µm in Fig. B.9, 50 µm in Fig. B.10, and 40µm in Fig. B.11.

B.2 Microscope Images

Different input currents influence actuator structure. Three different actuators are shown in Fig. B.12 that were synthesized with different input current magnitudes.

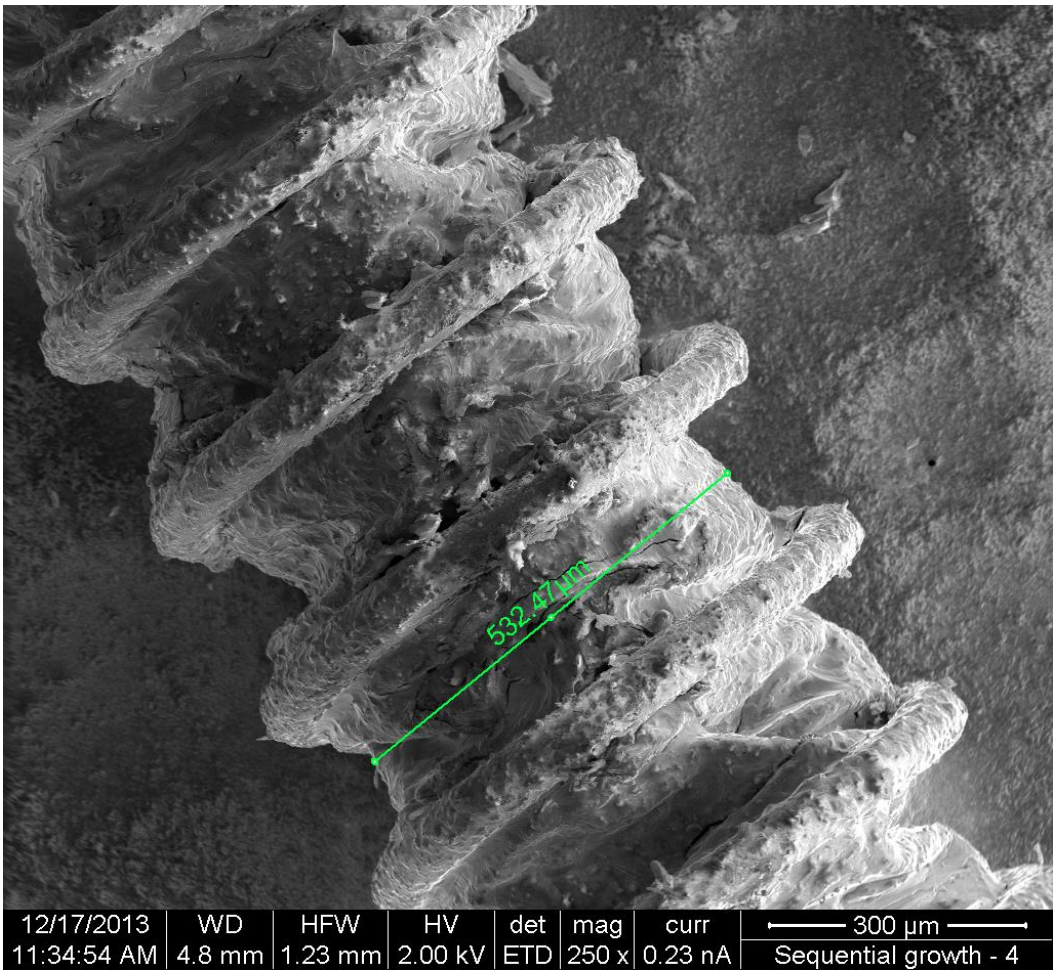

Figure B.1. SEM image of an actuator after the initial growth.

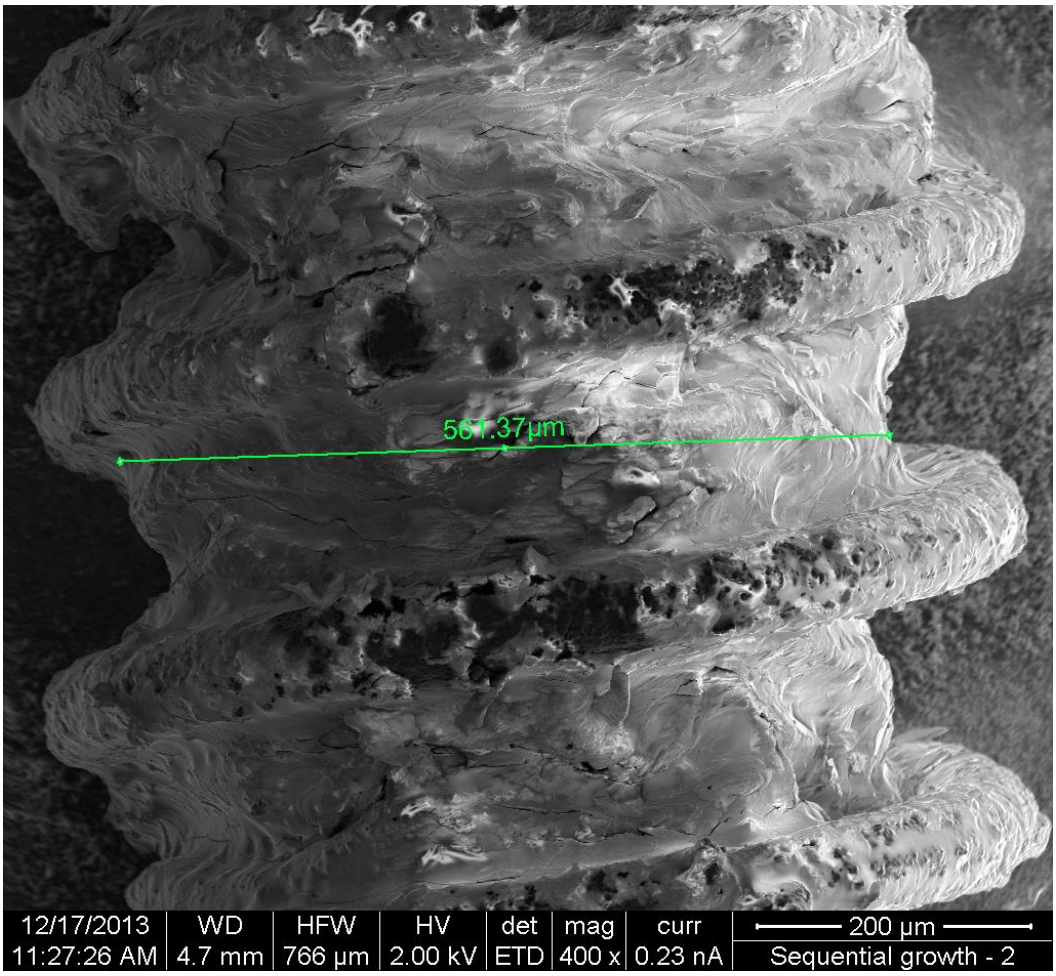

Figure B.2. SEM image of an actuator after the first additional growth stage.

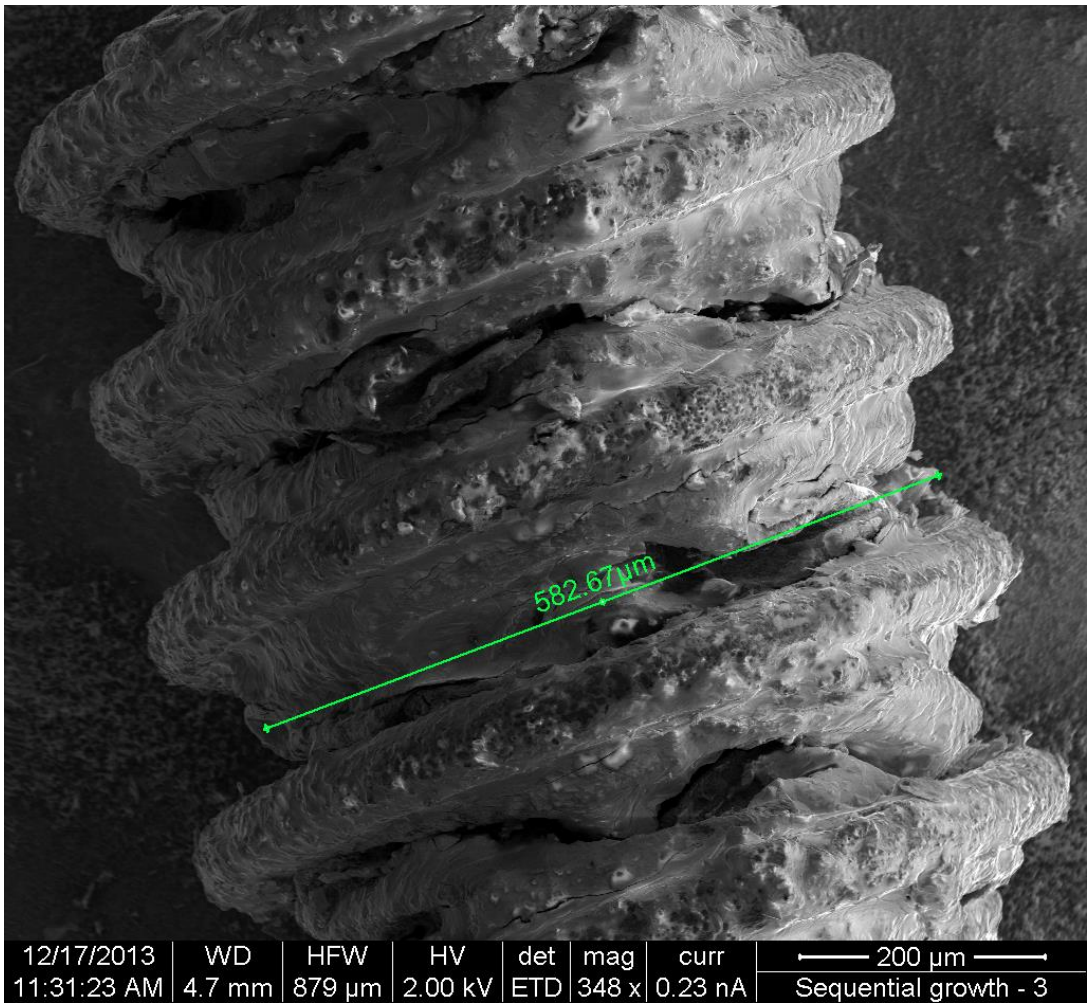

Figure B.3. SEM image of an actuator after the second additional growth stage.

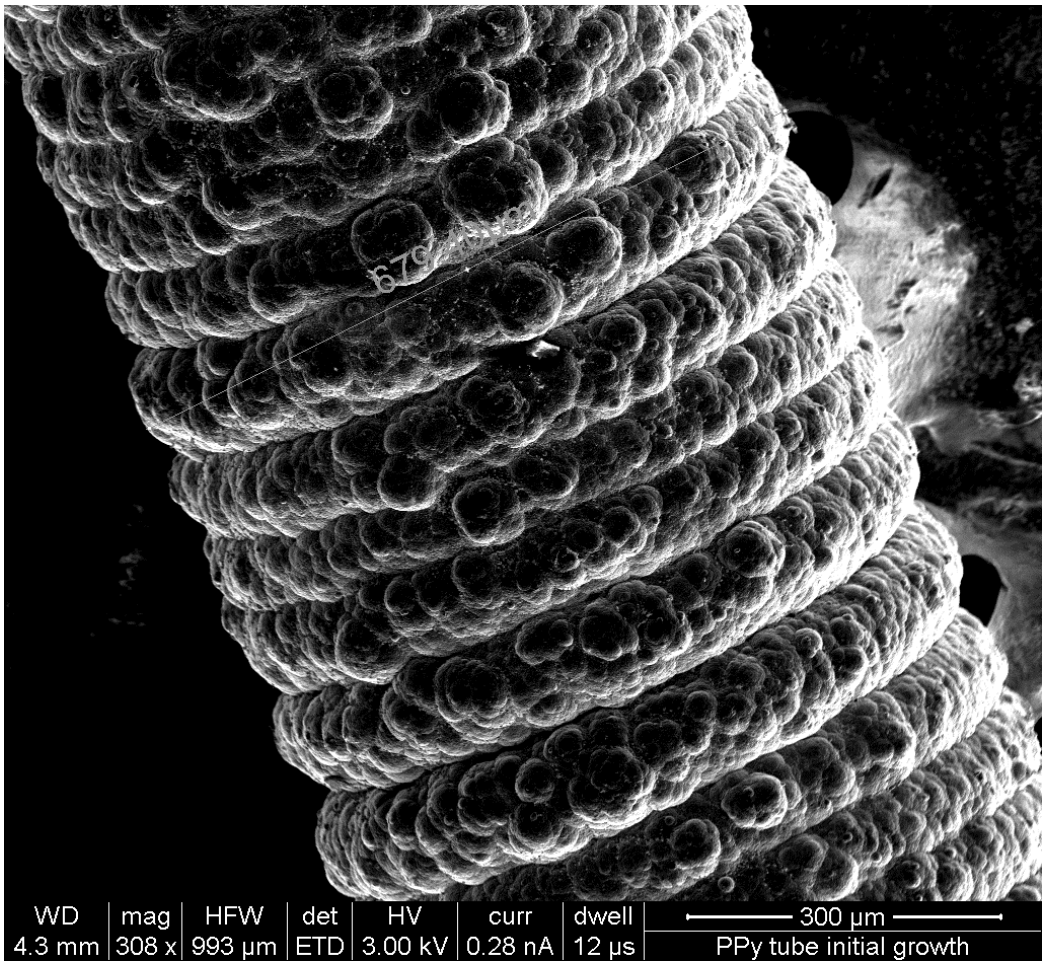

Figure B.4. SEM image of an actuator grown with conventional, continuous conditions.

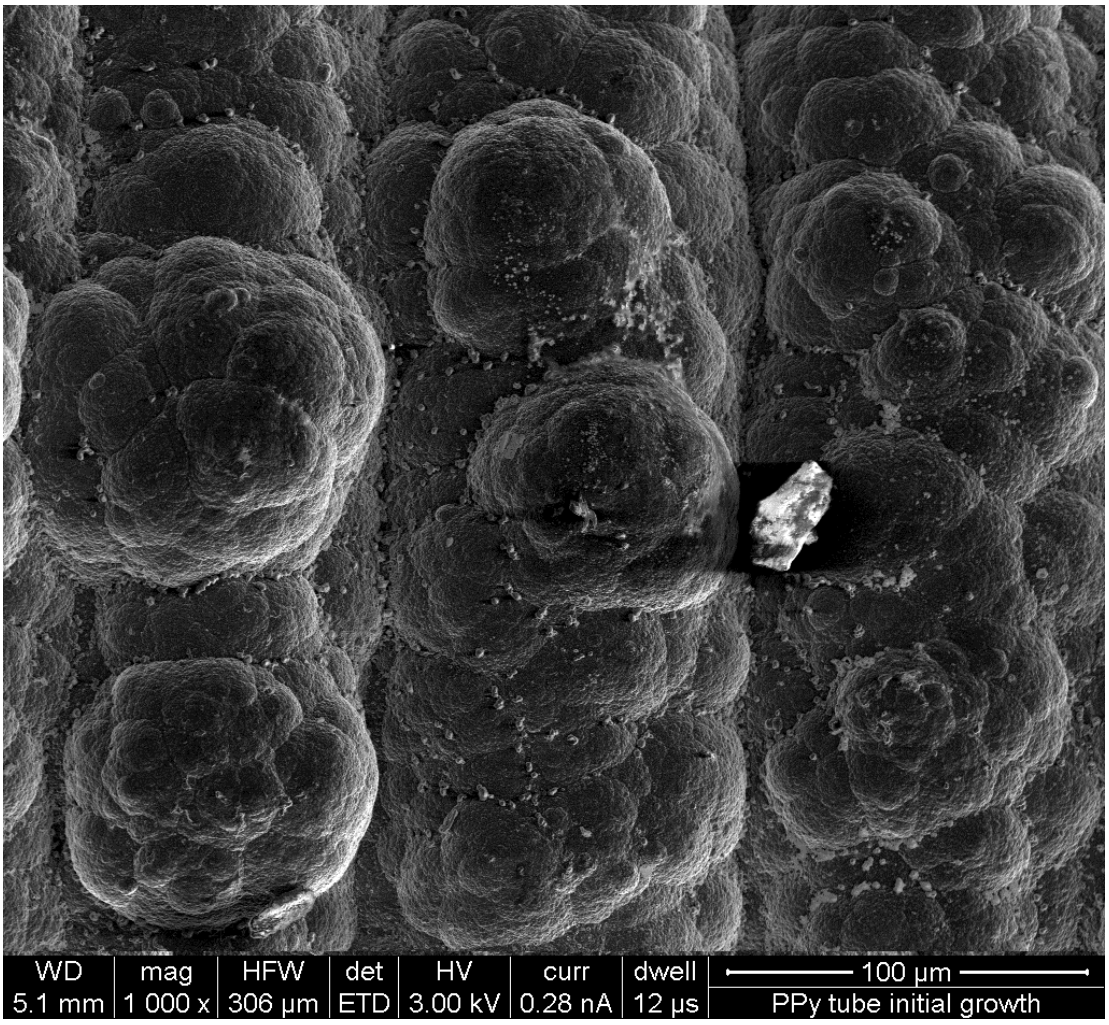

Figure B.5. Increased magnification SEM image of an actuator grown with conventional, continuous conditions.

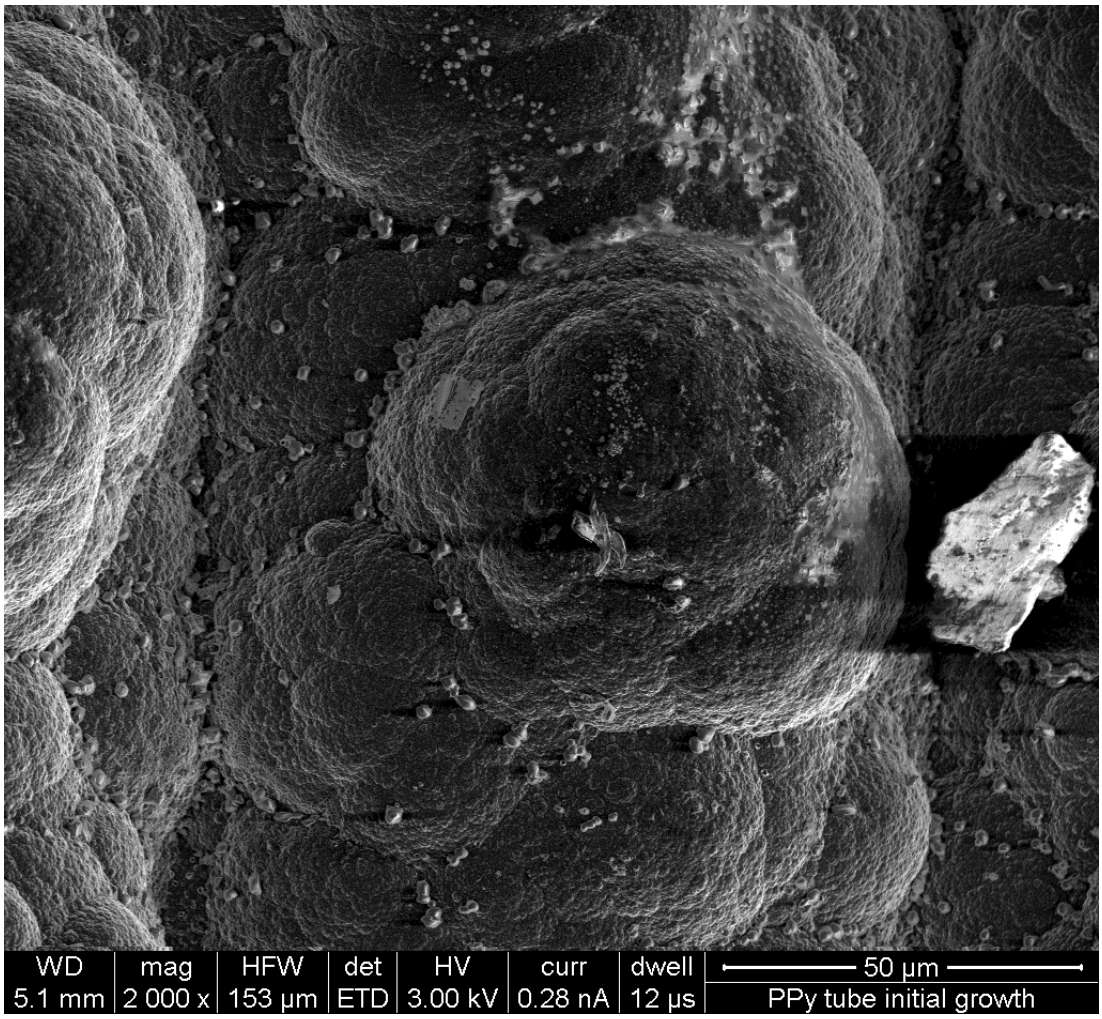

Figure B.6. Further increased magnification SEM image of an actuator grown with conventional, continuous conditions.

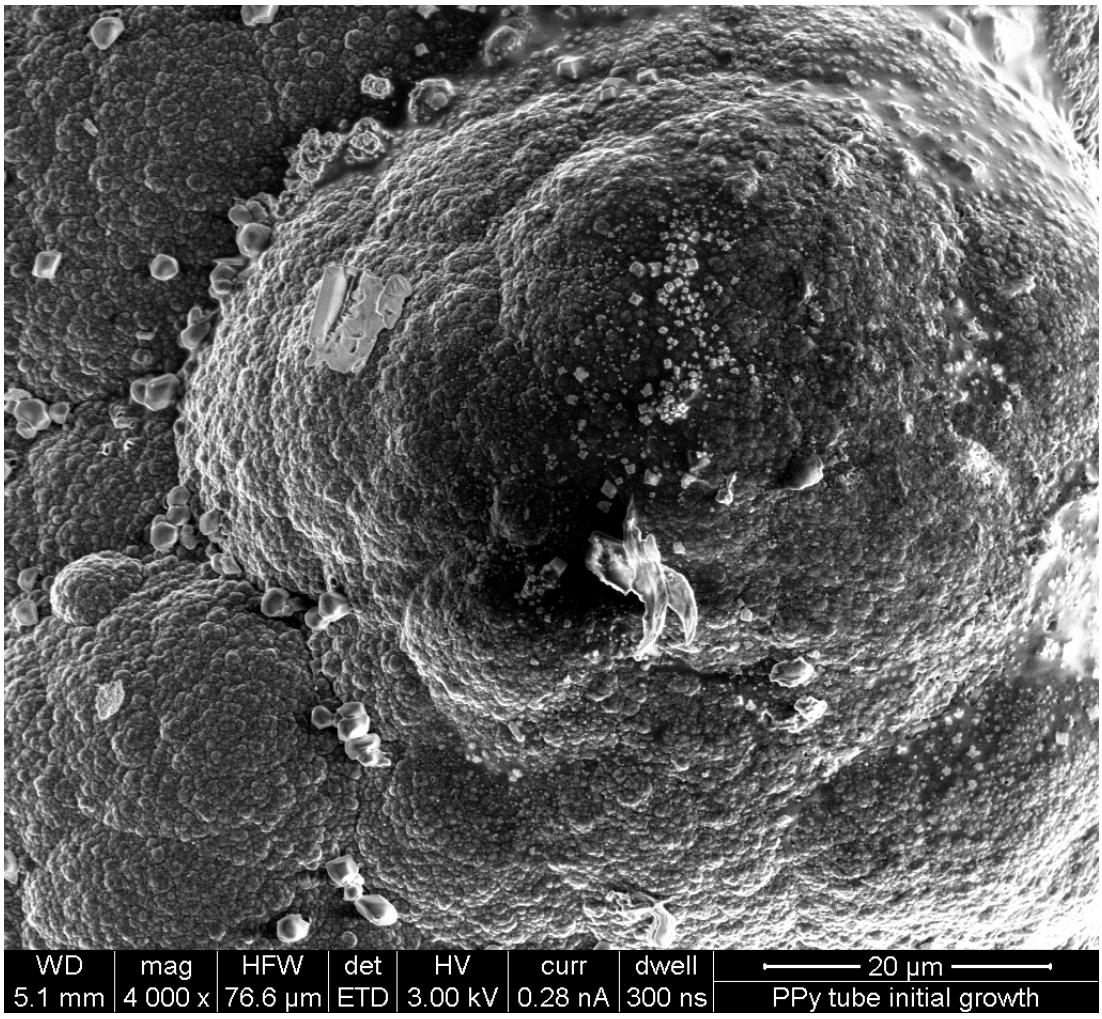

Figure B.7. Further yet increased magnification SEM image of an actuator grown with conventional, continuous conditions. One ‘cauliflower’ section is examined.

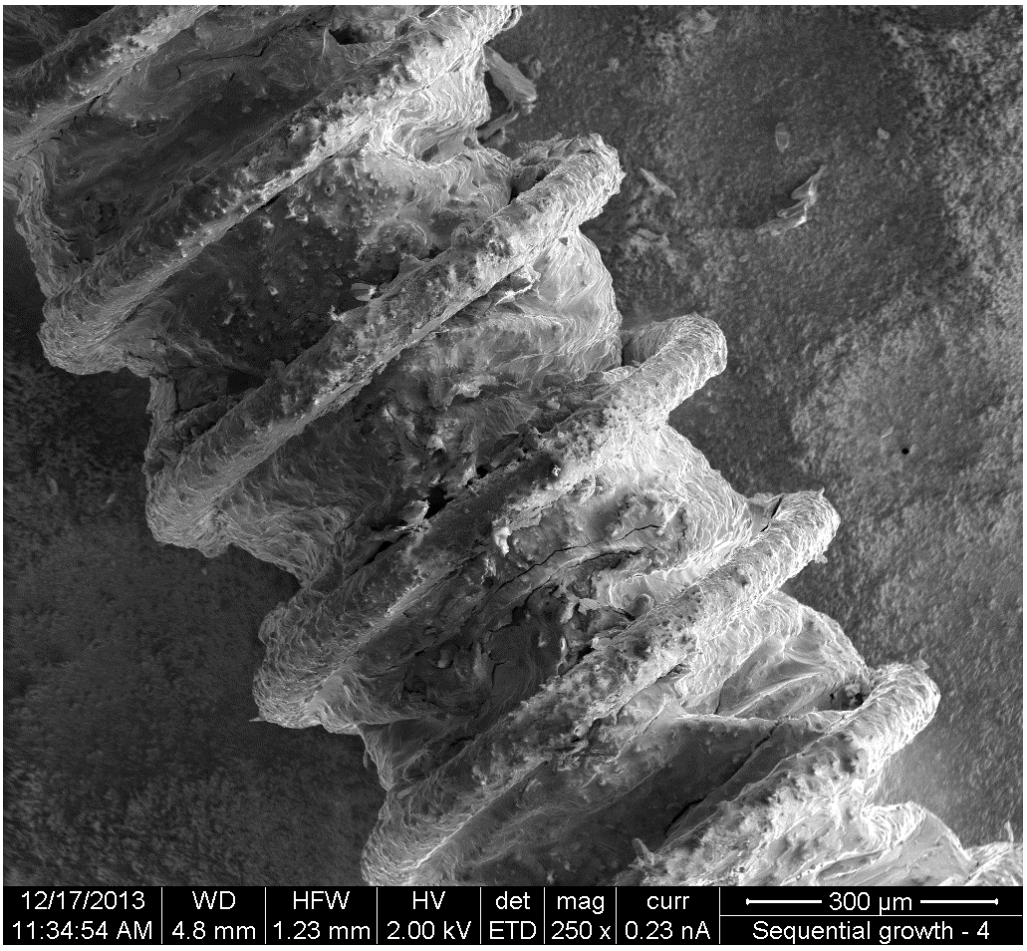

Figure B.8. SEM image of an actuator grown with sequential growth conditions.

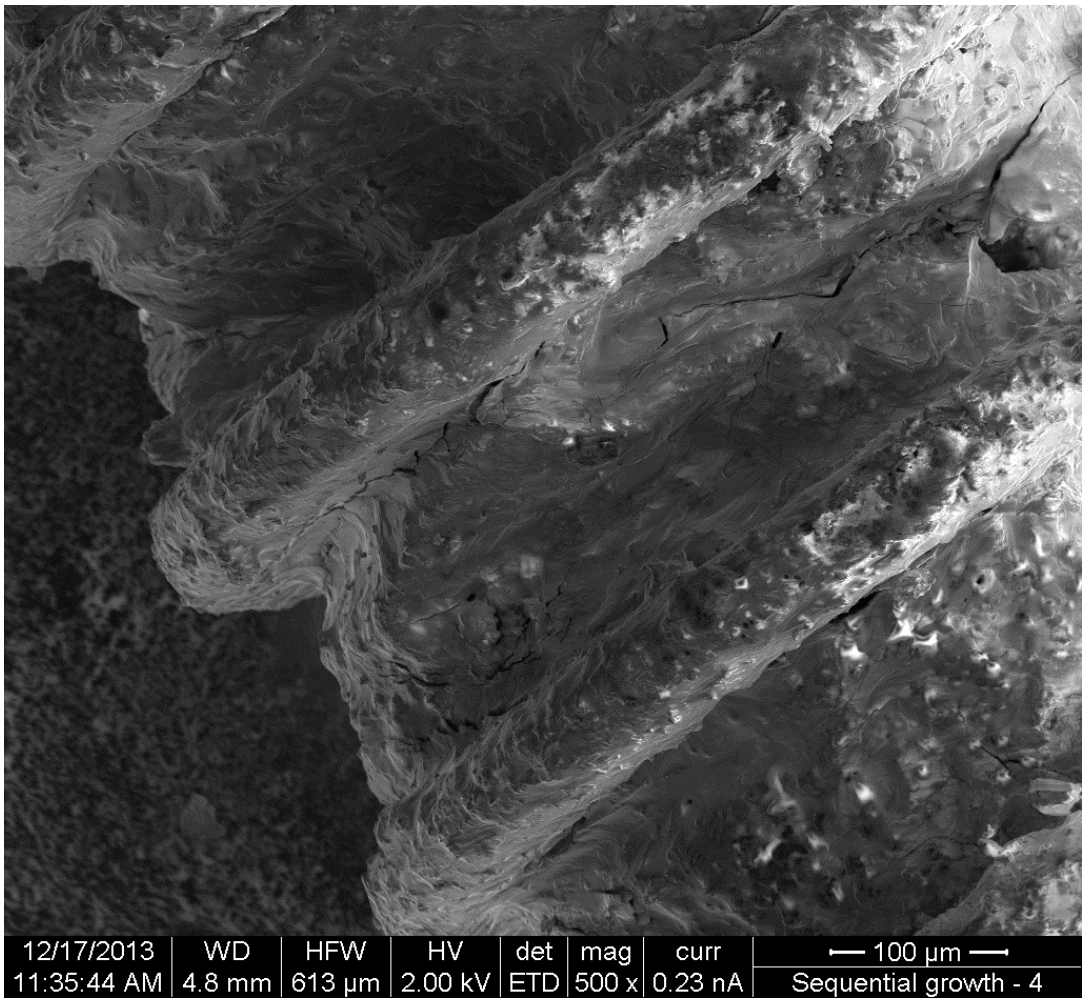

Figure B.9. Increased magnification SEM image of an actuator grown with sequential growth conditions.

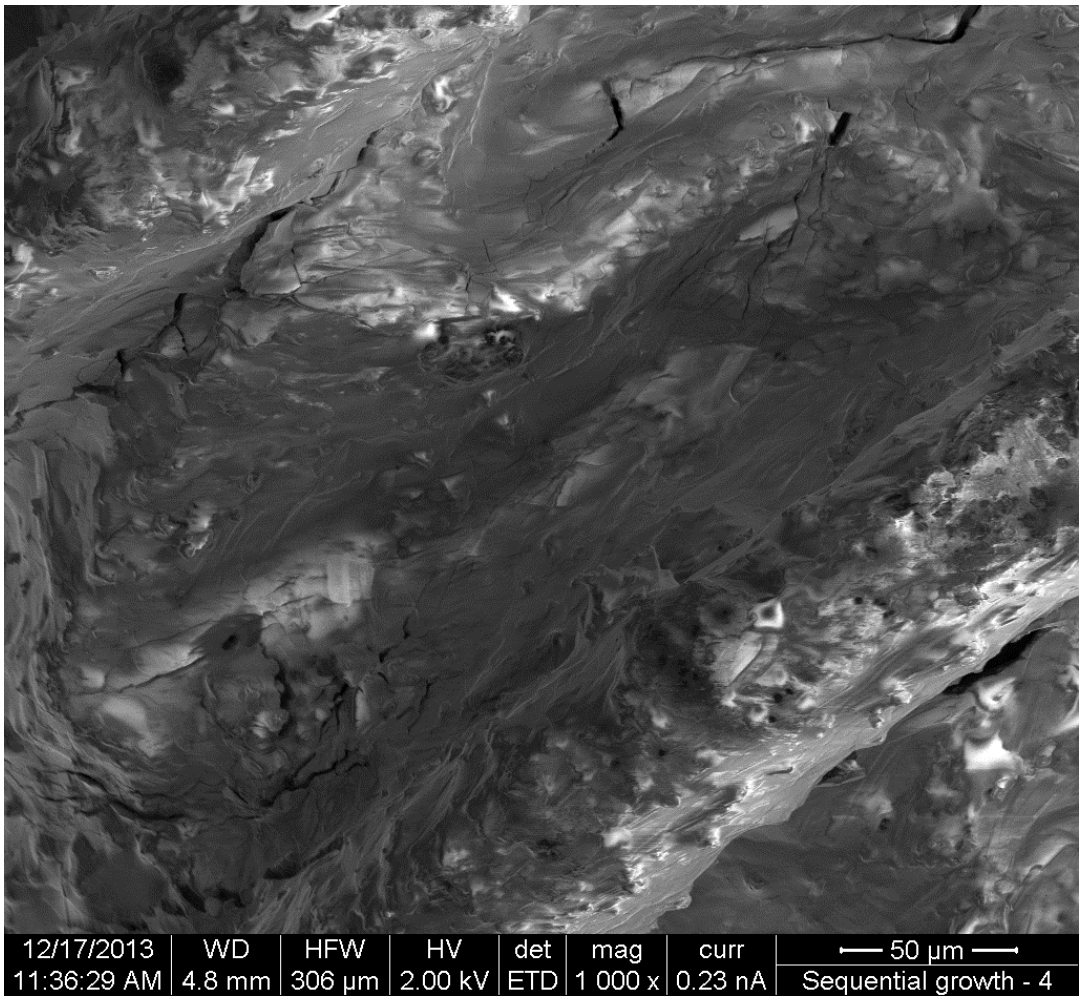

Figure B.10. Further magnified SEM image of an actuator grown with sequential growth conditions.

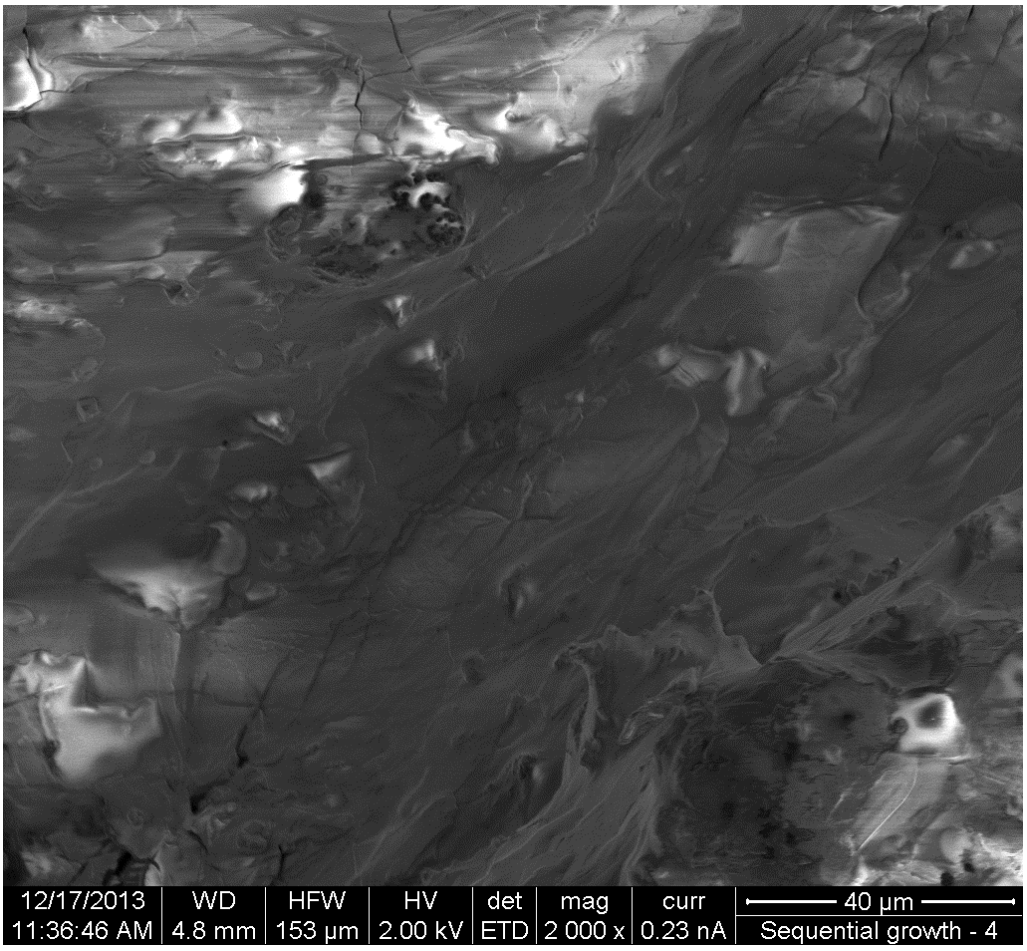

Figure B.11. Further again magnified SEM image of an actuator grown with sequential growth conditions highlighting the surface structure.

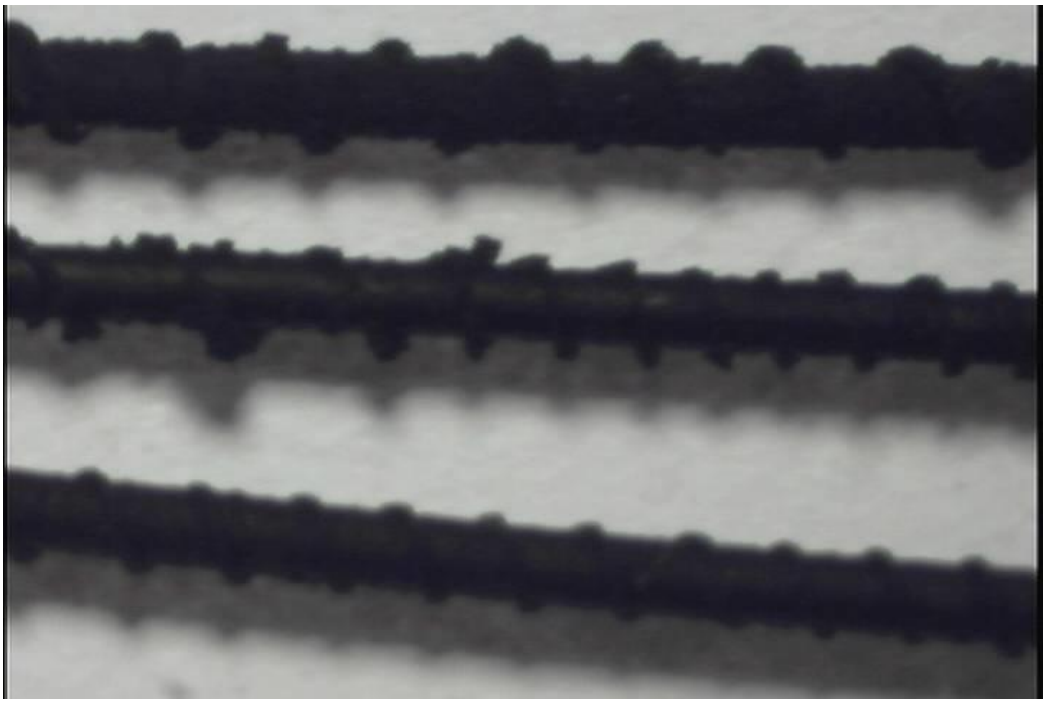

Figure B.12.Images from initial sequential growth tests. The top actuator shows a rougher appearance from increased current input. The middle actuator had a decreased current and decreased superfluous growth, and the third actuator shows a smoother polymer with the lowest current input magnitude of the three actuators.

APPENDIX C

ALTERNATIVE TESTING METHODS AND DELAYED SUCCESS

This appendix outlines some ideas only partially explored. Different experimental paths were pursued to adjust the actuator geometries, core materials and removal methods, coil control strategies, assembly methods, synthesis techniques, and actuation operation approaches.

C.1 Geometries

One of the initial alternate avenues pursued was fabricating custom coils using wire electric discharge machining (EDM). A nitinol tube was machined to similar coil pitch specifications to the coils used. This method allows control of unique coil cross-sections, ideally to optimize electrical conductivity, surface area for polymer adhesion, and coil motion. Another benefit was making connectors built-in to the coil so the additional step of adhering coil leads for connections after the main core is removed is no longer needed. A bayonet connector was selected for the initial prototypes. The geometry is shown in Fig. C.1.

The custom coils permitted polymer growth, but enough samples were not created to attempt sequential growth methods.

C.2 Cores

Another fabrication method attempted was to use a removable core under a thin metallic film that could be dissolved. One such attempt used a beeswax tube covered in a layer of aluminum foil. The wax and foil was fit snuggly into a purchased metal spring. The polymer was synthesized on the foil and coil following continuous growth methods. After growth, the actuator was placed in boiling distilled water to melt the wax and let it flow out. Then the spring, foil, and polymer composite was placed in an aqueous sodium hydroxide solution. This solution dissolved the aluminum, preserving the polymer. The polymer was left preserved, but the overlap section of the aluminum foil was too extreme to allow the polymer to span it. Further testing was not pursued.

Another attempt was made to use a nonconductive material for the core, but coated in a conductive paint. The paint selected coated the core well, but did not stay adhered to the core while in the synthesis solution. Nonetheless, a core material coated, or even sputter coated with a metallic substrate, could improve fabrication and core removal options.

C.3 Coils

The manual coil winder makes coils that have a pitch of 0.5 mm. This pitch could easily be adjusted by fixing one end of the coil to the core, and then pulling or pushing on the free end until the desired coil pitch is achieved. Pulling to extreme pitches, though, held the residual stress in the spring. Initial attempts to remove the stress was to anneal using either an open flame from a lighter, or

boiling water. Although this avenue was not heavily pursued, it is presumed that coil annealing will improve coil performance over a certain actuation range.

C.4 Assembly

Removal of the core from the initially synthesized polymer proved to be a great problem. Many attempts led to destroying the polymer actuator. An attempt to mitigate this problem was made by applying lubricants to the core before synthesis. This did not yield any fruitful results, but it was not yet determined if a lubricant that was not broken down by the synthesis solution was selected.

C.5 Synthesis

Although these actuators are intended for room temperature use, and therefore, room temperature regrowth steps, the initial growth was attempted in a colder environment to produce optimal base layers of the polymer. Initial tests were performed with the synthesis cell in a salt water and ice bath. This produced similar polymer structures. Future work could include a cooling cell around the test cell for initial growth, and ice or preferably dry ice, could be used to cool the initial growth. The test cell would like have to be redesigned, though, since extreme temperature ranges will likely test the seals.

Another method to ease fabrication after the core was removed was to insert core material leads on both ends, affix with epoxy, and then cover with heat shrink. The heat shrink covered the core leads to reduce any undesired electrical conductivity, and provided more material to clamp on to. Unfortunately, this also

made the ends much heavier and this increased the likelihood of damage. This also made the ends bulky in some cases, which helped in separating the actuator from accidentally contacting the reference or counter electrodes, but also made removal and insertion to and from the test cell cumbersome.

C.6 Operation

Actuation as a result in acidity level was preliminarily tested by systematically adding very basic or very acidic chemicals to an aqueous solution of a fabricated actuator, observing any shape change, and checking the pH level using pH testing strips. This proved no observable results, but should not be completely discounted as a possible means for actuation.

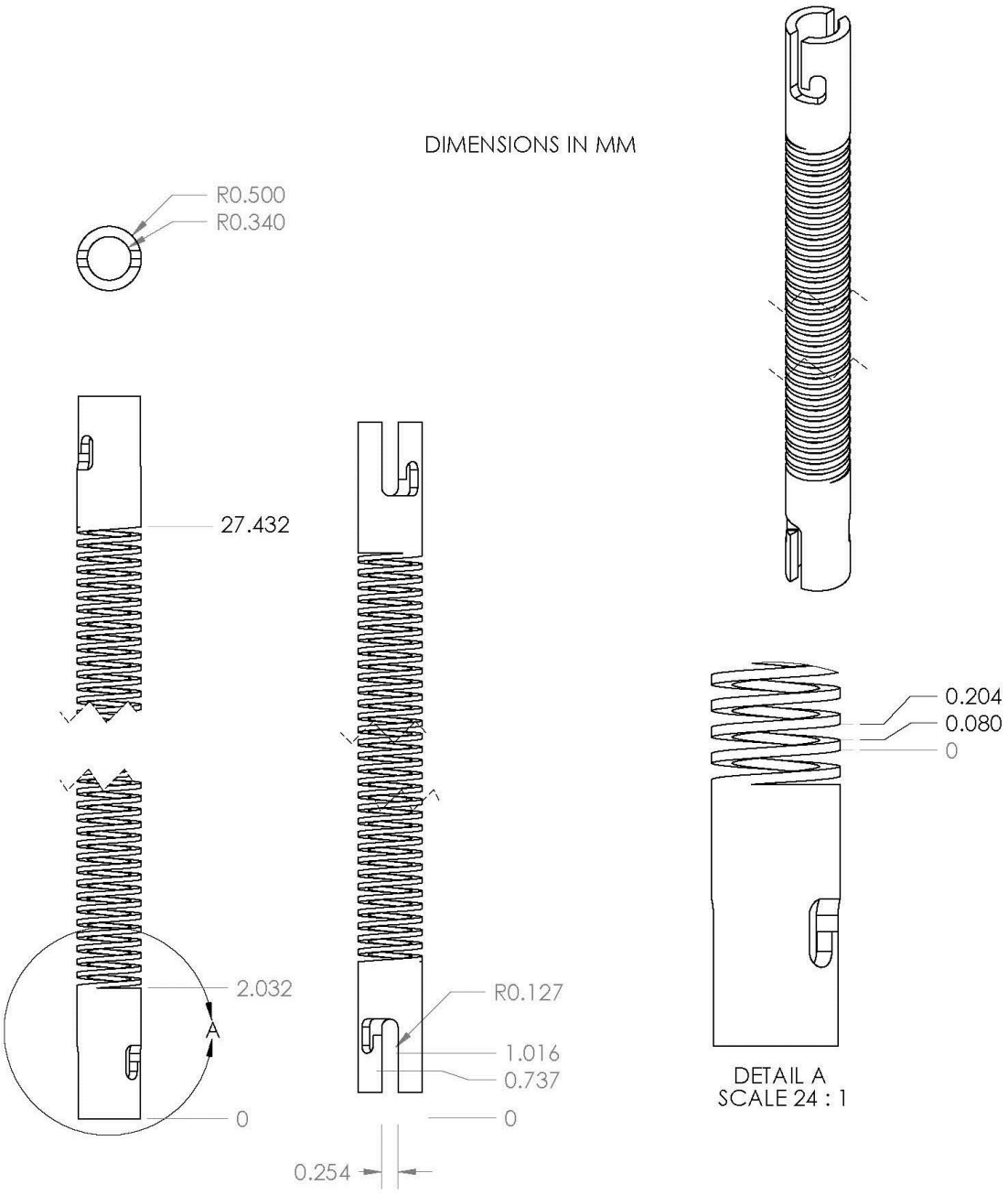

Figure C.1. Custom coil geometry.